



2011-06-06

Microstructure and Transport Properties of Porous Li-ion Electrodes

David E. Stephenson
Brigham Young University - Provo

Follow this and additional works at: <https://scholarsarchive.byu.edu/etd>

 Part of the [Chemical Engineering Commons](#)

BYU ScholarsArchive Citation

Stephenson, David E., "Microstructure and Transport Properties of Porous Li-ion Electrodes" (2011). *All Theses and Dissertations*. 2752.
<https://scholarsarchive.byu.edu/etd/2752>

This Dissertation is brought to you for free and open access by BYU ScholarsArchive. It has been accepted for inclusion in All Theses and Dissertations by an authorized administrator of BYU ScholarsArchive. For more information, please contact scholarsarchive@byu.edu, ellen_amatangelo@byu.edu.

MICROSTRUCTURE AND TRANSPORT PROPERTIES
OF POROUS LI-ION ELECTRODES

David E. Stephenson

A dissertation submitted to the faculty of
Brigham Young University
in partial fulfillment of the requirements for the degree of

Doctor of Philosophy

Dean Wheeler, Chair
John N. Harb
Richard L. Rowley
Ken A. Solen
Randy S. Lewis

Department of Chemical Engineering

Brigham Young University

August 2011

Copyright © 2011 David Stephenson

All Rights Reserved

ABSTRACT

MICROSTRUCTURE AND TRANSPORT PROPERTIES OF POROUS LI-ION ELECTRODES

David E. Stephenson

Department of Chemical Engineering

Doctor of Philosophy

The goal of this work is to understand the relationships between electrode microstructure and mass transport resistances. One can use this information to predict cell performance from fundamental principles. This work includes new types of particle-scale 3D models for correlating and predicting the effects of electrode microstructure on both ionic and electronic transport. The 3D models imitate the sub-micrometer-scale arrangement of active material particles, carbon, binder, and pores and use FIB/SEM images as a basis for parameterization. The 3D models are based respectively on the statistical mechanics techniques of molecular dynamics and Monte Carlo. The approach closely related to molecular dynamics, named the dynamic particle packing (DPP) model, uses aggregates of spheres to recreate electrode microstructures. The other approach, named the stochastic grid (SG) model, is closely related to Monte Carlo techniques in which a small set of fundamental interdomain and bulk energy parameters are used to generate structures.

In order to predict electrode microstructures we correlated the fundamental interdomain and bulk energy parameters for the SG model to electrode mass composition and porosity. We used the revised computer program, known as *predict SG*, to estimate structures of which there are no experimental measurements of electrode structure. From these predicted electrode structures we obtained electronic and ionic transport properties. This allowed us to estimate the trade-offs between ionic and electronic transport for different porosities and carbon fractions.

We found from experimental measurements of electrode structure that carbon and binder formed distinct agglomerates. From the 3D models we determined at commercial fractions of carbon and binder that the conductivity of these carbon agglomerates plays a large role in determining both the electronic and ionic pathways. So in order to better understand the role that these carbon/binder agglomerates play, we explored and developed several experimental methods to find the electronic and ionic conductivity of both simulated carbon domains and complete electrode films. The goal was not only to elucidate the role carbon agglomerates play, but also to develop a non-destructive method of determining overall film properties. Although we found that a non-destructive method is extremely challenging due to probe contact resistances, we did find success in determining carbon domain properties using a delamination method.

Keywords: electrochemistry, monte carlo, structure reconstruction, FIB imaging

ACKNOWLEDGMENTS

To Carl and Susan, my parents who have lived with an idea worth living by. My advisor Dr. Wheeler, Dr. Harb and fellow students Seth Harris, Cole Skelton, Nathan Zacharias, Erik Hartman, Indrajeet Thorat, and James Hillier. This work was supported by the Office of Naval Research under grant No. N000140510865 and by the BATT program of the U.S. Department of Energy under Contract No. DE-AC02-05CH11231.

Contents

1	Introduction	1
1.1	Motivation for the work	3
1.1.1	Design considerations	3
1.1.2	Need for physical insight and predictive capability	4
1.1.3	Approach	5
1.2	Scope of work	6
1.2.1	Prediction of electrode structure from images	6
1.2.2	Predicting effects of electrode morphology on transport	7
1.2.3	Electronic conductivity measurements	7
1.3	Outline	7
2	Background	9
2.1	Introduction	9
2.2	Cathode chemistries	9
2.3	Anode chemistries	11
2.4	Materials and system tested in this work	12
3	Cross-sectional imaging and ionic transport measurements	15
3.1	Introduction	15

3.2	Characterizing structure	16
3.3	Experimental electrodes	17
3.4	Experimentally determining ionic transport	18
3.5	FIB imaging	23
3.6	Structural metrics	26
3.7	Volume analysis of carbon domains	31
3.8	Experiments for determining ionic pathways in carbon domains	34
3.9	Conclusions	35
4	3D microstructure models	37
4.1	Introduction	37
4.2	Background	38
4.3	Dynamic particle packing model	38
4.4	Stochastic grid model	42
4.5	Ionic transport model calculations	46
4.6	Conclusions	52
5	Trade-offs between ionic and electronic resistances	55
5.1	Introduction	55
5.2	Electronic conductivity of LiCoO_2	58
5.3	Interparticle connections	60
5.4	SG model electronic predictions	62
5.5	SG predictive model	65
5.5.1	Parametrizing the SG predictive model	66
5.5.2	Electronic transport results with different resolutions	70
5.5.3	Determining the importance of carbon on overall conductivity	71
5.5.4	Relationship between porosity and carbon domain volume	76

5.5.5	Ionic pathways	78
5.5.6	Structure changes and its effects	78
5.5.7	PSG model limitations	81
5.5.8	Experimental results of varying carbon fractions	82
5.6	Conclusions	84
6	Electronic conductivity experiments	87
6.1	Introduction	87
6.2	Intrinsic conductivity measurements	88
6.3	Overall effective conductivity measurements	89
6.4	Four-point probe on delaminated films	92
6.5	Tangential probe	95
6.5.1	Electronic measurements of electrode films	98
6.5.2	PSG model validation versus experiments	101
6.5.3	Electronic measurements of simulated carbon domains	101
6.6	Comparing tangential probe measurements to PSG model results	102
6.7	Normal-direction AC impedance	107
6.7.1	Experiments	109
6.7.2	Baseline AC test	111
6.7.3	Pressure-dependence AC test	113
6.7.4	Voltage-bias AC test	114
6.8	Proof of concept for the thermal method	115
6.9	Conclusions	118
7	Summary and scope for future work	121
7.1	FIB/SEM imaging and 3D structural reconstructions	121
7.2	3D Model predictions on the effects of structure and composition	123

7.3	Experimental determination of transport in films	124
-----	--	-----

List of Tables

3.1	Calculated volume fractions of raw materials and domains.	29
3.2	Volume fractions analysis.	33
4.1	Cathode tortuosity predictions for around 34% overall porosity.	51
5.1	Inter and intra domain constants.	67
5.2	Varying performance at different discharge rates and carbon fractions.	84
6.1	Tangential probe electronic measurements.	100

List of Figures

2.1	Schematic of porous cathode cell studied in this work.	13
3.1	Schematic of FIB instrument.	16
3.2	Schematic of a symmetric cell.	19
3.3	34% porosity Saft electrode polarization-interrupt experiment.	20
3.4	46:54 binder-to-carbon black polarization-interrupt experiment.	21
3.5	SEM image of a porous cathode including ablated planar section.	23
3.6	Segmented FIB/SEM images of electrode films with varying porosities.	25
3.7	Domain (A, P, C) volume fractions versus porosity of electrodes.	28
3.8	Lateral neighbors (L) and diagonal neighbors (D) for a central pixel.	28
3.9	Inter and intra domain neighbor contact probabilities versus distance.	31
4.1	$30\ \mu\text{m} \times 30\ \mu\text{m}$ slice from a DPP model configuration at 34% porosity.	40
4.2	$30\ \mu\text{m} \times 30\ \mu\text{m}$ slices for 34% porosity electrode.	45
4.3	SG model tortuosity versus node resolution for 34% porosity electrode.	49
4.4	SG model reconstruction using non coarse-grained statistics.	50
4.5	Simulated and experimental electrode tortuosity versus porosity.	50
5.1	$30\ \mu\text{m}$ cube of 34% porosity electrode with carbon domains.	57
5.2	$30\ \mu\text{m}$ cube of 34% porosity electrode without carbon domains.	58

5.3	Picture of discharge of a two-phase material like LiCoO_2	60
5.4	Interdomain contact areas per unit volume versus porosity.	61
5.5	Model prediction of dimensionless conductivities versus porosity.	64
5.6	Electronic results of the SG model.	65
5.7	Electronic validation of predict SG model versus the baseline SG model.	68
5.8	PSG model reconstructions versus baseline SG model reconstructions.	69
5.9	Comparisons of Predict and baseline SG models.	69
5.10	Overall dimensionless conductivity versus resolution.	70
5.11	Electronic and ionic dimensionless conductivity changes with carbon fractions.	72
5.12	Different resistive circuits.	74
5.13	Electronic resistances at different ε_C and σ_A/σ_C ratios.	77
5.14	2D slices from PSG model at 34% porosity.	79
5.15	2D slices from PSG model at 45% porosity.	80
5.16	2D slices from PSG model at 51% porosity.	81
6.1	Equivalent circuit of dry electrode impedance.	91
6.2	Four-point probe setup.	93
6.3	Images of experimental flat electrode setup	96
6.4	Illustration of tangential probe experimental setup	97
6.5	Resistance of free-standing carbon film.	98
6.6	Area-specific resistance of 45% porosity Saft films.	99
6.7	Electronic conductivity of free-standing carbon films.	103
6.8	Contact resistances of free-standing carbon films.	104
6.9	Experimental electrode conductivity versus PSG model.	106
6.10	Experimental electrode tortuosity versus PSG model predictions.	107
6.11	Hoped for impedance circuit.	109

6.12	Images of experimental setup for AC experiment.	110
6.13	Schematic of experimental setup for AC experiment.	110
6.14	Real part of impedance versus frequency.	112
6.15	Real part of impedance versus frequency for 51% porosity Saft.	114
6.16	Real part of impedance versus frequency for 51% porosity Saft electrode. . .	116
6.17	Hotplate with Saft films.	117
6.18	Hotplate results with Saft films.	118

List of Symbols

Roman

r	distance between two points
$g(r)$	radial distribution function
G	relative probability
P	observed pair probability
D	intrinsic diffusivity
$C_2(r)$	two-point cluster function
$L(r)$	lineal-path function
L	length of the simulated system
\mathbf{s}	site location vector
\mathcal{I}	electrical current
Δt	time increment
k_B	Boltzmann's constant
T	temperature

f	potential of mean force
m	particle mass
w	electrode constituent mass fraction
x	fraction of pore going into the carbon domain
y	fraction of binder going into the carbon domain
R	ratio of binder-to-carbon or real part of impedance
R	resistance
A	area
L	length
V	voltage
I	current
C	capacitance
π	pi
t	thickness
Z	complex impedance
jX	imaginary part of the impedance
Greek	
ρ	density of an electrode constituent
ε	porosity or volume fraction (with subscript) of an imaged domain

δ	node size
κ	ionic conductivity
σ	Lennard-Jones size parameter or solid conductivity
ϵ	Lennard-Jones energy parameter
ϕ	electric potential
ω	frequency

Subscripts

i, j	domain types
I	center site
J	adjacent site
0	fixed constant
c	carbon or carbon domain
C	carbon domain
p	pore or pore domain
P	pore domain
a	active or active domain
A	active domain
b	binder
x	fraction of lithium

Superscripts

eff effective

tot total

ext external

dev deviation

L lateral

D diagonal

Chapter 1

Introduction

Rechargeable Lithium-ion (Li-ion) batteries are a highly useful technology for portable energy storage and could have many more possible commercial applications. This is due in part to their high cell voltage, as much as 4.2 volts, as compared to 2.0 volts for lead-acid batteries and 1.4-1.45 volts for nickel-metal-hydride cells. Generally speaking for rechargeable battery chemistries, higher voltage translates to higher energy density. Energy density is a product of cell potential and capacity per unit mass. Lithium-based chemistries have a high cell potential as well as a high capacity per unit mass. Because of these properties, Li-ion batteries have already been commercialized for high energy applications like cellphones and laptop batteries.

Nevertheless, difficulties with Li-ion technology can include poor cycle life, reduced low-temperature performance, and limitations on their possible power performance. Many of the performance and degradation issues are related to electronic or ionic transport, leading workers to attempt to improve cell performance by decreasing transport resistances [1–3].

If the high energy density of Li-ion batteries can be coupled with increased power performance and lower costs, the applications of Li-ion batteries will significantly increase. Such applications for lithium batteries can include larger portable devices with moderate to high

power requirements, for example everything from hand tools to electric cars. For lithium batteries to become widespread in these higher power/energy applications, performance and life span must be improved along with enhanced safety, all at lower costs.

Li-ion batteries are composed of two electrodes separated from each other by a separator material. Commercial electrodes are generally formed of particles of active materials and carbon bound together by a binder. The electrodes are labeled as cathode and anode, which by convention are defined so that the anode active material is oxidized during cell discharge while the cathode active material is reduced. Secondary Li-ion battery cathodes primarily contain metal oxides like LiCoO_2 or LiMn_2O_4 while anodes are composed primarily of carbon.

The power obtained from a cell is related to the potential between the electrodes (more specifically, the open-circuit or equilibrium voltage) and the internal resistances of the cell. Resistances come in the forms of transport (ionic and electronic) and reaction-type resistances. Work has been done to isolate and determine these different resistances [2, 4–6], which depend on structural and chemical conditions in the cell. However, because of the complex and integrated nature of these resistances, determining and analyzing them individually is extremely difficult.

Parts of this work are being published or prepared for publication. Due to papers being collaborative endeavors with multiple authors I used the plural *we* rather than *I* throughout this work. This work includes contributions from my adviser, the Naval Research Laboratory, and undergraduates.

1.1 Motivation for the work

1.1.1 Design considerations

The challenge of increasing cell power performance requires decreasing transport losses through modifications in electrode design both in materials used and the structure of the electrodes. For example some materials (like carbon) have a high electronic conductivity allowing for easy transfer of electrons. However, we have found in the LiCoO_2 cathodes that the carbon when mixed with binder creates agglomerates that highly restrict ionic transport. So adding carbon to an electrode will improve electronic conductivity, yet diminish electrode ionic conductivity.

Another example is the amount of pore space available in the electrode structure. Pore space is dependent on the amount of calendaring (mechanical squeezing between rollers) used during manufacture of the porous electrode films. Ionic pathways improve as more pore space is allowed in the electrode [7]. However, at the same time the electronic resistances decrease with increased pore space [2]. So there is a trade off between these two resistances when calendaring.

Another trade-off in cells is between power performance and energy density. This trade-off can be illustrated by examining the performance changes upon varying cathode film thicknesses. Decreasing the thickness of electrodes decreases transport distances, thereby lowering transport losses and increasing power. However, this also generally lowers the amount of active material in each battery relative to a thicker-electrode cell, thereby lowering the energy density of the cell. The challenge of designing thicker electrodes with similar losses as thin cells will require a comprehensive consideration of the design of electrodes. In particular an understanding of how cell structure (or cell morphology) and cell thickness affect transport losses will be needed to facilitate solutions to this complex problem.

A primary consideration in cell design is the duty cycle required of the cell, which is determined by the device being powered [8]. Some devices like micropower devices need high-power discharge pulses with either long rest times or slow discharge rates [9]. Other devices like computers need more constant discharge rates [10]. Electric vehicle batteries require a range of discharge rates ranging from high-power pulses (greater than 1C discharge) to low power steady discharge with high overall energy requirements [11].

Chemical degradation also limits the lifetime of battery cells, which increases the costs associated with Li-ion batteries. It may be possible to modify cell design so as to minimize the effects of chemical degradation and therefore maximize cell lifetime. Chemical degradation reactions depend on the rate of discharge as well as the operating and storage temperature [12, 13]. Chemical degradation affects ionic and electronic pathways differently [14–17]. Optimum cell design balances the overall effects of ionic and electronic transport to be approximately equal. In order to achieve an optimum cell design with changing ionic and electronic transport may mean that an electrode optimized to provide a specific energy/power requirement after 50,000 cycles would be materially and structurally different from an electrode optimized for 100 cycles. Changes in cell materials and structure could compensate for the different degradation rates.

1.1.2 Need for physical insight and predictive capability

Current manufacturing and design parameters are largely determined empirically, for example volume fractions of electrolyte and solid materials, thickness of electrodes, electrolyte concentration and positive-to-negative electrode capacity ratio. Determining the optimum cell parameters is expensive and time consuming [18–20] especially for applications that require guaranteed performance characteristics over years of operation [21–24]. A physical understanding of the connections between cell performance and manufacturing and design

processes could improve the ability to predict cell performance. This can lead to manufactured electrodes that are tailored for each specific application's power/energy requirements and lifetime. Reductions in both production time as well as material costs could result from this engineering work.

1.1.3 Approach

State-of-the-art electrochemical models frequently incorporate transport and reaction kinetics equations. Because of the complexity of the cell microstructure, transport and reaction kinetics equations are frequently modified so that their solutions depend only on the spatial depth in an electrode (a 1-dimensional position) rather than cell volume (a 3-dimensional position). In order to modify transport and kinetic equations to apply in one dimension an assumption is made that a tensorial property can be spatially averaged into an effective scalar property [5]. This modification relies on an untested assumption that the averaging of properties does not diminish model accuracy. As a result of property averaging, transport mechanisms rely on effective resistance parameters. These effective resistances may be unphysical or incapable of reproducing physical processes that occur non isotropically within an electrode [2]. Also another drawback is that effective transport parameters are difficult to predict or determine.

In order to minimize the possible negative effects of volume averaging, a more accurate picture of 3D microstructure is required. Once the 3D microstructure is determined, a 3D electrochemical model can be developed that relies less on volume-averaged equations. The approach taken in this work is to combine theoretical models with experiments. The experimental work provides images of electrode structures from which model parameters can be determined and validated. Some additional experimental work was done to determine both ionic and electronic properties of electrodes and carbon/binder films and was also used to

validate the models. Two forms of theoretical models were developed: structural and electrochemical. The structural model is able to recreate and predict electrode structures and quantify the ionic and electronic pathways through the electrode structure. The electrochemical model couples ionic and electronic transport resistances to electrochemical reactions in order to determine the effect properties have on cell performance.

1.2 Scope of work

The objective of this work is to develop tools that can predict electrode performance for different manufacturing and design conditions. Cell energetic losses can be minimized by increasing the electronic and ionic access at distributed reaction locations, which access in turn depends on cell design and materials [2, 25–29]. This work focuses on improving electronic and ionic access by understanding material and electrode microstructure trade-offs on transport. Modifying the underlying chemistry or material types was not the focus of this work. The tasks and results of this work are summarized as follows.

1.2.1 Prediction of electrode structure from images

In order to better understand morphology we needed experimental data on electrode structure. To do this we collaborated with David Rowenhorst of the Naval Research Laboratory (NRL), who used focused ion beams to ablate commercially made LiCoO_2 cathodes manufactured to different pore volume fractions. Resulting flat cross sections were imaged using scanning electron microscopy (SEM). We assisted in analyzing FIB/SEM images and were able to determine statistically important structural characteristics that could be used to recreate 3D electrode structures. Ionic resistances of the predicted 3D electrode structures were compared to experimental values. It was shown that correct trends with electrode porosity in ionic transport behavior were shown by the predicted electrode structures.

1.2.2 Predicting effects of electrode morphology on transport

To predict structure requires an understanding of how electrode morphology changes with material and pore volume fractions. The statistically important structural characteristics that could recreate structure were further analyzed and correlated with component volume fractions. Including these correlations into the reconstruction code allows us to predict structures at different material and pore volume fractions.

The electronic and ionic resistances of resulting predicted structures were validated by looking at ionic and electronic resistances independently for a range of porosities as well as different volume fractions of carbon and binder.

1.2.3 Electronic conductivity measurements

In order to better quantify the accuracy of predicted electronic resistances to actual electrode conductivity we performed electronic conductivity measurements on films. Both mixtures of just carbon and binder as well as commercial electrodes from Saft America were tested with three different experiments. We found that electronic conductivity is highly dependent on the pressure applied to films as well as the ratio of binder-to-carbon.

1.3 Outline

The remainder of this document is organized as follows.

Background. Chapter 2 is a brief description of the physical processes in battery operation. Brief summaries of the materials used as well as basic battery fabrication procedures are described. Subsequent chapters contain additional descriptions of materials used in this work.

FIB/SEM imaging. Chapter 3 goes through experimental FIB/SEM imaging techniques and background.

3D Microstructure Models. Chapter 4 explains the important statistical metrics found from FIB/SEM imaging that can be used to recreate electrode structures. Imaged structures of carbon and binder mixtures are discussed as well as experimental determination of ionic pathways through them. Chapter 4 presents two different methods for electrode reconstruction. Ionic pathways are determined from electrode reconstructions. Results are compared to experimentally obtained values of ionic pathways. Effects of carbon/binder/pore domains are quantified both experimentally and theoretically.

Trade-Offs between Ionic and Electronic Results. Chapter 5 shows the experimental results on interparticle connections and how they change with volume fractions. Also comparisons between empirically parametrized electrode reconstructions versus models parametrized directly from experimentally imaged electrodes structures. From empirically parametrized electrode reconstructions across a range of porosities and material fractions we present how interparticle connections affect electronic resistances.

Electronic conductivity measurements. Chapter 6 outlines three different electronic conductivity measurements. We tested different films we created as well as commercial electrode films.

Conclusions. Chapter 7 presents the conclusions drawn from this work as well as some possible future directions for additional reconstruction and modeling work.

Chapter 2

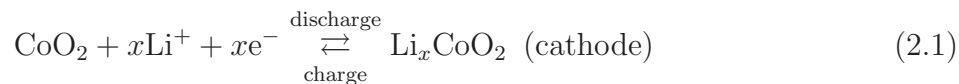
Background

2.1 Introduction

This chapter provides an overview of what chemistries have been used for rechargeable batteries. Also included is an overview of rechargeable battery cells and the important transport processes that occur in them. This background is necessary to provide context for this study of cell resistances and their connection to electrode structure.

2.2 Cathode chemistries

Numerous lithium-based chemistries have been or are being studied for rechargeable batteries, but three chemistries are the most notable. LiCoO_2 was the first commercialized Li-ion cathode chemistry (circa 1990) [30] and its reaction is



where x represents the fraction of lithium, which stoichiometric ratio ranges between 0.5 and 1. Even though the amount of lithium is variable, for convenience we refer to this material

as LiCoO₂. LiCoO₂ materials used in batteries have not changed much since their discovery by Goodenough and coworkers [31]. Different synthesis temperatures of LiCoO₂ have been experimented with [30], which result in particle size and crystal variations. Particle size of commercial grade LiCoO₂ is generally on the order of 3-5 μm.

More recently LiFePO₄, has started to be commercialized as a cathode material. Although it has lower energy density than LiCoO₂, it also has lower potential material costs and a lower toxicity. The reaction is



where once again x varies between 0 and 1. Due to the low solid diffusion of lithium ions in LiFePO₄, the particle size of commercial grade LiFePO₄ is on the order of 100 nm [32–34]. Because of the low intrinsic electronic conductivity of LiFePO₄, synthesis steps have been developed which create carbon coatings around nano-sized particles. The carbon coatings have been shown to improve electronic contact and thus improve performance by lowering electronic transport resistances [35–37]. Due to these manufacturing techniques that increase electronic conductivity of LiFePO₄ electrodes, it has been found that LiFePO₄ may actually be better suited for high-power cells than other chemistries.

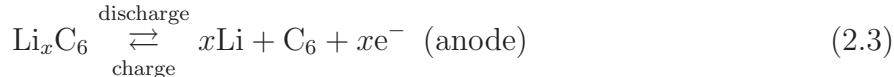
There are other rechargeable lithium chemistries which have the potential to have higher energy densities than LiCoO₂ and LiFePO₄ but have yet to be commercialized for various reasons. A possible future commercializable chemistry is Li/O₂ chemistry (or Li-air). Interest in Li-air chemistry has been around for quite some time, but the first practical non-aqueous Li-air battery was demonstrated by K. M. Abraham and co-workers in 1996 [38]. Possible advantages of cells based on an air cathode are numerous such as lower material costs (oxygen is very abundant) and higher energy density (oxygen is one of the most electronegative elements). For instance, the theoretical energy density of Li/O₂ is ten times greater than cells based on LiCoO₂. However the Li/O₂ chemistry has yet to be commercialized because

of numerous technical issues including extremely low mass transport and precipitation of Li_2O_2 and LiO_2 on cathodes, effectively poisoning reaction sites and plugging up pores.

Some other rechargeable lithium chemistries include lithium sulfur (Li-S), lithium nickel oxide (LiNiO_2), and lithium manganese oxide (LiMn_2O_4). Li-S, despite having a relatively large cell potential, tends to dissolve into electrolyte, which causes irreversible loss of active material and performance [39]. LiNiO_2 has problematic stability with overcharge as well as relatively high costs. LiMn_2O_4 suffered from low capacities and rapid capacity fade with cycling [40] which have been overcome by drying. LiMn_2O_4 materials are used in approximately 80% of commercial Li-ion batteries currently.

2.3 Anode chemistries

Anodes are generally made commercially in the form of carbon-and-binder mixtures. This is because carbon has a small electrochemical potential versus lithium, it is cheap, it is lightweight, and it is electrically conductive. The reaction of lithium with graphite carbon is



where C represents the carbon atoms in the solid. While generally 6 carbon atoms react with one lithium to generate 372 mAh/g of capacity, this quantity is somewhat variable depending on the form of carbon and defects within the solid. Expansion and contraction of carbon during charge and discharge is small due to lithium being such a light element and only one atom generally reacts with six carbon atoms. Low volume expansion helps make carbon a stable anode material.

Commercial anodes using Li_2TiO_3 are being used to eliminate expensive and time-consuming solid-electrolyte-interphase formation cycles required of carbon anodes. However,

Li_2TiO_3 has a higher cost and lower potential difference versus LiMn_2O_4 and LiCoO_2 cathode materials.

A future anode type that has caught the interest of the battery community is the group of lithium alloys such as lithium silicon (Li-Si). Li-Si anodes have much higher energy density in comparison to the carbon anodes. However, this increase in capacity leads to material expansion issues. Because so much lithium can react with silicon, particles of Li-Si generally expand by 400% during charging. This expansion and subsequent contraction leads to fracturing of particles which causes particles to become electrically isolated, leading to irreversible capacity loss.

In the work done here, the anodes were made of lithium metal foils instead of a carbon-and-binder mixture. This was done to reduce the experimental variation in the anode and to highlight cathode performance. However, lithium metal is not used in commercial cells due to dendrite formation, which shorts cells, as well as safety issues due to the reactivity of lithium metals [41]. The anode reaction for lithium metal is



2.4 Materials and system tested in this work

The physical layout of cells used in this work is illustrated in Fig. 2.1. During discharge Li^+ ions move through a separator from the anode to the cathode while during charge the direction is reversed. Electrons during discharge move from the anode to the anode's copper current collector and then through an external circuit to the aluminum current collector and from there through the cathode to reaction sites. This is shown in Fig. 2.1. During charge the electrons move the opposite direction. The porous separator mechanically and electrically separates the anode and cathode.

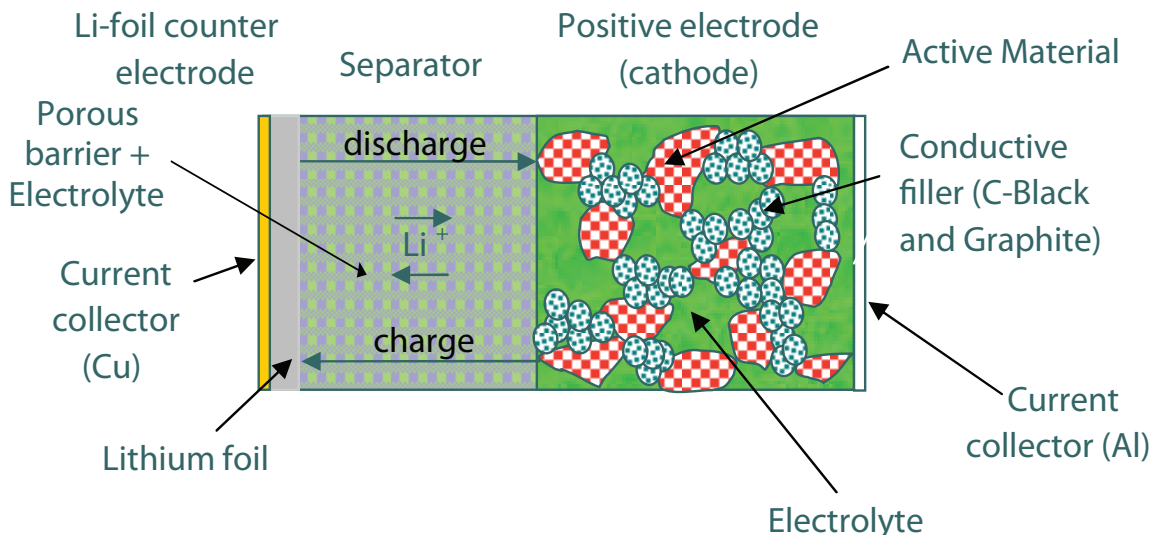


Figure 2.1: Schematic of porous cathode cell studied in this work. Dimensions are not to scale.

The cathode is composed of LiCoO_2 and carbon black bound together by polyvinylidene fluoride (PVDF). During commercial fabrication the dry components of an electrode are generally mixed with 1-methyl-2-pyrrolidone fluoride (NMP) to form a slurry. The slurry is applied to a metal foil current collector and smoothed to a uniform film thickness. The resulting film is then dried under vacuum to evaporate the NMP. Subsequently films are calendered to desired thicknesses to achieve desired porosities. Cathode, anode, separator, and electrolyte are hermetically packaged to make an electrochemical cell.

LiCoO_2 is the primary cathode material explored in this work due to long commercial usage and its particle size being large enough to be observable with focused ion beam (FIB) and scanning electron microscope (SEM) instruments. In this study we tested commercial electrode films made with commercial-grade LiCoO_2 . We also fabricated similar films at BYU with similar commercial-grade LiCoO_2 .

Generally the physical mechanisms occurring during charge and discharge can be thought of in terms of ionic transport, electronic transport, and reactions. During charge or discharge,

these physical mechanisms create voltage losses within the cell known as overpotentials [4]. The magnitude of these different cell overpotentials depends on the physical mechanisms as well as the dependence of these mechanisms on the microstructure, cell location, and the materials at each location within a cell. For example, the overpotential for a surface reaction depends on intrinsic kinetics as well as the availability of electrons and ions. Due to ion concentration gradients as well as electric potential gradients, different electrode locations have varied availability of electrons and ions. The mathematics that can be used to describe these cell resistances are described in depth in literature [2, 4–6], and some resistances are described in Chapters 3-5.

Chapter 3

Cross-sectional imaging and ionic transport measurements

3.1 Introduction

To better understand and predict electron and ion transport in porous electrodes it is necessary to determine and characterize the electrode microstructure. In order to do this, the porous structures of battery cathodes were imaged through focused ion beam (FIB) planarization and scanning electron microscopy (SEM). SEM images were then analyzed to determine significant structural characteristics. These structural characteristics were used to develop 3D reconstruction techniques described in Chapter 4. The goal of reconstruction work is to generate accurate recreation of structures, which can then be used to predict desired physical performance.

Validation of 3D reconstruction and transport models entailed experimentally finding the ionic transport properties of films [7], which is described in this chapter. The imaging and transport experiments were performed on commercially made LiCoO_2 cathode films that were calendered to different porosity levels.

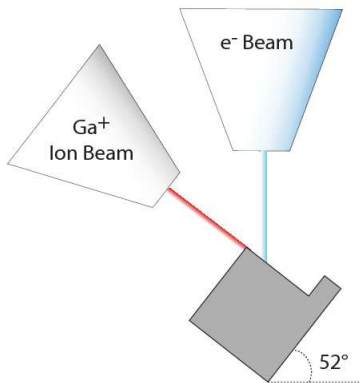


Figure 3.1: Schematic diagram of relative sample and beam orientations in a dual beam FIB instrument.

3.2 Characterizing structure

The most common way of quantitatively characterizing the microstructure of materials is through stereological methods that take measurements from planar 2D slices through the material, and, using statistical methods, extrapolate these results to the 3D structure. Many composite materials, including those found in modern battery materials, are difficult to section properly to reveal a single 2D plane of material. Polishing of these materials often results in particle pullout, and cryo-cracking only reveals a non-planar interparticle fracture path. However, new analysis and sample preparation tools have now made it possible to more easily create cross-sections that are appropriate for stereological image analysis. Specifically, dual beam FIB, shown in Fig. 3.1, combines a traditional SEM used for imaging with a focused ion beam that can be used to mill away and create cross sections through the material. The resulting images can then be processed to measure varying microstructural properties including volume fractions and interfacial areas.

In some material systems, it is possible to take this process further by taking consecutive, closely spaced slices to create a 3D image of the material. Of particular note, the

FIB/SEM method has been used to image solid oxide fuel cells [42, 43] and more recently Li-ion cathode active material particles [44]. However, in these cases the image processing of the consecutive slices was greatly assisted by use of backfilling materials. In this work no appropriate backfilling material was found that would not significantly alter the morphology of the LiCoO_2 films and/or provide contrast between the pore areas, LiCoO_2 particles, and the carbon domains, leading to difficult image segmentation (as discussed below). Other possible imaging methods would not provide significant image resolution (such as optical microscopy) or would not provide a large enough field of view (electron tomography). X-ray tomography is also a promising technique for determining electrode structure but has not yet been explored in relation to cathode films.

3.3 Experimental electrodes

The cathode films imaged in this work were made under contract by Saft America (Cockeysville, MD). One continuous film was sequentially calendered to differing degrees to obtain 4 different porosity values according to our specifications. The Saft cathodes were composed of 94.5% LiCoO_2 , 2.0% carbon black, and 3.5% polyvinylidene fluoride (PVDF) by dry weight. The volume fractions of the raw materials and the porosity, were estimated from the density of each constituent as well as the measured average film thickness. After post-calendering relaxation, the four different films exhibited dry-state porosities of 34%, 38%, 45%, and 51%, respectively. Cathodes were cast on both sides of the aluminum current collector.

For some of the electronic experiments described in Chapter 6, the cathode films were removed from the aluminum current collector. In order to do this on one side, the cathode film was removed with NMP, and then the aluminum was dissolved in gallium leaving a free-standing cathode film. This free-standing cathode film was used for electronic measurements.

Energy-dispersive X-ray spectroscopy was used to verify that the gallium had removed the aluminum current collector. We found that on films where aluminum was removed with gallium that aluminum was not found. Less than 1% of gallium was left on the delaminated surface.

Our estimate of overall porosity is obtained from a constituent volume analysis:

$$\varepsilon = 1 - \rho_{\text{film}} \sum_i \frac{w_i}{\rho_i}, \tag{3.1}$$

where ρ_{film} is the dry film density, w_i is constituent dry mass fraction (given above), and ρ_i is constituent intrinsic density. The dry film density is obtained from measurements of mass per electrode area and average film thickness, with corrections for mass and thickness of aluminum current collector. The intrinsic densities were taken to be 5.10 g/cm³ for LiCoO₂, 1.98 g/cm³ for carbon black, and 1.77 g/cm³ for PVDF, consistent with published values [45–51]. All four films had the same mass per area, and so the change in film thickness with calendaring was the single parameter that determined ε in Eq. 3.1. The film porosities reported above were determined independently by our research team as well as by Saft America and were in agreement.

3.4 Experimentally determining ionic transport

Thorat et al. [7] worked out a method of determining the effective ionic pathways within a porous electrode film. We used the same method to determine the ionic transport properties of the Saft America films as well as films we created. A brief overview of the ionic transport experiment is described here.

The complicated ionic pathways within a porous cathode can be described with an effective geometric parameter, namely tortuosity τ [52]. Tortuosity corrects the transport

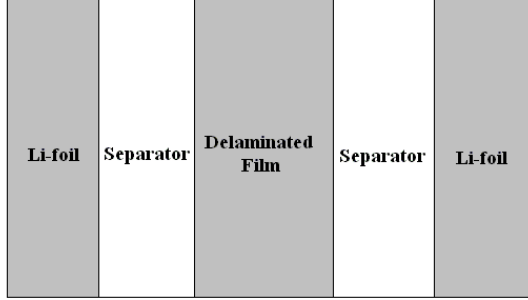


Figure 3.2: Schematic of a symmetric cell geometry for testing both porous-electrode films and simulated carbon domains. The separator area could be composed of one or multiple separators.

properties of electrolyte conductivity and diffusivity with the same functionality:

$$\kappa^{\text{eff}} = \frac{\kappa \varepsilon}{\tau}, \quad (3.2)$$

$$D^{\text{eff}} = \frac{D \varepsilon}{\tau}, \quad (3.3)$$

where κ^{eff} and D^{eff} are the effective conductivity and diffusivity, κ and D are the intrinsic conductivity and diffusivity (of the electrolyte in this case), and ε is the volume fraction of the conductive phase (pore in this case).

Tortuosity values for the films were measured using a polarization-interrupt experiment (otherwise known as restricted-diffusion experiment) [7]. This experiment involved creating a symmetric cell as shown in Figure 3.2. In a symmetric cell, the free-standing film was placed between the two lithium electrodes. The free-standing film was electronically isolated from the Li-foils by three separators on each side. The free-standing films tested in this work were either composed of cathode mixtures of LiCoO_2 , carbon black, and binder or simulated carbon domains which just had carbon black and binder.

In order to determine the ionic pathways of porous films, polarization-interrupt tests were done using a battery tester (Maccor 4300, Maccor Inc.). Several conditioning cycles were performed on the symmetric cells tested in order to form stable solid electrolyte interfaces

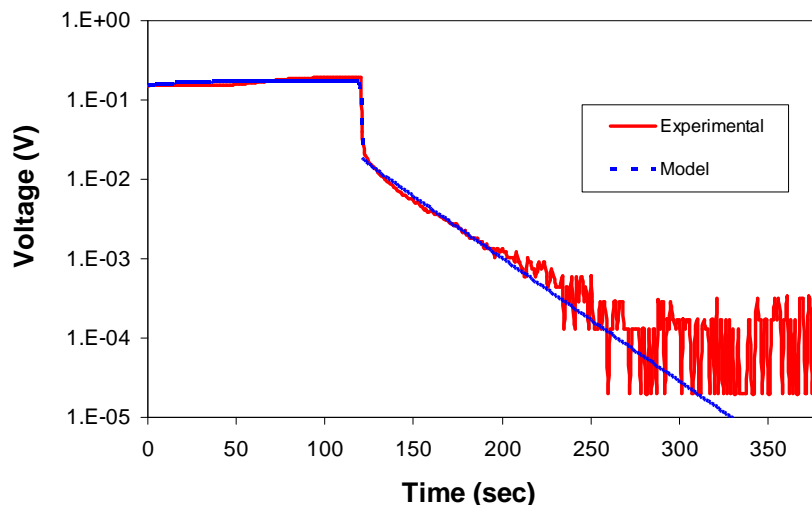


Figure 3.3: Model-experiment comparisons for galvanostatic polarization ($t < 120$ seconds) at a constant current of 1.25 mA cm^{-2} , followed by the relaxation ($t > 120$ seconds). The free-standing film being tested was a Saft cathode with 34% porosity.

(SEI) on the lithium foil electrodes. Each conditioning cycle involved passing a constant current of 0.5 mA cm^{-2} for 10 minutes followed by a 3-minute rest period. Each cycle reversed the current direction from the previous cycle. The polarization-interrupt test then was done by applying a constant current for 2 minutes to set up a concentration gradient in the cell. Four different constant currents were used in the polarization-interrupt tests. These currents were 2.5, 1.25, 1.0, and 0.75 mA cm^{-2} . After the constant current was applied, the symmetric cell was allowed to relax by interrupting the current until the cell potential approached zero. Then the current direction was reversed for 2 minutes and followed by another interruption of current. The relaxation of the concentration gradient was observed in terms of a symmetric cell-potential decay with time as shown in Figures 3.3 and 3.4. Voltages are plotted logarithmically versus time.

The model developed to interpret the polarization relaxation results was a 1D model which used the appropriate electrochemical transport and kinetic expressions as has been

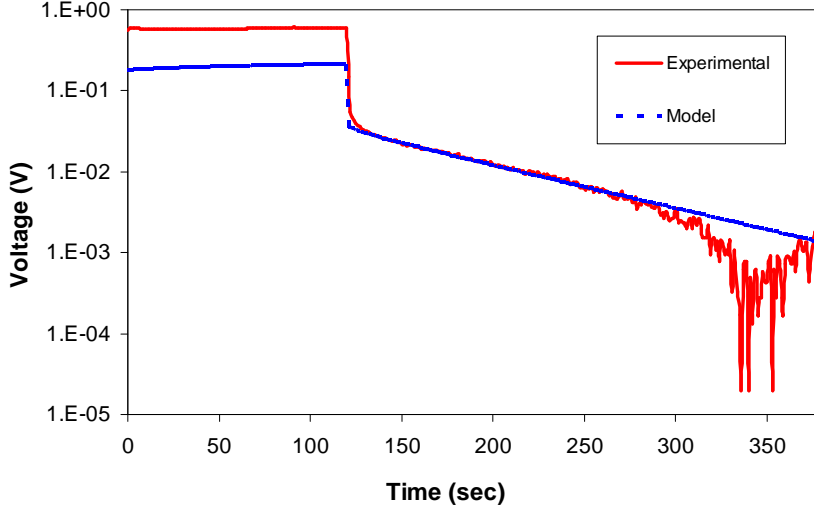


Figure 3.4: Model-experiment comparisons for galvanostatic polarization ($t < 120$ seconds) at a constant current of 1.25 mA cm^{-2} , followed by the relaxation ($t > 120$ seconds). The free-standing film being tested was a 46:54 binder-to-carbon black mixture.

described previously [2, 5–7]. These equations were implemented and solved using a finite-element package (COMSOL Multiphysics 3.5a) as described previously [2, 7]. We assumed in this work that because the free-standing films were electronically isolated, they did not react electrochemically. This meant that only ionic transport was responsible for the polarization relaxation slope.

Charge transfer through the liquid phase was modeled with the governing equation

$$\frac{\partial i}{\partial x} = 0, \quad (3.4)$$

where i is the superficial current density in the liquid phase, and x is the position in the direction normal to the electrode surfaces.

Assuming a binary electrolyte, no convection, and concentrated solutions with a constant cation transference number t_+^0 , the current in the electrolyte can be expressed in a particular region as

$$i = -\kappa_{\text{eff}} \frac{\partial \phi}{\partial x} + \frac{2\kappa_{\text{eff}} RT}{F} (1 - t_+^0) \frac{\partial \ln c}{\partial x}, \quad (3.5)$$

where ϕ is the electric potential, R is the gas constant, T is the temperature, F is the Faraday's constant, and c is the electrolyte concentration. The appropriate effective conductivity, κ_{eff} varied depending upon which domain (pore or carbon) was being modeled.

Diffusion in the liquid phase was modeled using the continuity equation for mass transport

$$\varepsilon \frac{\partial c}{\partial t} = -\frac{\partial N}{\partial x}, \quad (3.6)$$

where N is the superficial molar flux of cations through a region and is calculated by

$$N = -D_{\text{eff}} \frac{\partial c}{\partial x} + \frac{it_+^0}{F}. \quad (3.7)$$

The effective diffusivity D_{eff} varied depending on the domain being modeled.

A 1 mol dm⁻³ mixture of LiPF₆ in 1:1 (w:w) ethylene carbonate/ethyl methyl carbonate (EC/EMC) was used in the experiments. Intrinsic transport properties of this electrolyte mixture were obtained directly or estimated from literature and have been summarized by Thorat et al. [7].

As mentioned before, the change in potential during relaxation matched the concentration gradient in the symmetric cell. Matching the potential polarization at the lithium ion foils was not the goal of the model, which is why the voltages of the model and the cells don't necessarily match during the constant-current polarization. The separator material has been well-characterized both by us and by other researchers; separator tortuosity is known and was included in the model [7]. The differing relaxation slopes are thus fitted by changing model tortuosity of the free-standing film. As seen in Figures 3.3 and 3.4, after this was done the slopes of the model and experiment matched until the voltage became very small. Once voltages became very small the electrochemical noise caused from instrument limitations resulted in small voltage variations that we did not try to model.

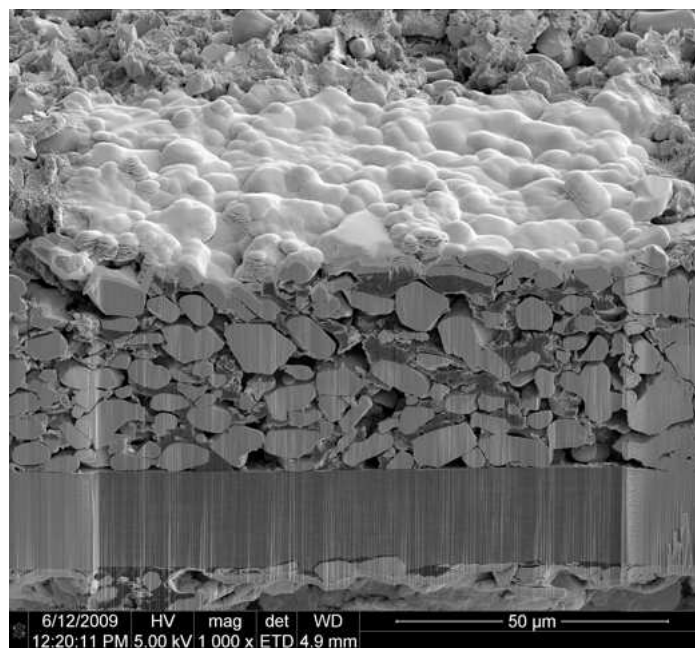


Figure 3.5: SEM image of a porous cathode including ablated planar section. The aluminum current collector (horizontal dark band near bottom of image) is coated on both sides. A layer of platinum (bright region at the top) is applied to reinforce and maintain the edge while sectioning.

3.5 FIB imaging

Determining the structure of porous electrodes is challenging, because the high depth of field of SEM causes the interior of pores behind the ablated plane to be imaged with nearly the same brightness as the surface of the cross-section (see Fig. 3.5). Proper accounting of microstructure can be obtained by segmenting the image (the process of clearly labeling each region within the image [42, 43, 53, 54]). Infiltrating the pores with a different type of solid than the electrode materials can greatly assist in this process, but only if the infiltration does not change or obscure the microstructure. If the process of segmentation cannot be highly automated, hand segmentation of the images is required, wherein the outlines of the regions of interest are manually traced by the user, which leads to a significant amount of user interaction and time. In the case of full FIB/SEM 3D reconstructions with hundreds of

images, these labor constraints become unworkable, especially when much of the information required can be extrapolated from 2D images through the use of models.

Sectioning and imaging were done with a dual-beam FIB/SEM instrument (FEI Nova 600 NanoLab) by our collaborators at the Naval Research Laboratory (NRL). Samples were frozen in liquid nitrogen and fractured to reveal rough cross sections. Films were then ablated to make a planar cross-section through the film with the gallium-ion beam. After ablation, images were obtained with a scanning electron microscope (SEM). Fig. 3.5 shows an ablated region of a double-sided LiCoO_2 electrode film. Ablated regions in the images were segmented by first filtering the image with photo software and segmenting based on the color of the image. Further differentiating between LiCoO_2 particles, carbon domains and pores was accomplished by modifying individual pixels by hand. Initial segmentation procedures were explored at BYU. The final segmented images were produced at NRL.

The resulting segmented images made at the NRL of the four commercially made electrodes are shown here as Fig. 3.6 and are the basis for subsequent analysis I performed. While each image is $100\ \mu\text{m}$ wide, with calendaring the thickness of the cathodes decreases dramatically. Distances between active material particles similarly decrease. In Figs. 3.5 and 3.6 it can be observed that the carbon particles, which have sizes on the order of $0.1\ \mu\text{m}$, agglomerated into rather homogeneous and discrete carbon domains. Below we give additional analysis to understand these carbon domains, including their composition and effect on overall ionic pathways.

Of note is how the FIB/SEM images show distinct carbon particles agglomerates. In general carbon black particles are around $0.1\ \mu\text{m}$ in diameter. Figure 3.6 shows how these small carbon particles, bound together by the binder, are creating large carbon domains. Up to this point researchers have largely been ignoring carbon as a distinct phase in structural models [55]. Instead they assume that the carbon forms a uniform coating on the surface

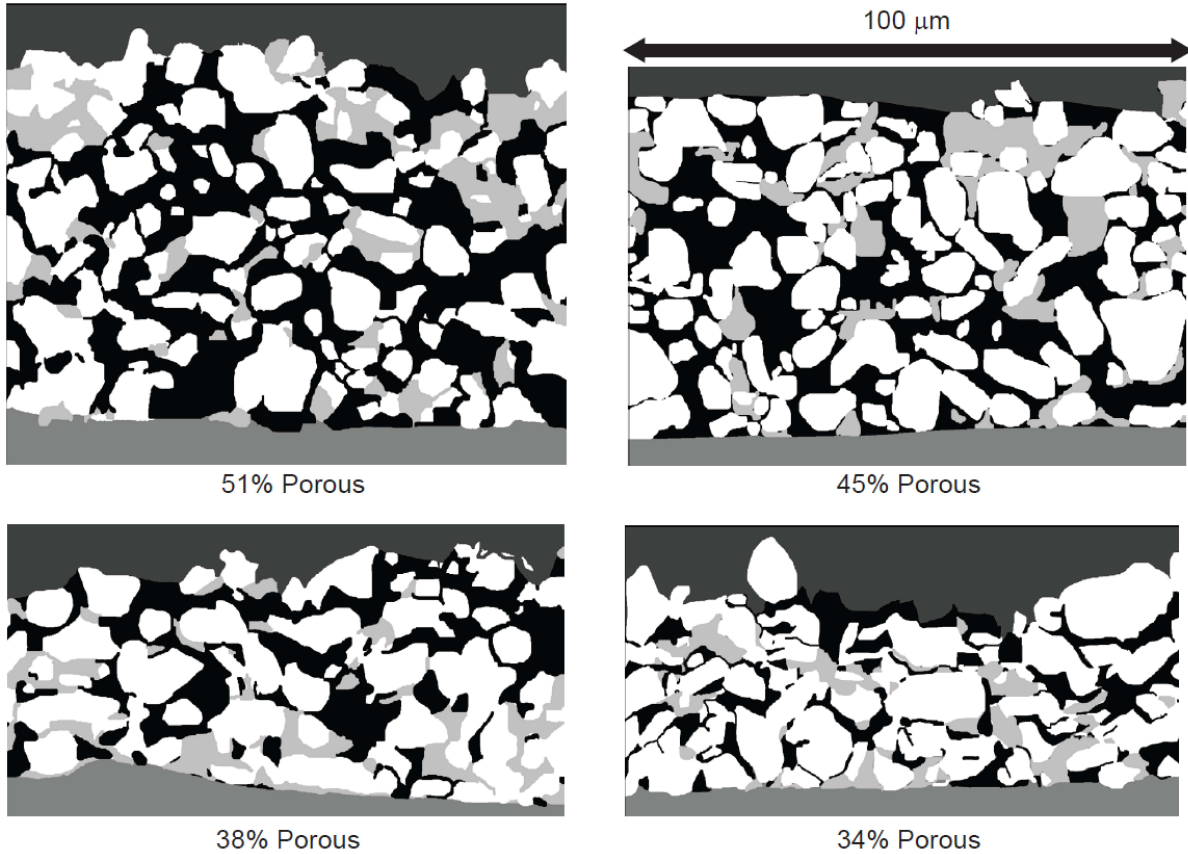


Figure 3.6: Segmented FIB/SEM images of electrode films with varying porosities. White represents active material domains, light gray represents carbon domains, black represents pore domains, and the top dark gray and bottom gray represent the exterior volume and aluminum current collector respectively.

of active material particles. This in turn leads to a model in which the active domains are given an effective conductivity that differs from intrinsic conductivity.

In order to automate the segmentation of FIB/SEM images better image contrast of the pores needs to be created. Better contrast may be accomplished by adding a pore-filling material. We tried materials such as an epoxy resin, sulfur, and cyanoacrylate (superglue). We and others have found that these materials, while making easier the segmentation and reconstruction of active particles, generally obscure the presence and morphology of carbon domains and conflates them with the surrounding pores [56]. We therefore chose not to use

pore-filling materials in this work after some initial attempts. However, recent work has claimed adequate contrast results by using silicon elastomer resin in LiFePO_4 electrodes [57].

3.6 Structural metrics

Rendering a 3D structure from a large sequential series of 2D slices is a reasonably routine operation, though in the case of FIB/SEM images this is still time consuming and difficult [42, 43]. Therefore a method for predicting representative 3D structures from a more limited set of 2D images would be useful.

In order to know how representative a predicted structure is, one must choose one or more image or structure metrics to compare. Russ and Dehoff summarized different general image analysis metrics in terms of the type of sampling techniques, namely point, line, or plane probes [58]. Specific image metrics to recreate 3D structures have been summarized and used by Torquato [59]. We looked at different metrics that can be obtained from a 2D image, from the most fundamental metric of the volume fractions of the phase domains to more complicated line probability distributions. We found as did Torquato [60] that 2D information alone is not sufficient to fully reproduce 3D geometries. However, the reconstruction methods used here nevertheless produced 3D geometries deemed reasonable at this stage of the work. We deemed it reasonable because the models created structures with the correct number of connections between phases (which is important for determining electronic resistances) and placed material phases at approximately the correct distances (which is important for determining both ionic and electronic transport).

We found that locally obtained image metrics such as volume fractions (a point-probe technique) and nearest-neighbor probabilities (a line-probe technique) yielded satisfactory 3D reconstruction results with a minimum of computational cost. Longer-range statistics such as the line probability distribution, which is the probable length of a phase sampled

by line probes [58], were found to be less useful in reproducing 3D structure. Another non-local metric related to interdomain line curvature was also explored. Some metrics such as mean caliper diameter and plane-probe-type methods were not explored in this work, partly because 2D images do not support these techniques [58].

Volume fraction analysis of electrodes. Analysis of the FIB/SEM images gives insight into how the structure of the cathodes changes with cell porosity. Fig. 3.7 shows the volume fractions of the different domains as a function of overall porosity. Domain identities here and in the discussion below are denoted by A for active material, P for pore, and C for carbon. We found that the 38% porosity image (Fig. 3.6) was anomalous for a number of properties, such as having volume fractions and contact areas similar to those for the 51% porosity image and showing substantial nonuniformity of the current collector, see 38% porosity image in Fig. 3.6. We suspect that the cryo-cracking process used in sample preparation may have modified the sample in this one case. As a result of the 38% porosity data being similar to the 51% porosity data, we excluded the segmented image for 38% porosity from Fig. 3.7 and subsequent analysis in the present work. However, including the 38% porosity data in subsequent analysis did not significantly change the results of this work. In future work we hope to obtain images of 38% porosity electrodes.

While both A and P domain volume fractions in Fig. 3.7 change with overall porosity, surprisingly the carbon domain volume remains fairly constant and at a value far above the volume of carbon black added to the cells. Moreover, the apparent pore volume fraction (curve P) is below the overall porosity of the electrode. Therefore it can be inferred that the imaged carbon domains are composed of not only carbon but also binder and micropore.

The breakdown of dry composition versus the image domain volumes for the 51% porous electrode are shown in Table 3.1. The raw material volume fractions are obtained in a manner consistent with Eq. 3.1. By analyzing the difference between the imaged pore volume versus the volume of pore it was found that the carbon domains are 63% porous on average and

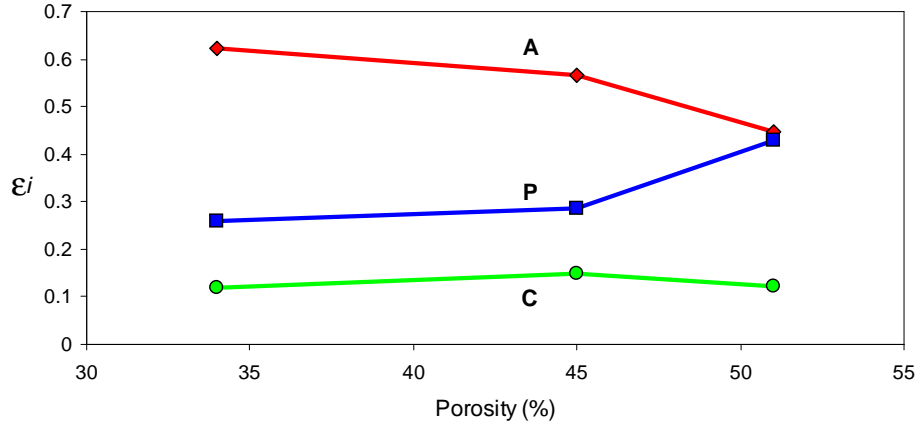


Figure 3.7: Domain (A, P, C) volume fractions versus porosity of electrodes. Lines are to guide the eye.

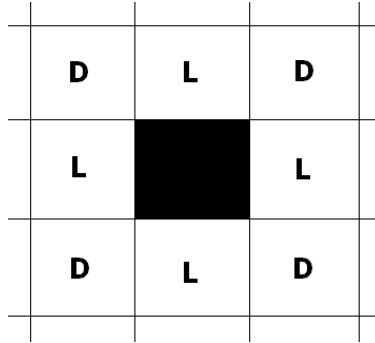


Figure 3.8: Lateral neighbors (L) and diagonal neighbors (D) for a central pixel.

contain most of the electrode binder. This is similar to the porosity of carbon black without binder that is not under pressure, which is between 68% to 73% porous. Binder likely helps lower the porosity of the imaged carbon domains.

Contact probabilities. In analyzing an image or structure, we divide the domain into a matrix of discrete nodes—square pixels in 2D, cubic voxels in 3D—each of which has length scale δ . A determination of node-to-node contact probabilities can be done by summing up all the nearest neighbor contacts of a given type and then dividing by the total number of contacts. We looked at lateral nearest-neighbor pixels (closest pixels in the x and y

Table 3.1: Calculated volume fractions of raw materials and domains for 51% porous electrode.

Raw material balance		Image segmentation	
Identity	Vol frac	Domain i	Vol frac ε_i
Pore	0.510	P (pore)	0.429
Active material	0.427	A (active material + binder)	0.448
Carbon	0.023	C (carbon + binder + micropore)	0.123
Binder	0.040		

directions) and diagonal nearest-neighbor pixels, as shown in Fig. 3.8. In a 2D image, there are four lateral and four diagonal nearest neighbors to a given pixel, while in 3D space, there are six lateral and twelve diagonal nearest neighbors.

The lateral and diagonal nearest neighbors correspond to the first two discrete points ($r = \delta, \sqrt{2}\delta$) in the radial distribution function $g(r)$, where r is the distance between points. The radial distribution function is a normalized probability of finding particular neighbors at a particular distance [61]:

$$g_{ij}(r) = \frac{P_{ij}(r)}{\varepsilon_i \varepsilon_j}, \quad (3.8)$$

where $P_{ij}(r)$ is the observed probability that two points separated by distance r happen to be of domain types i and j . There are $\frac{1}{2}(n+2)(n-1)$ independent P_{ij} functions for an n -component (or n -phase) system. ε_i is the volume fraction of domain i and equals the probability of finding that domain at any single point. The basis for our extrapolation procedure is that, given adequate sampling, properly normalized radial distribution functions are the same for both a 2D cross section and a full 3D structure originating from the same isotropic material. Whether or not the cathodes are isotropic after non-isotropic processes

such as calendering is not known. Not enough data were collected to assess the level of isotropy of cathodes.

Making a 3D reconstruction having the same resolution as our FIB/SEM images (i.e. each image pixel being represented by a simulation node) with current computer capabilities only would produce a volume containing a few active material particles. This is because a standard personal computer at this time can handle a cubic volume with edge length of around 220 nodes and prove solutions within a day or two of solving time. If each node length δ corresponded to the raw image resolution of $0.065 \mu\text{m}$, the simulated cube would only have an edge length of $14.3 \mu\text{m}$. Therefore, before analyzing neighbor pairs we degraded the FIB/SEM image resolution by grouping pixels together and assigning each group a single domain identity based on a random selection of one of the underlying pixels. Coarse-grained image statistics allowed us to simulate corresponding cathode structures of sufficient size (i.e. over $40 \mu\text{m}$ cube length) to analyze transport properties.

We define lateral and diagonal contact probabilities as $P_{ij}^L = P_{ij}(\delta)$ and $P_{ij}^D = P_{ij}(\sqrt{2}\delta)$ respectively; these can be further categorized by interdomain ($i \neq j$) and intradomain ($i = j$) contact. Contact probabilities change with resolution or pixel size as shown, for example, in Fig. 3.9 for the case of lateral and diagonal contacts in the 34% porous electrode. Curve AA represents the fraction of neighboring pixels both belonging to active material domains, AP represents active material and pore domains adjacent to each other, and the remaining follow the same logic. As resolution approaches zero, all contact probabilities approach trivial values. In particular, interdomain contact probabilities go to zero, and intradomain contact probabilities approach their respective volume fractions ε_i [62]. The contact probabilities tend to be linear in δ , meaning that the interfaces are not generally fractal at these length scales [63]. The lateral and diagonal contact probabilities for all imaged electrodes followed these trends. Therefore when a simulation is matched to an image at a finite resolution, it is the deviation of contact probabilities from the zero-resolution limit that is the important

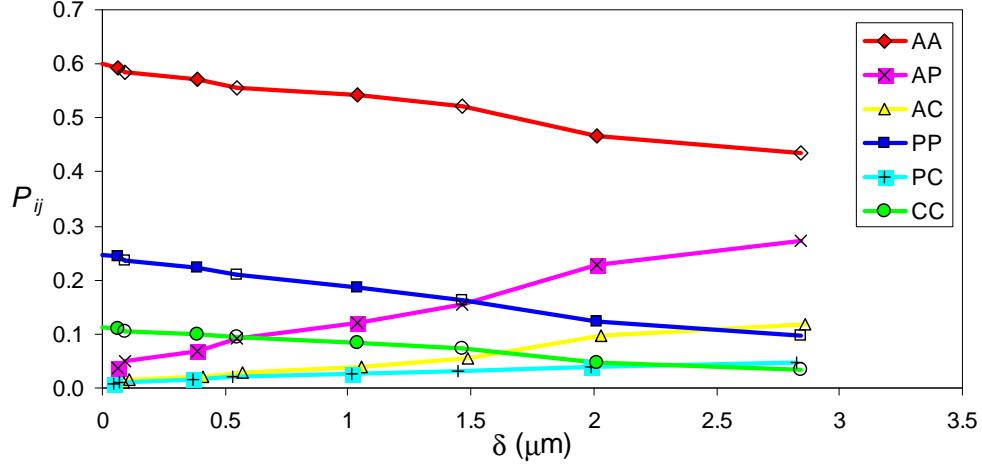


Figure 3.9: Interdomain and intradomain neighbor contact probabilities versus distance between pixels, generated from the FIB/SEM image at 34% porosity (Fig. 3.6) and different levels of coarse graining. Pairwise labels (AA, etc.) are defined in the body text. Filled symbols indicate lateral neighbors (plotted vs. δ) and unfilled symbols indicate diagonal neighbors (plotted vs. $\sqrt{2}\delta$). Lines are a guide to the eye; some points have been horizontally offset for clarity.

metric and contains microstructural information. Also of note, for $\delta > 3 \mu\text{m}$ (not shown), the pixel size approaches the mean sizes of active particles and pores, and contact probabilities begin to lose physical significance. Therefore, there is an upper bound on any coarse-graining procedure used. Further discussion on this resolution-size concept accompanies Fig. 4.3 below.

3.7 Volume analysis of carbon domains

As discussed in the previous section, carbon domains include a significant amount of micropore volume, which means ions can travel through these domains as well as through the macro-size pores. Because the carbon domains take up a significant volume of the cathode, carbon domain ionic pathways can significantly affect overall tortuosity.

A couple of assumptions were made in analyzing the images. The first was that the carbon was not imaged in the active domains. The second was that we could experimentally determine the carbon domain porosity. We did experiments with simulated carbon domains with 1:1 and 2:1 binder-to-carbon ratios and found the porosity was consistently 52% for the 2:1 binder to carbon films and 57% for the 1:1 binder-to-carbon films. Calendering as well as changing the amount of NMP used in the preparation of the carbon films did not affect the porosity more than 5%. In the analysis presented here, we took the average of the simulated carbon domain microporosities in order to estimate the imaged carbon domain porosities.

Because conductivity of the carbon domains is highly dependent on the ratio of binder-to-carbon, the goal of this analysis is to try to determine the binder-to-carbon ratio. In order to do this, the imaged volumes were described by their component domains. This meant that imaged carbon domain ε_c^* is equal to

$$\varepsilon_c^* = \varepsilon_c + x \cdot \varepsilon_p + y \cdot \varepsilon_b, \quad (3.9)$$

where ε_c is volume of carbon, x is the fraction of pore going into the carbon domain, ε_p is the volume of pore, y is the fraction of binder going into the carbon domain, and ε_b is the volume of binder. For the other two domains, a similar volume analysis leads to

$$\varepsilon_p^* = (1 - x) \cdot \varepsilon_p, \quad (3.10)$$

$$\varepsilon_a^* = \varepsilon_a + (1 - y) \cdot \varepsilon_b, \quad (3.11)$$

where the imaged pore domain is ε_p^* , the imaged active domain is ε_a^* , and ε_a is the volume of the active material. The results of this analysis are shown in Table 3.2.

Table 3.2: Volume fractions analysis results. x is the fraction of pore going into the carbon domain. y is the fraction of binder going into the carbon. The microporosity of the carbon domains was assumed to be 0.57. R_{bc} is the ratio of binder-to-carbon.

Results				
Electrode Porosity	calculated porosity	x	y	R_{bc}
51%	0.512	0.127	0.567	0.993
45%	0.421	0.156	0.438	0.767
38%	0.520	0.105	0.386	0.675
34%	0.329	0.205	0.287	0.502
Averaged		0.148	0.473	0.734

The ratio of binder-to-carbon (R_{bc}) is given by

$$R_{bc} = \frac{y \cdot f_b}{f_c} . \quad (3.12)$$

where f_b is the dry weight fraction of binder and f_c is the dry weight fraction of the carbon.

The equations above assumed that the active domains did not have micropores, which we believe is accurate because no evidence was seen in the FIB/SEM images that suggested that the active domains were not continuous. Based on an analysis as presented in Table 3.2, we estimate that approximately 47 percent of the binder was attached to the carbon in the carbon domains. The 38% image data were consistent with volume fractions corresponding to 51% porous cells. The 38% image interdomain interactions were consistent after appropriate volume fraction adjustment with 51% porosity cells. It is believed that section imaged in the 38% Saft film had either relaxed back to the 51% porosity or had somehow not been calendered.

We can learn from Table 3.2 that on average the binder-to-carbon ratio of the imaged films was around the 1-to-1. The effects that this has on the electronic conductivity of the cells is discussed in section 6.8.

3.8 Experiments for determining ionic pathways in carbon domains

To better understand the ionic pathways in the carbon domains, we created simulated carbon domains and measured their tortuosities with a symmetric cell [7]. The simulated carbon domains were created out of carbon black and PVDF cast on an aluminum current collector. The ratio between carbon black and PVDF was varied between two binder-to-carbon ratios. Simulated carbon domains were made with different ratios of carbon to binder, while maintaining approximately the 63 percent microporosity obtained from image analysis. One simulated carbon domain's composition was made with a volume fraction of binder that would simulate 100% of the binder in the tested electrodes being bound to the carbon (63:37 binder-to-carbon by weight). The other symmetric cell composition simulated 50% of the binder in the tested electrodes being bound to the carbon (46:54 binder-to-carbon by weight).

Symmetric cells were built and tested as we have previously described above. It was found that the simulated carbon domain with 63:37 binder-to-carbon produced a domain tortuosity of 16.5, while the simulated carbon domain with 46:54 binder-to-carbon produced a domain tortuosity of 9.6. These tortuosities produce effective ionic conductivities and diffusivities for the carbon domains of 3 to 6 percent of the intrinsic electrolyte conductivity. Overall Saft electrode tortuosities were around 3 (see Chapter 4), which means the tested carbon domains have significant ionic restrictions when compared to the overall electrodes. Overall Saft electrode tortuosity compared well with prior porous electrodes tested at BYU [7].

3.9 Conclusions

We found using FIB/SEM imaging that the essential structural features of LiCoO_2 cathodes could be quantified. These features are related to the electrode composition and fabrication conditions. The constituent materials formed domains that could be identified in FIB/SEM images. We found that the majority of binder and carbon clumped together into discrete domains, which occupied spaces between the active material particles.

From analysis on segmented SEM images we determined effective pairwise interactions between different domains. We found that these interactions depend upon the structure of the electrode as well as the resolution at which the images were analyzed. Interactions between different domains can be described in terms of probabilities or energies.

Experiments were used to quantify the ionic pathways within simulated carbon domain agglomerates. We found that although these carbon domains are mostly porous, the ionic pathways through them are highly tortuous. This means carbon domains highly restrict ionic pathways within a cathode. To better understand the trade-off between the ionic and electronic resistances due to these carbon domains, in Chapter 5 experiments are described which were used to determine the electronic properties of these carbon domains.

Chapter 4

3D microstructure models

4.1 Introduction

Microstructure models were developed in this work which could predict 3D microstructures from 2D images. Two different microstructure models were used to predict 3D microstructures from the 2D image metrics discussed in Chapter 3. The first method, the dynamic particle packing (DPP) model is a particle-based Lagrangian-type approach where domains were simulated by agglomerates of spheres which move collectively under Newton's law of motion. The second method, the stochastic grid (SG) model used a Eulerian-type approach where domain structures were created on a grid. The Monte Carlo approach was used to generate configurations by swapping the material identities of nodes.

These two methods primarily used the domain volume fractions and contact probabilities obtained from the images to regress their model parameters. Both methods yielded similar ionic transport results even though they were developed from very different reconstruction methodologies. Both models were implemented with periodic boundary conditions to best reproduce bulk electrode structure from a minimum simulation volume. Also, both treated

the carbon domains as a homogeneous phase such that individual carbon black particles are not considered.

4.2 Background

Several prior workers have attempted to directly model the microstructure of porous battery electrodes. Sastry and coworkers have explored models based on a random packing of spherical or ellipsoidal particles [64, 65]. Siddique and Liu recently proposed a model that uses random seeding and growth of particles in order to generate 3D structures [66]. Smith et al. created a 2D electrochemical model of electrodes as a step toward understanding how particle-particle interactions determine cell performance [67].

The grid- and particle-based models developed in this work use physical parameters that were regressed by matching properties of predicted 3D structures to properties from 2D images. Physical metrics for comparison include domain volume fractions (carbon, active, and pore) and interdomain contact probabilities. Further validation of the DPP and SG models came from comparing predicted ionic tortuosity to experimental values. We found that reasonable 3D reconstructions are possible solely by use of 2D cross sections and that the models can assist in understanding how electrode structure affects ionic transport performance.

4.3 Dynamic particle packing model

The first reconstruction method, called the dynamic particle packing (DPP) model, was an attempt to generate the rough active material particle shapes and carbon domains with agglomerates of overlapping spheres [59]. Sphere interactions were represented with Lennard-Jones interaction potentials, and configurations were generated with a molecular dynamics-type simulation code [68]. The molecular dynamics approach is used by analogy, as length

(and time) scales in the simulation are mesoscopic rather than atomic. The interdomain contact probabilities and domain volume fractions found from the 2D images at different porosities were matched by adjusting interparticle pair interactions. The same interparticle pair interactions were used to model a range of porosities. This was done by running the DPP model with different box volumes but the same number of particles and particle sizes.

There are two major benefits to the DPP model. The first benefit comes from the molecular dynamics approach. The DPP model allows simultaneous or collective motion of particles based on Newton’s law. Particle motion in time could allow for a reconstruction to simulate electrode fabrication steps such as solvent evaporation and electrode calendaring, and possibly morphology changes during cell operation. The second benefit comes from the simplicity of the parameters needed. The Lennard-Jones potential function used here requires only two parameter values per type of particle: σ and ϵ , which represent the size of the particle and the attractive energy well depth, respectively. The form of the Lennard-Jones potential function is [69]:

$$\phi_{ij}(r) = 4 \epsilon_{ij} \left[\left(\frac{\sigma_{ij}}{r} \right)^{12} - \left(\frac{\sigma_{ij}}{r} \right)^6 \right], \quad (4.1)$$

where indices i and j represent particle identities. Particles of different types (i.e. active material and carbon), as well as particles of different size, will have different LJ parameters. Cross interactions are given by standard combining rules [70]:

$$\sigma_{ij} = \frac{\sigma_{ii} + \sigma_{jj}}{2}, \quad \epsilon_{ij} = \sqrt{\epsilon_{ii}\epsilon_{jj}}. \quad (4.2)$$

The agglomeration of spherical particles into complex shapes is controlled by the relative degree of attraction between similar and dissimilar particles.

One disadvantage of the DPP model is that appropriate DPP model parameters could be determined only indirectly, meaning there is not a direct correspondence between image metrics and DPP model parameters. When changing the parameters, we observed predictable

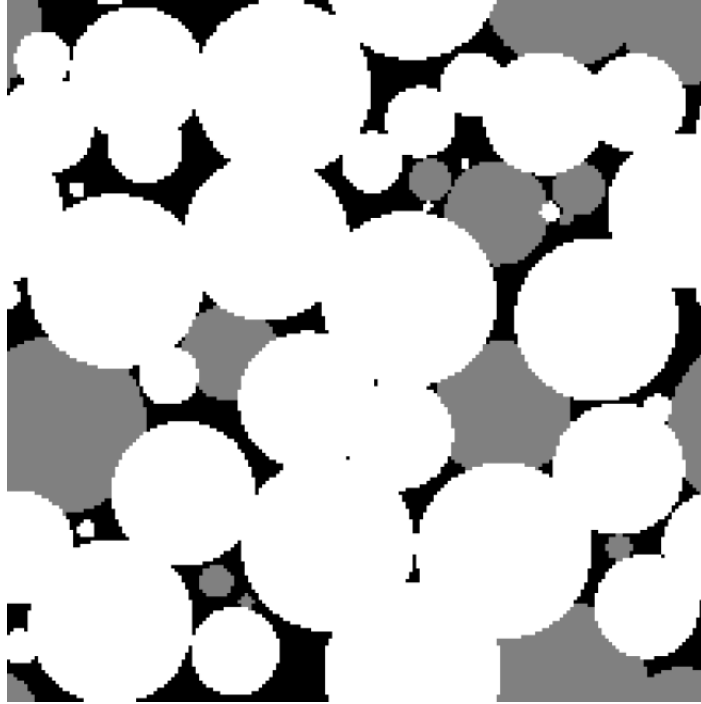


Figure 4.1: $30\ \mu\text{m} \times 30\ \mu\text{m}$ slice from a DPP model configuration at 34% porosity. White represents active material domains, gray represents carbon domains, black represents pore domains.

trends, such as the effect on simulated domain volume fractions. Nevertheless, an iterative method had to be used to determine appropriate model values to use. Also, one set of parameters was not fully adequate to describe the structures at the four different porosities.

A second disadvantage to the DPP model is poor reproduction of the particle shapes seen in the images. Fig. 4.1 shows a cross section from the simulated structure of a 34% porous electrode. To try to increase surface roughness, a distribution of particle sizes was used to simulate the active and carbon phases. The idea was for smaller spheres to agglomerate on the surface of larger spheres thereby increasing the roughness of the particles. However, the number of smaller spheres necessary to increase roughness is large and most of the small spheres tended to get obscured by the larger spheres thereby failing in their purpose. Because computational costs increase considerably with number of simulated spheres, the best

result we were able to obtain with the DPP model was interfacial areas (or interdomain contact probabilities) which were approximately one third of the imaged values for a particular resolution. We nevertheless were able to match imaged volume fractions as well as relative interdomain contact probabilities, meaning the ratios between the different P_{ij} ($i \neq j$) approximately matched the image values.

The following parameters were used for the baseline DPP model and are based on empirical adjustment. All ϵ_{ii} values were fixed to the same value, $2k_B T_0$, where T_0 is an arbitrary temperature. Particle masses were also set to a constant arbitrary value m_0 , since masses do not affect the equilibrium distribution evaluated at this stage of the work. DPP particle size was defined by σ_{ii} in the Lennard-Jones potential function. Both σ_{ii} for active and carbon domains followed a truncated log-normal distribution, which we found enabled the DPP model to fit relative interdomain contact probabilities. For carbon domain particles, $\log_{10}(\sigma_{ii}/\sigma_0)$ followed a normal distribution with mean -1.0 and standard deviation 0.74 and was truncated between -1.0 and 0.36 . For active material particles, $\log_{10}(\sigma_{ii}/\sigma_0)$ followed a normal distribution with mean of -1.0 and standard deviation of 0.78 and was truncated between -1.0 and 0.36 . Parameter $\sigma_0 = 4.5 \mu\text{m}$ is a length-scale parameter that can be adjusted after the simulation is completed (i.e. the entire simulation can be scaled in size) to match expected particle sizes, in this case making the largest spheres around $10 \mu\text{m}$ diameter. However, the choice of σ_0 does not affect the primary property of interest, namely tortuosity. 1000 particles were placed in a cubic box of length L per side; 275 of the particles were labeled as carbon with the rest of the particles being active material, which enabled the DPP model to match both the image carbon domain and the active material volume fractions. The box length L was adjusted for each intended porosity; for instance, 34% porosity required $L = 6.59\sigma_0$. The particles were initially placed on a regular grid in a random sequence and initialized with initial velocities that corresponded to the temperature. Particle

motion was propagated for 10^4 time steps, each of time increment $\Delta t = 0.07\sigma_0\sqrt{m_0/(k_B T_0)}$, leading to a quasi-equilibrated final configuration used as the electrode structure.

To convert a simulation snapshot to an electrode configuration (e.g. Fig. 4.1), we did two things. First, the soft LJ spheres were converted to hard spheres with diameter equal to σ_{ii} . Second, whenever a resulting carbon sphere overlapped an active material sphere, the active material took precedence. This displacement imitates the fact that carbon domains are much more compliant mechanically than active material and allowed the model to better match AC interdomain contact probabilities. The model’s interdomain contact probabilities were calculated by mapping the simulated 3D structure onto a grid. Each voxel was then assigned the identity of the domain occupying the voxel center. Nearest neighbor contact probabilities could then be calculated for comparison with a FIB/SEM image.

4.4 Stochastic grid model

As an alternative to the DPP model we developed the stochastic grid (SG) model, which can be considered an extension of the classic Ising model, which in turn is based on Monte Carlo (MC) simulation principles [71]. With the SG model, the volume is divided into nodes or voxels from the outset. Each node is assigned a single domain identity corresponding to pore, carbon, or active material, with the relative number of nodes for each domain corresponding to image volume fractions. Starting from a random configuration, a sequence of configurations is generated by evaluating trial node swaps. By swapping the domain identities of one pair of nodes at a time, the correct domain volume fractions are maintained. The proposed swaps are either accepted or rejected based on the relative probabilities of the current and trial configurations.

To generate a trial move, two sites (\mathbf{s}_I and \mathbf{s}_J) are selected randomly. A variation that we found improved the results was to ensure that both sites were located near an existing

domain boundary, i.e. each proposed site must have at least one nearest neighbor of a different domain type. This reduced the anomalous formation of isolated domains occupying only 1 node. Following site selection, probabilities are calculated. The relative probability of site I containing domain i is

$$G_i(\mathbf{s}_I) = \prod_{\mathbf{s}_K} g_{ik}, \quad (4.3)$$

where a product is made for all g_{ik} values between the central node \mathbf{s}_I and its nearest lateral and diagonal neighbors at sites \mathbf{s}_K . Index k indicates the domain identity of those neighbors. Each g_{ik} value for a given pair type is pre-tabulated from a FIB/SEM image at the same resolution as the simulation—there are 12 possible g_{ik} values for lateral and diagonal nearest neighbors, though only 10 are independent. The probability of a successful swap of domains i and j , originally located on sites \mathbf{s}_I and \mathbf{s}_J respectively, is based on the Metropolis algorithm:

$$P_{I \leftrightarrow J} = \min \left[1, \frac{G_j(\mathbf{s}_I) G_i(\mathbf{s}_J)}{G_i(\mathbf{s}_I) G_j(\mathbf{s}_J)} \right]. \quad (4.4)$$

The swap is accepted if $P_{I \leftrightarrow J}$ is greater than a pseudo-random number uniformly distributed on $[0, 1]$.

The observed probability of a configuration is related to its relative free energy. As mentioned before, the radial distribution function g_{ij} is a normalized probability of pairwise interaction. The radial distribution function can be related to a so-called potential of mean force f_{ij} by $g_{ij}(r) = \exp[-f_{ij}(r)/k_B T]$, where k_B is Boltzmann's constant and T is the temperature [61, 72]. The potential of mean force is a pairwise free energy, meaning it includes not only the direct pairwise interaction potential but also mediating or entropic effects due to other neighbors interacting with the original pair. A classic MC algorithm must use direct pairwise interactions to evaluate trial configurations (e.g., Eq. 4.4), whereas extant configurations (e.g., FIB/SEM images) can only give one the equivalent to potential of mean force. In the SG model, by letting image-derived g_{ij} values govern proposed moves, we in effect assumed that the potential of mean force can be used as a pairwise interaction

potential. This is a reasonable assumption because at small r the pairwise potential portion of f_{ij} is large compared to the entropic contribution, meaning that the potential of mean force is nearly equal to the direct pairwise potential. This near-equivalence is not true at longer interaction distances. For this reason, as well as for computational efficiency, only lateral and diagonal nearest neighbor probabilities were utilized in the SG model.

Torquato described a composite-material reconstruction strategy similar to that proposed here [59, 62]. A few differences should be noted, however. First, Torquato was reconstructing only 2-phase systems in which there are 2 independent pair distribution functions. Second, while Torquato's $S_2(r)$ function is equivalent to our $g_{11}(r)$ function (1 represents the phase of interest), it appears the second independent pair distribution function (e.g., either g_{12} or g_{22}) was not calculated or used. This has implications in fully reconstructing intradomain and interdomain connectedness. On the other hand, while only the two nearest neighbor distances are considered in our work, Torquato appears to have used pair distributions to longer range.

The SG model configuration starts in a randomized state that is then driven toward thermodynamic equilibrium (a minimum in system free energy). However, the actual imaged system is a collection of meta-stable solid particles that do not exhibit a thermodynamic minimum energy, but rather a mechanical equilibrium. A thermodynamic equilibrium means a minimum in interfacial area, which would generate unnatural agglomeration of solid phases. To compensate, we ran the model trial swaps while monitoring the sum-squared-deviation between the reconstruction and image P_{ij}^L and P_{ij}^D values. The SG run was terminated when this error difference reached a minimum, which generally happened quickly. This final configuration was then used as the electrode structure for ionic transport analysis.

It is instructive to compare the 3D reconstructions to the 2D images. In Fig. 4.2 one observes that the actual active material domain (a) has more cracks than the reconstructed

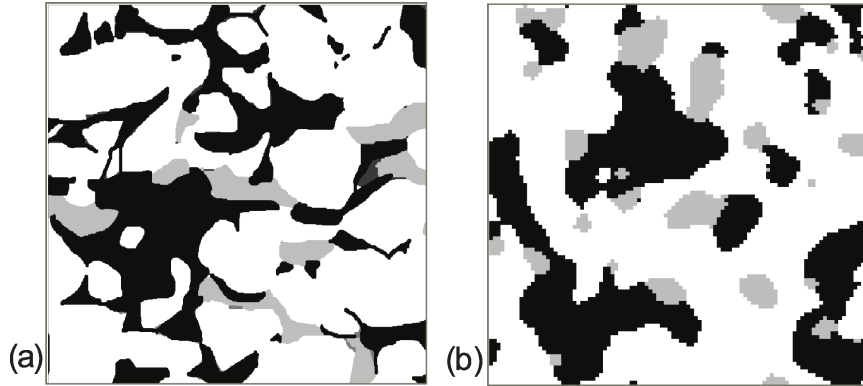


Figure 4.2: $30\ \mu\text{m} \times 30\ \mu\text{m}$ slices for 34% porosity electrode from (a) FIB/SEM image and (b) baseline SG model reconstruction (node size $0.2\ \mu\text{m}$). White represents active material domains, gray represents carbon domains, black represents pore domains.

version (b). Again, the thermodynamic propensity of the SG code seeks to minimize surface area, thereby creating active-material agglomerates that are not sufficiently segmented.

In an attempt to improve the model, we looked at a number of variations to the SG model to more closely match the image statistics. We first considered the distribution of curvatures at the interfaces between domains. A curvature metric was calculated by moving a defined number of steps along the interface and then measuring the actual distance between the starting and end points of the path. The curvature metric was coupled to the baseline SG model by alternatively generating swap moves based on improving the curvature distribution and then based on nearest neighbor contacts. However, this resulted in only minor changes to observed agglomeration and to ionic tortuosity. Another method we tried was analogous to the “Great Deluge” algorithm [59] in which the only moves accepted are those which decrease the sum-squared-deviation between the reconstruction and image metrics. Another method looked at the lineal-path function $L(r)$, defined as the probability of finding a straight line segment of length r contained entirely in a particular phase [62]. Another method used a feedback loop to dynamically perturb the pair interactions from the image-derived ones in an attempt to guide the 3D system metrics closer to the image metrics. While in several

cases image metrics were slightly more closely matched on a sum squared error basis, in reality these forcing methods generated structural anomalies, such as isolated high-surface-area domains alternating with low-surface-area domains. Therefore, after some investigation these methods were not used in the baseline SG model.

Torquato and coworkers have noted that relying solely on 2D metrics to generate 3D structures is problematic [60, 73]. Greater reconstruction accuracy likely requires 3D particle-boundary information to augment the single 2D cross sections used here. This could be in the form of experimental particle-size distributions [2] or the two-point cluster function $C_2(r)$ proposed by Torquato and coworkers [73, 74]. These options will be explored in future work once 3D structural information is obtained.

4.5 Ionic transport model calculations

Finite-difference model for periodic boundaries. Once representative 3D structures were generated from 2D image metrics, the ion transport properties of these structures were analyzed. The overall tortuosity was derived from the effective conductivity of the structure (Eq. 3.2), which in turn comes from imposing a driving force across the grid and calculating the resulting flux. For a finite or bounded system, one might think about placing the system between two parallel electrodes (i.e. isopotential surfaces) and imposing a potential difference. However, in combination with periodic boundaries, any such planar surfaces will cut through insulative domains (e.g. active material particles) causing varying portions of the electrodes to be obstructed. Because of local heterogeneities, the choice of where to place the surfaces would influence the calculated tortuosity. Therefore, we instead imposed a driving force that is consistent with the periodic boundary conditions used by the DPP and SG models and yields a single unambiguous value of tortuosity for each grid configuration and coordinate direction.

We place across the entire system volume a uniform external electric potential gradient $\nabla\phi^{\text{ext}}$ in one coordinate direction. The overall potential gradient at any point in the system is composed of this external field plus a local variation that averages to zero and must be computed. Put another way, the finite difference system is used to solve for local deviations from a linear potential profile, rather than for the full potential itself. Because this is a linear system, the resulting κ^{eff} is independent of the particular choice of magnitude $|\nabla\phi^{\text{ext}}|$. Our proposed method is similar to that employed to calculate transport properties in nonequilibrium periodic molecular simulations [75].

The finite-difference method was used to solve for the deviation potential distribution ϕ^{dev} on the 3D grid. The current flowing directly into node \mathbf{s}_I from lateral nearest neighbor node \mathbf{s}_J is

$$\mathcal{I}_{J \rightarrow I} = \delta \kappa_{ij} (\phi_J^{\text{dev}} - \phi_I^{\text{dev}} + \nabla\phi^{\text{ext}} \cdot \mathbf{s}_{IJ}), \quad (4.5)$$

where ϕ_I^{dev} and ϕ_J^{dev} are node potential deviations from a linear potential profile, and the quantity in parentheses expresses the total potential difference between the two nodes. The internodal position-difference vector \mathbf{s}_{IJ} is based on the “nearest image” of neighbor \mathbf{s}_J to node \mathbf{s}_I , in accord with periodic boundary conditions [68]. In particular,

$$\mathbf{s}_{IJ} = \mathbf{s}_J - \mathbf{s}_I - L \text{trunc} \left[\frac{2}{L} (\mathbf{s}_J - \mathbf{s}_I) \right], \quad (4.6)$$

where L is the edge length of the cubic system, and the function $\text{trunc}(\mathbf{x})$ independently truncates each element of \mathbf{x} , making it the next integer closer to zero. This means $|\mathbf{s}_{IJ}| = \delta$ even for neighbors that appear on opposite faces of the grid. Indices i and j indicate the domain identities of nodes \mathbf{s}_I and \mathbf{s}_J , respectively. Quantity $\kappa_{ij} = 2(\kappa_i^{-1} + \kappa_j^{-1})^{-1}$ is the pre-tabulated harmonic mean for the conductivities of domains i and j , reflecting the fact that current flow between adjoining nodes encounters a series resistance.

The finite-difference equation for the node potential at location \mathbf{s}_I is based on conservation of current, meaning that the sum of $\mathcal{I}_{J \rightarrow I}$ for all neighbors J to node I must be zero. This

leads to

$$\phi_I^{\text{dev}} = \frac{\sum_{\mathbf{s}_J} \kappa_{ij} (\phi_J^{\text{dev}} + \nabla \phi^{\text{ext}} \cdot \mathbf{s}_{IJ})}{\sum_{\mathbf{s}_J} \kappa_{ij}}, \quad (4.7)$$

where the sums are over the 6 lateral nearest neighbors (nodes \mathbf{s}_J) surrounding node \mathbf{s}_I . Nodes where $\kappa_i = 0$ give trivial solutions and were not included in the system of linear equations. Successive overrelaxation was used to solve for a converged vector of ϕ_I^{dev} values, starting from an initial guess of a zero vector.

The total flow of current \mathcal{I}^{tot} is evaluated across an arbitrary plane perpendicular to vector $\nabla \phi^{\text{ext}}$ by summing contributions given by Eq. 4.5 for each pair of neighbors on opposite sides of the plane. The choice of plane location will not change the value of \mathcal{I}^{tot} as current is conserved. The matrix effective conductivity is then

$$\kappa^{\text{eff}} = \frac{\mathcal{I}^{\text{tot}}}{L^2 |\nabla \phi^{\text{ext}}|}. \quad (4.8)$$

The virtual conductivity experiment was performed independently for all three coordinate directions of a given configuration. The three effective conductivities were compared to each other to ensure that a convergent isotropic structure had been generated—As long as system size was sufficient to incorporate several active material particles (as shown in Fig. 4.3) agreement was satisfactorily within a few percent. If accurate tortuosity is needed at lower resolutions the solution is to improve sampling through increased system size or number of tested configurations.

Tortuosity of predicted structures. Fig. 4.3 shows how the baseline SG model’s predicted tortuosity depended on the resolution, i.e. how much coarse graining of the basis image was done prior to the simulation. Each point in the figure is from the final configuration of a cubic simulation with 220 nodes per edge, meaning each point required similar computational effort. Even though they have the same number of nodes, the four images of the SG model reconstruction in Fig 4.4a-e exhibit widely different length scales due to different node resolutions. In Fig. 4.4a the simulation box has edge length of $14.3 \mu\text{m}$, meaning only a few

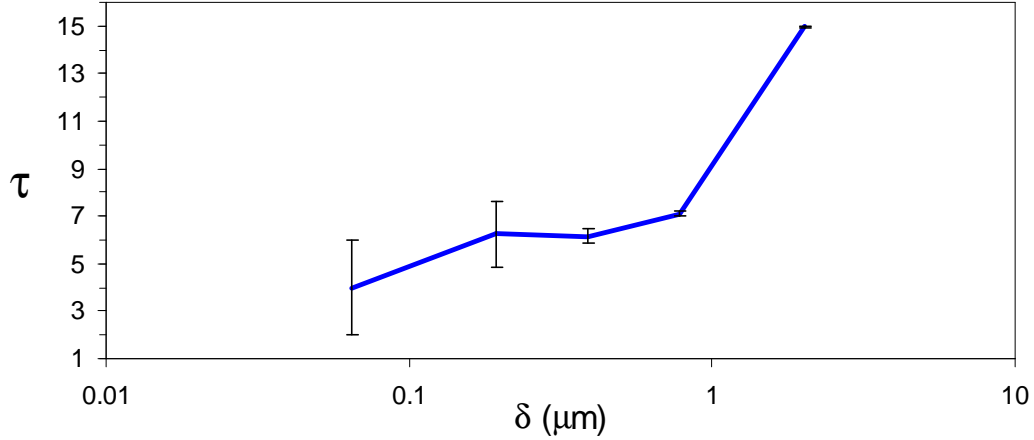


Figure 4.3: SG model tortuosity versus node resolution for 34% porosity electrode. Error bars are standard deviations of the mean, based on one sample in each coordinate direction. The line connecting points is a guide to the eye.

active particles may be included; for Fig. 4.4e the simulation box has edge length $443 \mu\text{m}$, much larger than for the original basis image. At smaller length scales the uncertainty in tortuosity is large because so few pores are included in the final configurations. Nevertheless, the tortuosity was remarkably consistent, given intrinsic uncertainties, for the SG model at lower resolutions. At node resolutions above around $0.8 \mu\text{m}$, computed tortuosity began to diverge, an artifact from having nodes representing too large a length compared to pore sizes. This means that there is a “sweet spot” where the model resolution is a compromise between minimizing random error and systematic bias. In the results that follow, a node resolution around $0.4 \mu\text{m}$ was used (the middle point in Fig. 4.3). The resulting simulated volumes were cubes with edge length $88 \mu\text{m}$, on the same order of film thicknesses as used in commercial electrodes.

Fig. 4.5 compares predicted tortuosity for the DPP and SG models to experimental values for the electrodes used in this work. The Bruggeman curve was developed in our prior work from experiments on different types of cathode films, and is shown for comparison

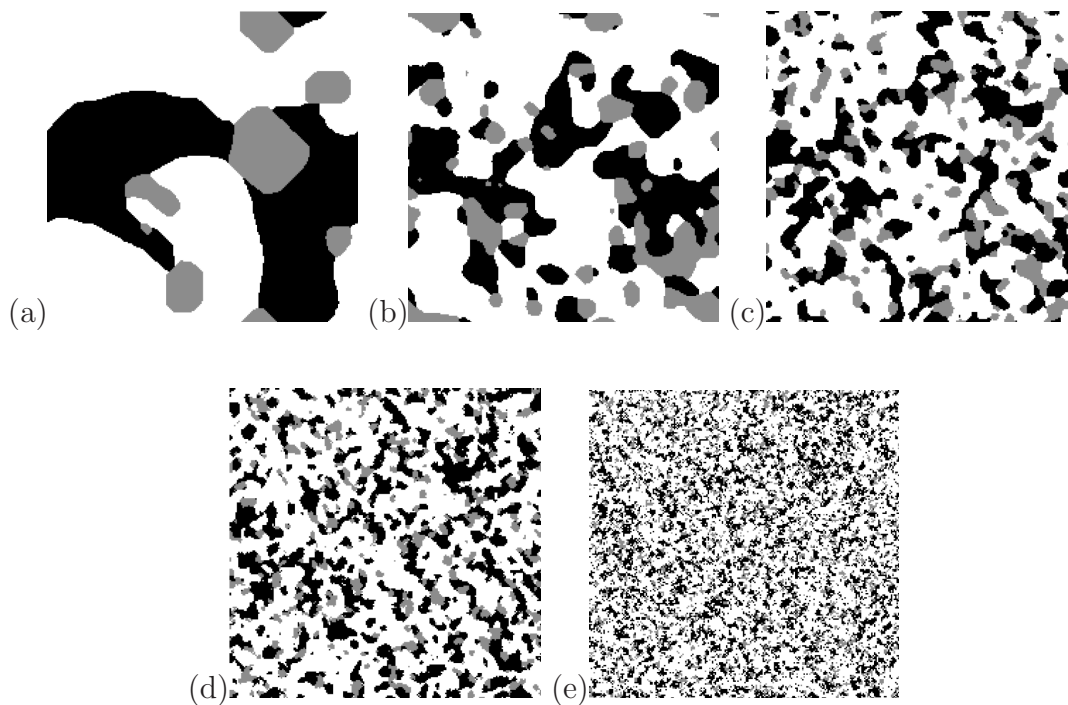


Figure 4.4: SG model reconstruction using non coarse-grained statistics for different node resolutions (δ) and the box lengths (L) as follows: (a) $\delta = 0.065\mu\text{m}$ and $L = 14.3\mu\text{m}$; (b) $\delta = 0.195\mu\text{m}$ and $L = 42.9\mu\text{m}$; (c) $\delta = 0.39\mu\text{m}$ and $L = 85.8\mu\text{m}$; (d) $\delta = 0.78\mu\text{m}$ and $L = 171.6\mu\text{m}$; (e) $\delta = 2.01\mu\text{m}$ and $L = 443.3\mu\text{m}$.

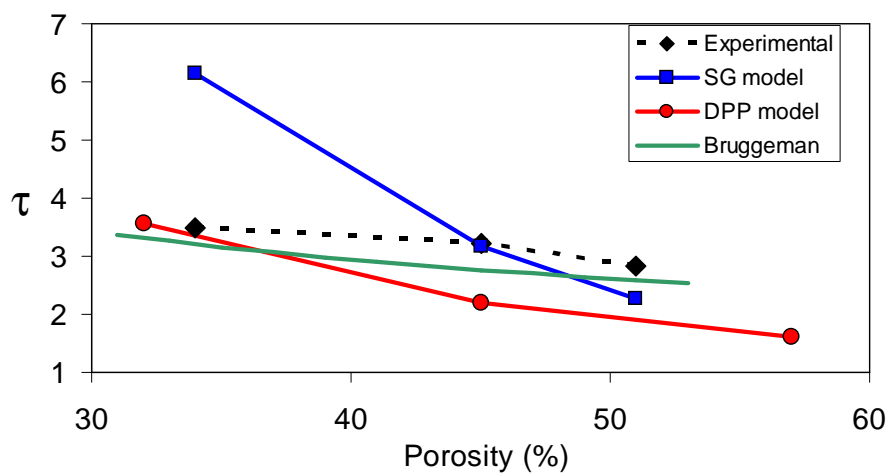


Figure 4.5: Simulated and experimental electrode tortuosity versus porosity. Lines are a guide to the eye, except for the Bruggeman curve, which corresponds to a best-fit correlation of prior experiments.

Table 4.1: Cathode tortuosity predictions for 34% overall porosity. The ionic conductivity of the carbon domains κ_C is adjusted relative to intrinsic electrolyte conductivity κ .

Conductivity κ_C	Tortuosity τ		
	Experimental	SG model	DPP model
κ		2.70	1.6
0.05κ	3.5	6.15	3.6
0		8.46	4.1

[7]. Due to the sub-micron carbon and binder materials forming micron-sized agglomerates we decided to treat the carbon/binder agglomerates as a pseudo-homogeneous domain with a lower electrolyte conductivity. For Fig. 4.5 we assumed the carbon domains exhibited effective ionic conductivity of 5% of intrinsic electrolyte conductivity. The resulting SG model tortuosity is close to correct at intermediate porosities when compared to experiment, but its slope with respect to porosity is too high. The DPP model underpredicts tortuosity. Nevertheless, both models produced semi-quantitative results with the correct trend. This is remarkable considering both models are extrapolated from single FIB/SEM cross sections.

The SG and DPP models can be used to give some idea of how the carbon domains restrict ionic transport. With the predicted microstructures in hand, we can vary the relative conductivity of the carbon domains to assess what effect this has on overall ionic transport through the electrode. Table 4.1 shows that the effect is significant. Results were obtained by varying carbon conductivity (κ_C) while holding the active material ionic conductivity at zero and holding the pore conductivity at the intrinsic electrolyte conductivity κ . For instance, if the carbon domains are virtually removed (equivalent to setting their conductivity to κ) the overall tortuosity of the cathode is less than half of the baseline value, according to both

the SG and DPP models. On the other hand, if the carbon domains completely obstruct ion transport, the overall tortuosity is only modestly greater.

These reconstruction results show how important carbon domain ionic conductivity is to the overall ionic conductivity. In fact, electrode ionic resistance is more strongly tied to the volume fraction and conductivity of the carbon domains than it is to the overall porosity, which is shown in more detail in Chapter 5. One result of improving the ionic pathways in the carbon domains would be the ability to add more carbon to a cathode without increasing overall ionic resistances. More carbon can reduce electronic resistances [2], which will enhance high-rate cell performance.

4.6 Conclusions

The cross sections of SEM images revealed the existence of discrete porous carbon domains in the cathode microstructure. Transport experiments and modeling indicated that these carbon domains are highly tortuous and restrict to a large degree the overall ion transport in the cathode. This suggests that adding additional carbon and binder to an electrode in an attempt to improve electronic conductivity may severely restrict ionic transport and hence overall cell performance. There is therefore an optimal amount of carbon and binder for any given electrode. We expect this principle holds true for a wide range of cathode and anode active materials being considered for Li-ion battery use, as nearly all require the supplemental carbon and binder additives.

Two types of 3D models for correlating and predicting the electrode microstructure were explored. The first, known as the dynamic particle packing (DPP) model, is based on aggregates of spheres that move collectively in response to interparticle forces. The second is a stochastic grid (SG) model closely related to Monte Carlo techniques used in statistical physics to study cooperative and competitive phase behavior. The two models imitate

the sub-micrometer-scale arrangement of active material particles, carbon, binder, and pores. The models use a small set of fundamental interdomain and bulk interaction parameters that were parametrized from 2D FIB/SEM cross sections, rather than from a full 3D reconstruction. The SG model is easier to implement and more closely imitates the structural features of the 2D FIB/SEM cross sections, though it suffered from excessive aggregation of active material particles. Both models were able to semi-quantitatively reproduce experimental tortuosity measurements of cathodes at different porosity values.

The SG model may be used for a more in-depth analysis of electronic transport. The model also may be used in predictive mode in which the trade-offs between ionic and electronic resistances can be evaluated under different material fractions. Trade-offs between ionic and electronic resistances are described in Chapter 5.

Chapter 5

Trade-offs between ionic and electronic resistances

5.1 Introduction

Most commercialized lithium-ion cells at this time rely upon cathode reacting materials (i.e. active materials) that have low electronic conductivity [76]. For example the conductivity of LiCoO_2 pellets is around $10^{-4} \text{ S cm}^{-1}$ while the aluminum current collector conductivity is $3.4 \cdot 10^5 \text{ S cm}^{-1}$ [76]. The low conductivity of these cathode active materials has been identified as causing the major electronic resistance within cathodes, thereby limiting power capabilities [2].

In order to mitigate the resistance of cathode reacting materials, high-conductivity materials such as carbon black and graphite are added to electrodes. Conductive additives and reactive materials are bound together using a polymeric binder such as polyvinylidene fluoride (PVDF).

In prior chapters we showed how to use focused ion beam (FIB) and scanning electron microscopy (SEM) in order to image sections of commercially made porous electrodes. Imaged cross sections of electrodes revealed the existence of discrete porous carbon domains in the microstructure, as shown in Figure 5.1. The resulting images were also processed to measure

microstructural properties including domain volume fractions and interfacial areas. Additional experimentation and modeling indicated that the carbon domains are highly ionically tortuous and restrict to a large degree the overall ion transport in the cathode. This result explains how the addition of carbon and binder to an electrode in an attempt to improve electronic conductivity may severely restrict ionic transport and hence decrease overall cell performance.

In Chapter 4 we introduced two models that can reconstruct porous electrode 3D structure. One method, the stochastic grid (SG) model, is closely related to Monte Carlo techniques used in statistical physics to study cooperative and competitive phase behavior. The SG model imitates the sub-micrometer-scale arrangement of active material particles, carbon, binder, and pores. Imaged carbon domains, which are composed of carbon, binder, and micropores, are treated as a homogeneous phase in the SG model. Treating the complicated microstructure as though it is composed of 3 homogeneous phases allows the SG model to create a 3D reconstruction from a small set of fundamental interdomain and bulk interaction metrics that were found from imaged 2D FIB/SEM cross sections.

One of the things we learned from the SEM/FIB electrode image, as seen in Figures 4.2 and 5.1, is how the carbon creates distinct agglomerates. The SG model can provide a 3D view of how these carbon agglomerates relate to each other. Figure 5.2 shows a 3D reconstruction of the cathode in which the active material and pore structures were made transparent. It can be seen that the carbon domains form very distinct agglomerates in 3D space that are distinctly below the electronic percolation limit. Using the SG model structure reconstructions, we can quantify how electronic conductivity depends on carbon domain agglomerates as well as on the active material conductivity.

In this chapter we look at how the following factors affect both electronic and ionic conductivity: porosity, carbon domain fraction, and binder fraction. To do this we used the observed changes in structural metrics seen in the FIB/SEM images as input for the

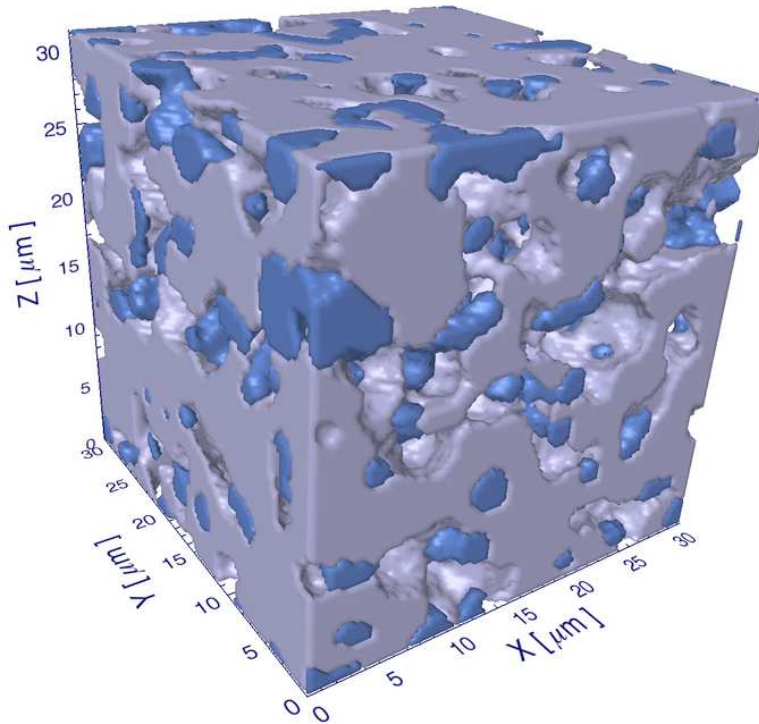


Figure 5.1: $30\ \mu\text{m}$ cube of 34% porosity electrode reconstructed from a FIB/SEM image. The active material is grey and the pores are transparent while the carbon domains are a darker shade of blue.

SG model. Furthermore, these input parameters are correlated into functional forms that allow the SG model to be run in predictive mode. This methodology provides us a way to predict and explore the effects that different electrode structures have on electronic and ionic resistances.

While it has been understood that changes in electrode structure (such as calendaring) can change cell performance, the mechanisms for this have only been understood qualitatively [2]. Our reparametrized SG model allows us to predict 3D structures with various electrode compositions and structures of porous electrodes. We show how the SG model can be

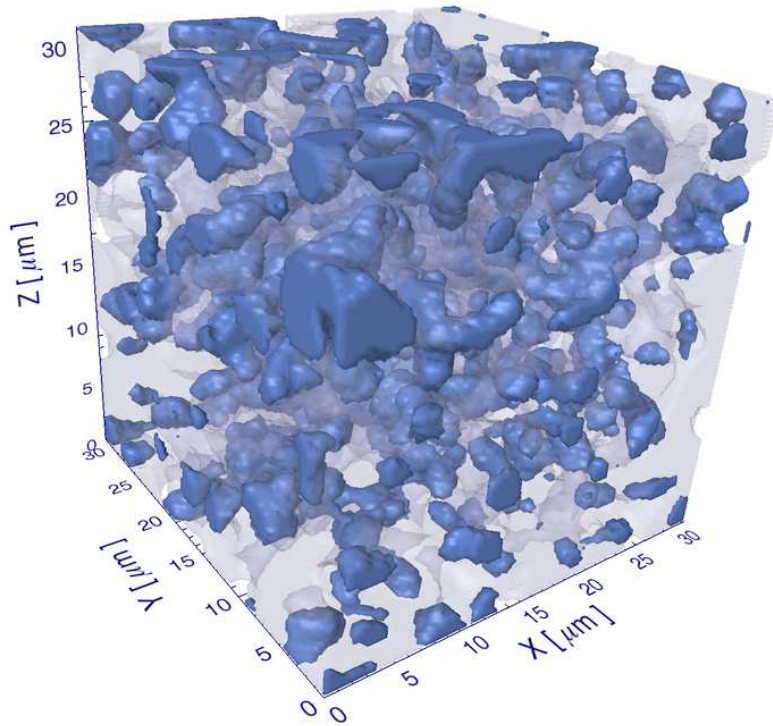


Figure 5.2: 30 μm cube of 34% porosity electrode reconstructed from a FIB/SEM image. The active material is semitransparent and the pores are transparent while the carbon domains are visible.

used to predict semi-quantitatively electronic and ionic resistances under varying fabrication parameters.

5.2 Electronic conductivity of LiCoO_2

The focus of this work is on lithium cobalt oxide, which has been the longest commercialized lithium-ion active material. Electronic conductivity measurements have been made of both pelletized LiCoO_2 as well as single crystals [31, 77, 78]. Pellet conductivity was measured at 0.00113 S/cm [31], which was measured by compressing LiCoO_2 particles together without a

binder additive. Single crystal conductivity has been measured at much higher conductivities of 0.2 S/cm for the fully discharged LiCoO_2 [77, 78] and 500 S/cm for fully charged $\text{Li}_{0.5}\text{CoO}_2$ [77]. Also, it has been reported that $\text{Li}_{1-x}\text{CoO}_2$ shows almost a temperature-independent conductivity between 1 and 100 S/cm, while fully lithinated LiCoO_2 has a semiconductor-like conductivity 0.001 S/cm at room temperature [79].

In addition, it has been found that LiCoO_2 exhibits p-type semiconducting behavior where either an excess of lithium from a fully discharged state or a deficiency of lithium causes holes, which increase conductivity as reported by several groups [78, 80, 81]. They also found that the addition of divalent doping agents like Mg^{2+} caused dramatic enhancements in conductivity of fully lithinated LiCoO_2 due to Mg^{2+} leading to the formation of lower valence ions Co^{4+} from Co^{3+} , which raises conductivity. Very little Mg^{2+} needs to be added as a dopant to increase electronic conductivity. At much higher concentrations of Mg^{2+} or other 2+ ions, conductivity of LiCoO_2 compounds is decreased significantly [76].

LiCoO_2 is a two-phase material, which means that during discharge, the exterior of LiCoO_2 particles is in the discharged state [79, 82, 83]. This means that the exterior of the LiCoO_2 particles becomes lithium rich while the center is at the initial concentration of lithium. Two-phase materials have been modeled using a shrinking core model [84] as illustrated in Figure 5.3.

Having a two-phase material like LiCoO_2 means that electronic conductivity of the exterior of LiCoO_2 particles during discharge is at its lowest value due to the exterior being fully saturated by lithium. Because electrical charge tends to travel on the exterior of particles, a change in a particle's exterior conductivity will have a large effect on interparticle resistances. Thus, overall electronic conductivity may be significantly different during discharge then during charge. Experimentally, significantly more electrode overpotential has been observed for LiCoO_2 during discharge conditions than on charge conditions [85]. White and coworkers observed this increase in overpotential during discharge and modeled it with an

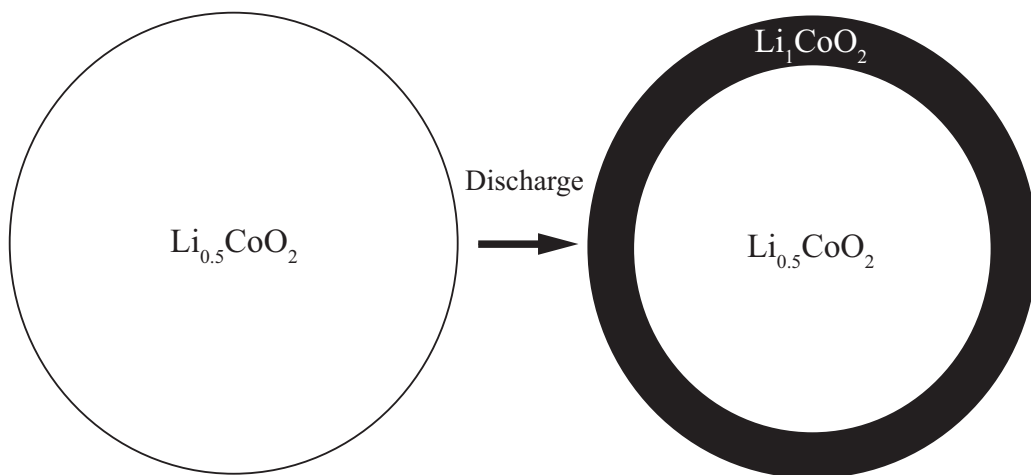


Figure 5.3: Illustration of the discharge of a two-phase material, namely LiCoO_2 . During discharge there is an outer shell of the lithium-rich phase and an inner core of lithium-poor phase.

empirical change to anodic versus cathodic surface reaction kinetics [85]. While a chemical reaction rationale may explain discharge behavior, it is more likely that the concentration-dependent conductivity of LiCoO_2 is the key mechanism controlling electronic behavior of electrodes at high rates of discharge or charge.

From reconstructed electrode structures, we can predict the effect that active material conductivity has on overall electrode conductivity. Full electrochemical models can be used to better determine the effects that concentration has on electrode performance by determining the role electronic conductivity of the electrode has on its performance.

5.3 Interparticle connections

In prior theoretical work, we proposed that electronic connectivity of particles is related to the area of interparticle interactions [2]. From the FIB images of commercially made Saft cells, as shown in Chapter 4, we were able to determine the relative areas of the interfacial interactions. This was done, for instance, by analyzing Figure 3.6 and determining the ratio

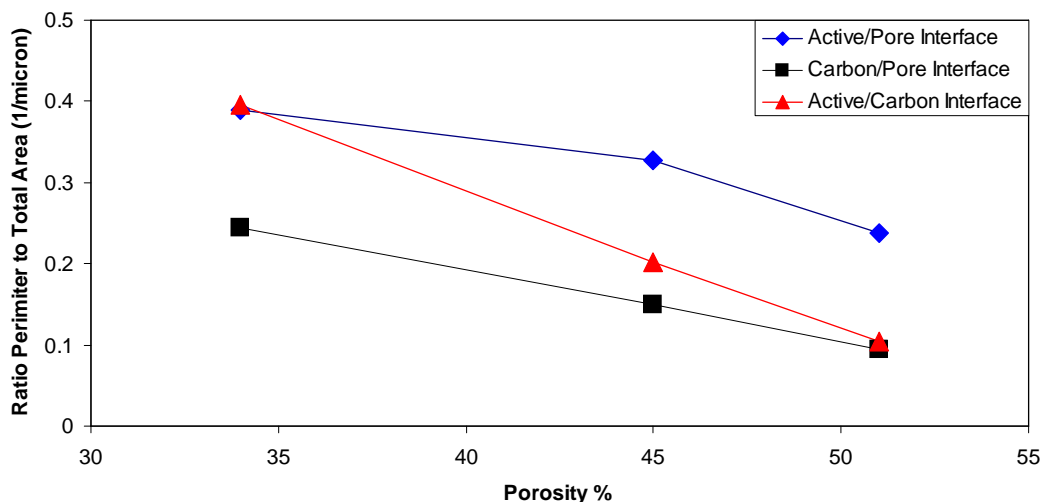


Figure 5.4: Interdomain contact areas per unit volume versus porosity with image pixel resolution of $0.195 \mu\text{m}$.

of the inter-domain contact perimeter to total area of the electrode image. Figure 5.4 is a graph of these statistics versus electrode porosity. In a 3D system (instead of the 2D image) the important perimeter to determine is the ratio of interdomain surface area to the volume of the electrode. Perimeter/area ratios are proportional but not equal to the surface/volume ratios which are used in electrochemical battery models [2, 4]. This means the relative values reported in Figure 5.4 can give us an idea of how the surface/volume ratio changes with porosity.

It can be seen in Figure 5.4 that the active/carbon domain interfacial area decreases with porosity significantly greater than the other interfacial areas. That active-to-carbon domain interactions increase with decreasing porosity has been postulated by us before [2], but the FIB images provide some quantification of this concept.

Prior work using spherical approximations suggested that interfacial areas are related geometrically to particle size [2]. Work done by Sheu and coworkers experimentally shows a decrease in electrode resistances with smaller particle size [86]. Sheu also found that cycle life

was adversely affected by larger particle sizes, which may suggest accessible interfacial areas are decreasing with cycling for the LiCoO₂ system. Further FIB or tomographic work should be able to experimentally determine how interfacial areas and hence impedances change with cycling.

5.4 SG model electronic predictions

As discussed in Chapter 4, representative 3D structures were generated from 2D image metrics. The ionic conductivity of these structures was determined by solving the conservation-of-charge equation for the potential distribution. The same method is used in this chapter to determine the electronic conductivity of the structures, except that electronic conductivities replace ionic conductivities. To do this, the conductivity of the different domains and of the overall structure are normalized by the carbon domain conductivity. Thus, the electronic conductivity (σ) of the pore domain was set at zero, and the normalized conductivity of carbon domains was set at one. The conductivity of active domains was then varied to assess its effect on overall electrode conductivity. The calculated overall effective conductivity (the analogue of Equation 4.8) becomes

$$\frac{\sigma^{\text{eff}}}{\sigma_{\text{C}}} = \frac{\mathcal{I}^{\text{tot}}}{L^2 |\nabla \phi^{\text{ext}}|}, \quad (5.1)$$

where σ_{C} is the conductivity of the carbon domain, \mathcal{I}^{tot} is the total flow of current, L is the length of the system, and $\nabla \phi^{\text{ext}}$ is the uniform external electric potential gradient we imposed upon the system. Instead of determining a geometric factor like tortuosity, the normalized effective conductivity of the structure was determined.

We analyzed both how electronic resistances may change with porosity as well as with electrode composition. Figure 5.5 shows how both the electronic and ionic transport changes with porosity, along with numerical confidence of each point. Each point comes from a

simulated configuration with 220 nodes per side and transport resistances found for different directions. Both the ionic and electronic transport resistances presented here come from the same set of structural configurations. Ionic transport is presented as $1/\tau$ so that it represents a non-dimensional ionic conductivity. The electronic transport is normalized to $\sigma_{\text{eff}}/\sigma_C$ at an σ_A/σ_C value of 0.05 as an example case. The σ_A/σ_C value of 0.05 is a reasonable estimate based on our experiments and the measured intrinsic conductivities as will be described in greater detail in Chapter 6. By graphing the non-dimensional values of ionic and electronic conductivities, it is possible to see the relative change in transport with changing porosity. Error bars shown in this chapter come from the standard deviation of the mean of the independent solutions in each coordinate direction of a given structural configuration.

In Figure 5.5 we see that both the electronic and ionic transport follow expected resistance trends with porosity. For example as porosity is increased, the ionic pathways improve, lowering the inverse tortuosity. For the electronic resistances the effective conductivity increases as porosity decreases.

Both the ionic and electronic resistances change significantly but not greatly with porosity. Experimental results show that electrode performance does change with porosity [2], which suggests that one or both types of resistances are significant. In order to determine the true trade-off of these effective resistances on electrode performance, a full electrochemical model is necessary.

The magnitude of electronic conductivity changes with different ratios of σ_A/σ_C as shown in Fig 5.6 at different porosities. The difference in overall conductivity at different porosities increases as the ratio of σ_A/σ_C increases. This means that as active material conductivity is increased, porosity changes have a larger effect on electronic resistances. It can also easily be seen that the effect of the active material conductivity on overall conductivity is much larger than that for porosity changes.

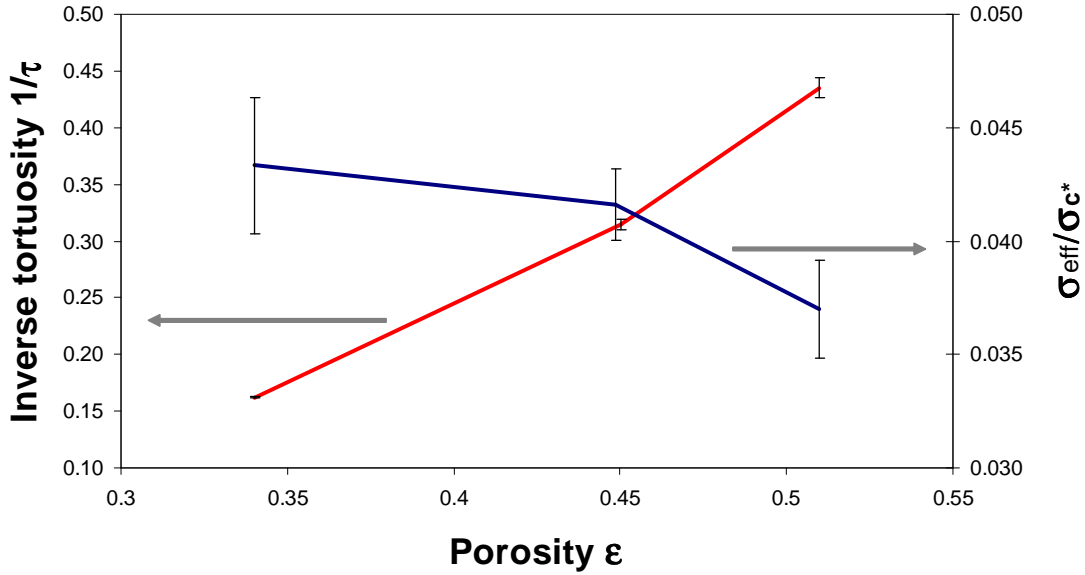


Figure 5.5: Model prediction of dimensionless conductivities versus porosity at an σ_A/σ_C value of 0.05. Both middle values are at 45% porosity but were offset so that the error bars wouldn't overlap. Resolution was $\delta = 0.39 \mu\text{m}$.

One hypothesis on electrode discharge resistances is if electronic resistances dominate then a reaction front will occur in which areas closest to the current collector react before areas closer to the separators. This reaction front would be heightened by the concentration-dependent conductivity of LiCoO_2 , which during discharge would further lower the conductivity of the electrode at areas close to the current collector. This would increase transport losses for later reactions when the easily accessible materials have reacted. At higher rates, both the reaction front and concentration-dependent conductivity will have larger effects, because the average concentration of lithium in the solid phase close to the current collector would be higher at higher rates. In other words, the higher the rate of discharge/charge, the larger the concentration gradients. These results may show in a theoretical way why material development has led commercialized LiFePO_4 to have carbon coatings, which effectively

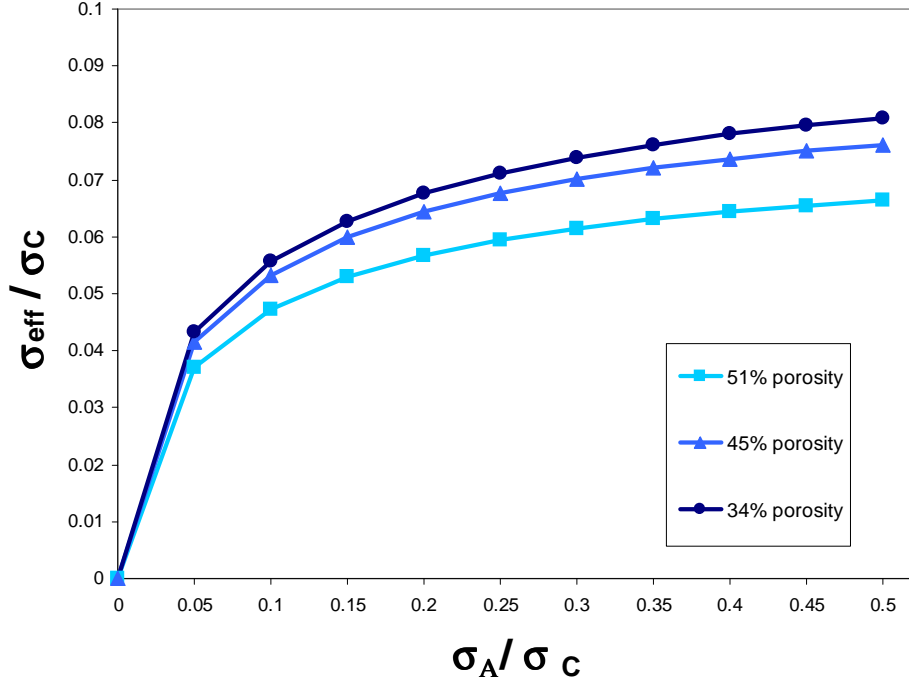


Figure 5.6: Electronic results of the SG model at different porosities and different ratios of σ_A/σ_C . SG model was run at 220 nodes cubed. The standard deviations of the mean for each point are nearly uniform at around 5% of dimensionless conductivity. Resolution was $\delta = 0.39 \mu\text{m}$.

increase the σ_A/σ_C ratio by increasing the conductivity of the active material domain and decreasing concentration conductivity effects.

5.5 SG predictive model

In the prior section, we illustrated the trade-offs in electronic and ionic resistances with porosity. In that case, the SG model parameters were obtained directly from FIB/SEM images. This section deals with how ionic and electronic resistances may be changing with material fractions. To look at how resistances depend on material fractions we had to determine how to modify the SG model so that it might accurately predict structures at

different material compositions, even though this wasn't thought of as a possible use of FIB/SEM image data.

Because there isn't a direct physical basis for the interdomain and intradomain contact probabilities, we found an empirical correlation that could be made between these probabilities and the volume fractions of domains. In order to find an empirical correlation, we plotted the radial distribution function versus the volume fractions until we found linear relationships. We found that the correlation presented here had the lowest standard deviation and was the best fit. The method described here may also work for other porous media interdomain and intradomain contact probabilities.

5.5.1 Parametrizing the SG predictive model

The SG model as previously outlined (Chapter 4) works off of MC moves evaluated through the normalized lateral and diagonal neighbor probabilities (P_{ij}). These probabilities correspond to the first two points of the radial distribution function:

$$g_{ij}(r) = \frac{P_{ij}(r)}{\varepsilon_i \varepsilon_j}, \quad (5.2)$$

where ε is the volume fraction of a particular phase, r is the internodal distance, and g is the radial distribution. The empirical correlation that we found for relating how this radial distribution function changed for different volume fractions of pore, active, and carbon domains is:

$$g_{ij}(r) = \begin{cases} \chi_{ii}\varepsilon_i & \text{for } i = j \\ \chi_{ij}\varepsilon_i\varepsilon_j & \text{for } i \neq j \end{cases} \quad (5.3)$$

where i and j represent domains, and each χ_{ij} is a constant for each independent type of domain contact. It is important to note that for intradomain interactions (AA, CC, and PP), a constant could only be found when dividing by the volume fraction of the domain phase, and for interdomain interactions (AC, AP, and CP), the most accurate form came

Table 5.1: Inter and intra domain constants determined from Equation 5.3. The \pm values are the standard deviation of the mean from three SEM/FIB images at different porosities.

Interaction ij	lateral χ_{ij}	diagonal χ_{ij}
AA	0.925 ± 0.002	0.900 ± 0.003
PP	0.891 ± 0.025	0.854 ± 0.033
CC	0.864 ± 0.012	0.817 ± 0.015
AC	0.00903 ± 0.001230	0.01222 ± 0.00184
AP	0.02904 ± 0.002700	0.03901 ± 0.00346
CP	0.00703 ± 0.00027	0.00951 ± 0.00031

from probabilities being divided by both domain volume fractions. Table 5.1 shows the constants determined by averaging the χ_{ij} constants from the three FIB/SEM images used for parametrization. That this empirical model achieves such a good fit is surprising to us but allows for the possibility of predicting radial distribution functions for different material volume fractions. In order to generate 3D structures at different volume fractions than those obtained from the image, we only need to multiply these constants by the desired volume fractions of the electrode we wish to simulate to obtain the needed model domain contact probabilities.

To validate the generated structures from the predicted inter- and intra-domain probabilities, we compared the electronic and ionic resistances of predicted electrode structures to electrode structures generated directly from images. This validation step does not show whether the SG model is more or less accurate, just whether the predict code agrees with the original code. Figure 5.7 shows the results of the Predict SG model (PSG model) versus the direct-from-image SG model results at different porosities. As can be seen, the two models show the same trends, except the PSG model generally predicts a slightly higher overall

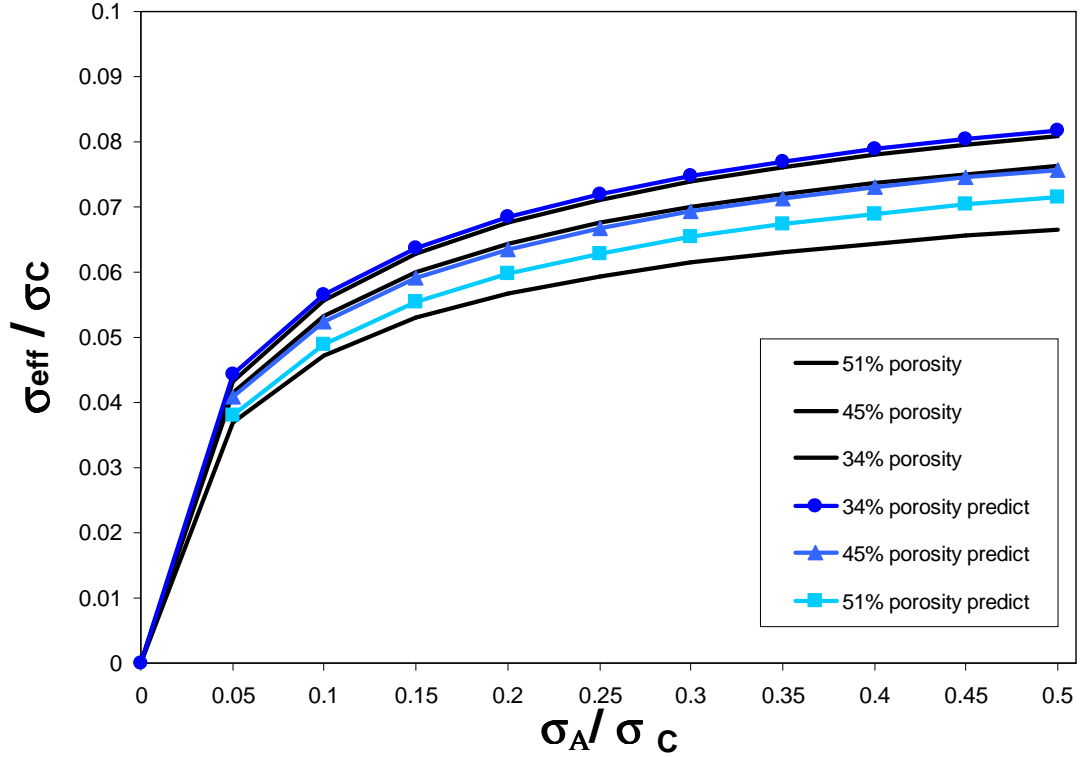


Figure 5.7: Electronic validation of the Predict SG model versus the baseline SG model. Predict SG model results are in different colors and have different symbols. The baseline results are the same as those shown in Figure 5.6. The standard deviation of the mean of the predict SG model was around 4% of dimensionless conductivity. Resolution was $\delta = 0.39\mu\text{m}$ for all model results.

electronic resistance. Figure 5.8 shows 2D slices of the structures generated at different porosities by the PSG model, which can be compared to the FIB images (Figure 3.6) as well as the SG reconstruction using image statistics as seen in Figure 5.8. It is important to note how similar the predict structures are to the regular SG reconstruction. Further validation comes from comparing the ionic resistances of the PSG model and baseline SG model, as seen in Figure 5.9. Ionically both the PSG model and the baseline SG model agree very well.

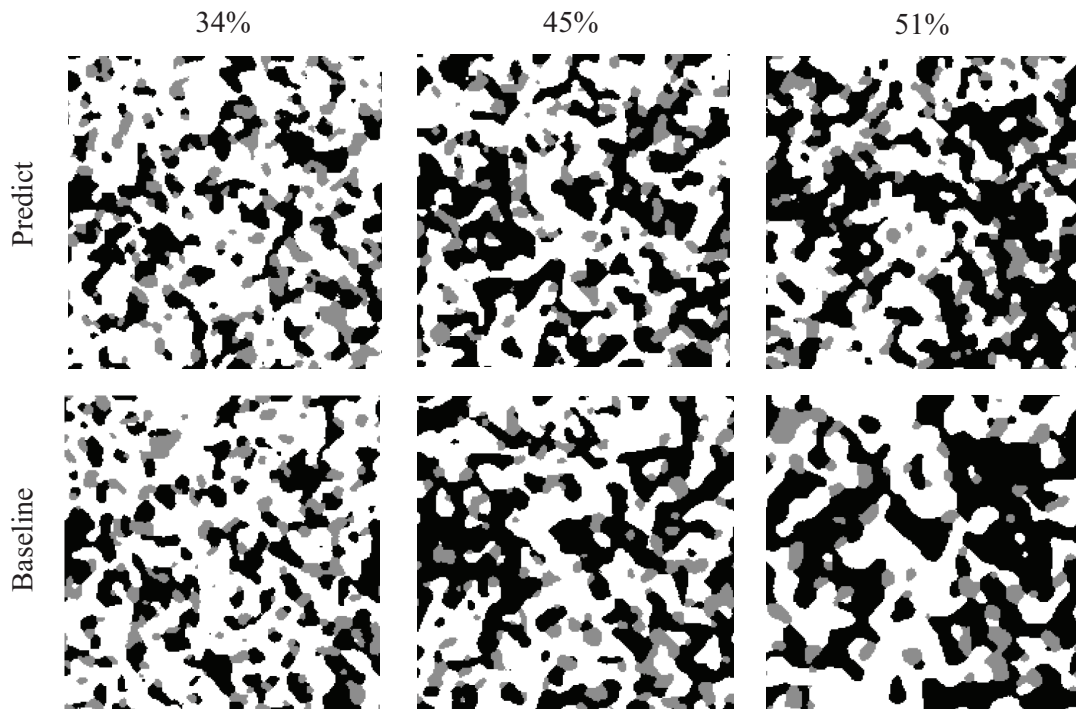


Figure 5.8: Predict and baseline SG model reconstruction at porosities of 34%, 45%, and 51%. Resolution was $\delta = 0.39\mu\text{m}$ for all model results.

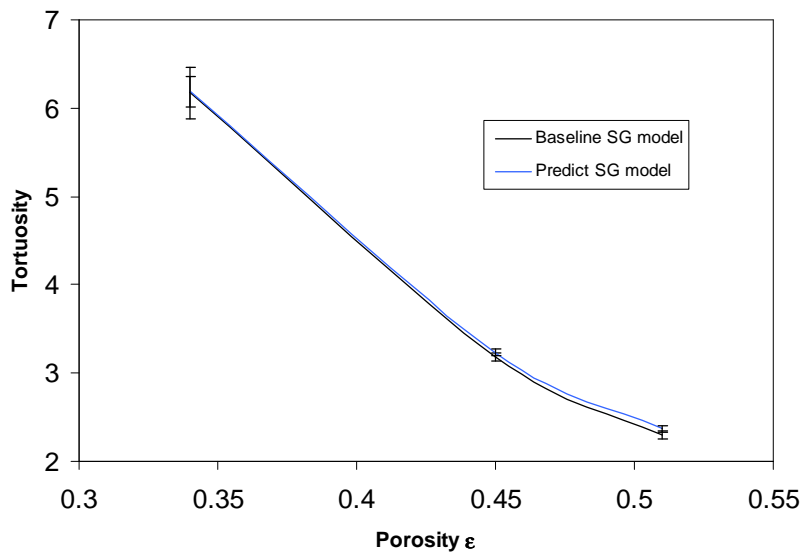


Figure 5.9: Comparisons of PSG model and baseline SG model's ionic tortuosity with varying porosity.

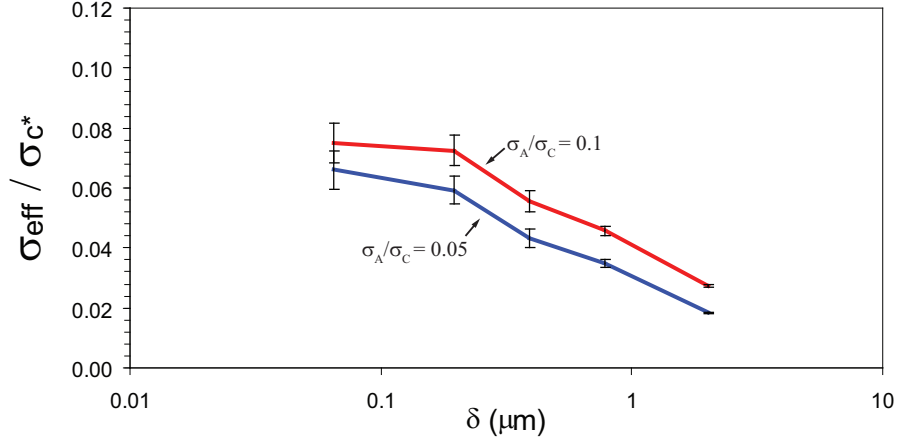


Figure 5.10: Overall dimensionless conductivity versus node size for two different active material conductivities. Error bars are standard deviations of the mean, based on one sample in each coordinate direction. The lines connecting points are a guide to the eye.

5.5.2 Electronic transport results with different resolutions

We studied how the PSG model’s electronic results changed with node size. Similar analysis was done for ionic pathways previously as shown in Figure 4.3 for the structural configurations shown in Figure 4.4. Figure 5.10 shows how resolution affects overall dimensionless conductivity at different ratios of σ_A / σ_C . We see that even at different σ_A / σ_C ratios, the trend of lowering overall dimensionless conductivity with resolution holds true. Similarly, as resolution decreases, the amount of numerical uncertainty increases. Due to ionic results being the best at $0.39 \mu\text{m}$, we wanted to also obtain the electronic results from the same configurations. While the electronic results do not have a plateau in which the electronic results are not dependent on node size, a resolution of $0.4 \mu\text{m}$ is close to the lower resolution results and benefits from faster computational time.

5.5.3 Determining the importance of carbon on overall conductivity

Many battery materials (such as LiFePO_4) have even lower intrinsic conductivities than LiCoO_2 . It has been shown that as active material conductivity decreases, overall electrode performance degrades. As a result, these lower conductivity materials have had to rely on higher volume fractions of carbon. Using the PSG model, it is possible to quantify how changes in active material conductivity will necessitate the varying of the carbon volume fractions and the effects this will have on ionic pathways. Figure 5.11 shows the PSG model results and how electronic and ionic dimensionless conductivities change with carbon domain fractions. As can be seen both ionic and electronic dimensionless conductivities vary widely over different carbon domain fractions.

The effect that the active material conductivity has on overall conductivity can be quantified using the model results. If we define baseline conductivity of the active material as a σ_A/σ_C ratio of 0.05, then a very low active material conductivity will be represented by a σ_A/σ_C ratio of 0. Changing the σ_A/σ_C can dramatically affect the overall conductivity as seen in Figure 5.11.

If we wished to manufacture electrodes with a very low active material conductivity and still have overall electrode conductivity be the same as electrodes made with baseline active material conductivity, more carbon would need to be added. The amount of extra carbon varies based on the porosity of the electrode, but let us use the 34% porosity as an example. Looking at Figure 5.11 we see that for very low active material conductivities, the overall conductivity is severely limited until around 20% carbon domain volume fraction. A 25% carbon domain is required in order to achieve the same overall conductivity for a low conductivity active material as the baseline active material has with just 11% carbon domain. However, a 25% carbon domain electrode has approximately double the ionic resistance. This

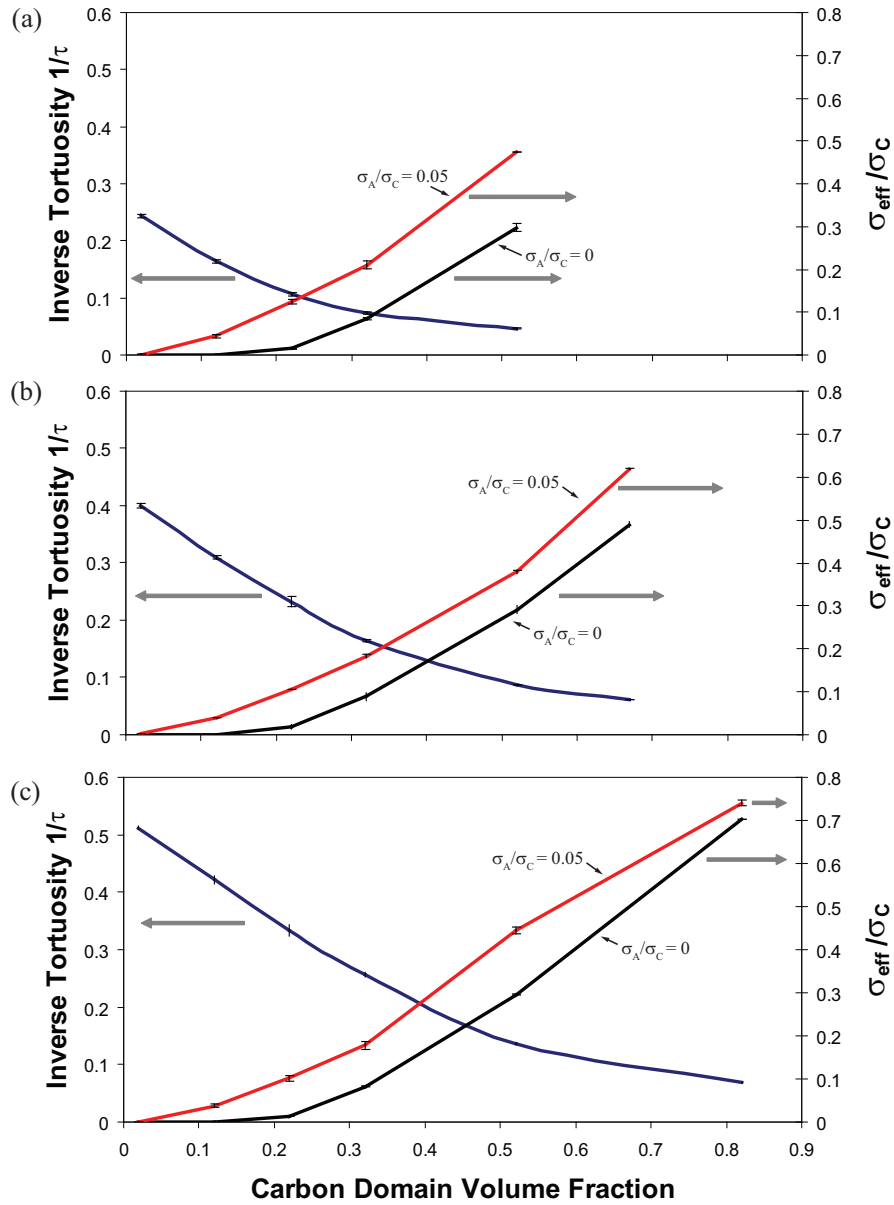


Figure 5.11: Electronic (red and black) and ionic (blue) dimensionless conductivity changes with carbon fractions at porosities of: (a) 34% (b) 45% (c) 51%. Electronic results are presented at two σ_A/σ_C ratios: 0.05 and 0.

example shows that by increasing the active domain conductivity, one reduces the need for high carbon contents, which in turn decreases ionic losses.

An example of increasing the active material domain's conductivity is the LiFePO_4 battery material system where commercialized manufacturing processes create the nano sized LiFePO_4 particles with carbon coatings. The carbon coatings effectively increase the conductivity of clumps of LiFePO_4 thereby increasing the conductivity of the active material domain. This changes the LiFePO_4 active material domains from very low conductivity to more of a baseline conductivity or even better.

To understand why so much more carbon domain is needed to achieve overall conductivity for very low conductivity active material electrodes, a brief discussion of percolation theory should be made. Percolation theory basically states that there is a critical volume fraction of conductive material needed in order for there to be a continuous pathway across the system. Figure 5.11 shows that if the carbon domain is the only conductive material, the percolation limit is at around 20% carbon domain fraction. If the active material is even slightly conductive, it greatly decreases the overall percolation limit because of the active material domain representing such a large overall volume fraction.

An electrode can be thought of from an electronic standpoint as a two-component system. There are two different electronic conduction regimes that can form. Figure 5.12 illustrates with resistive circuits two different regimes. The first electronic circuit happens if the carbon domain has a high enough volume to be above its percolation threshold as shown in Figure 5.12(a). If the carbon domain is above its percolation threshold, then the carbon domain conductivity generally determines overall electrode conductivity.

The second electronic circuit occurs when the carbon domains are below their percolation threshold as shown in Figure 5.12(b). This second electric circuit can be further divided into the case of high and low active material conductivity. In the case of the active material having a high enough conductivity to provide electronic percolation then current can flow.

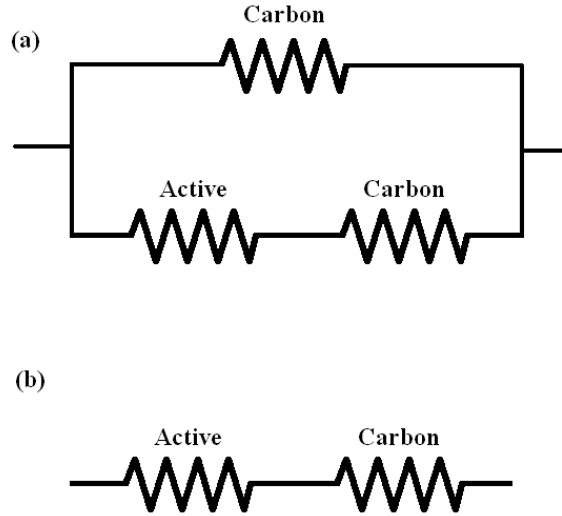


Figure 5.12: Different resistive circuits that describe the electrode system for: (a) when the carbon domain is above the percolation threshold. (b) when the carbon domain is below the percolation threshold.

For such a system the limiting electronic resistance is whichever resistor is the largest. Generally, the overall conductivity of commercial electrodes depends both on the carbon domain conductivity and the active material conductivity. The PSG model shows that the system described by Figure 5.12(b) generally exists when the ratio of σ_A/σ_C is greater than 0.05 and carbon domain volume fraction is below 20%. Once a σ_A/σ_C ratio of 0.05 is achieved, overall conductivity can be varied the most by either varying carbon volume fractions or by increasing the carbon domain conductivity. This has been shown in several experimental and theoretical studies of how adding a much more conductive active material into an electrode only marginally improved performance after calendaring [87, 88].

When the second electronic circuit has active material that is not conductive enough to provide an electronic percolation network, then overall electronic conductivity goes to zero.

This electronic circuit occurs when the carbon domains are below their percolation threshold and the active material conductivity is very low, i.e. ratio of σ_A/σ_C lower than 0.05.

Figure 5.13 shows electronic results from the PSG model at different carbon domain volume fractions as well as different active-to-carbon domain conductivity ratios. The PSG model electronic results can be seen for three electrode porosities. The first electronic circuit can be seen in how the PSG model's overall conductivities is similar in value at high carbon domain volume fractions despite changing the active domain conductivity by varying the σ_A/σ_C ratio. This is shown in the semi flat curves in Figure 5.13 at high carbon domain fractions. Once the percolation limit of the carbon domain has been reached relatively little increase in overall electronic performance can be obtained by changing the conductivity of the active material. We can observe how the overall conductivity shown in Figure 5.13 does not increase very much after after σ_A/σ_C ratios of 0.05. However, the overall conductivity can still be increased by changing the conductivity of the carbon domains or changing the volume fraction of the carbon domains.

The second electronic system is shown in Figure 5.13 where overall electronic performance changes dramatically with varying the σ_A/σ_C ratio at low carbon domain volumes (12% carbon domain curves for example). For the second electronic system is best optimized by maintaining at least a σ_A/σ_C ratio of 0.05 and the highest possible carbon domain conductivity.

For the second electronic circuit, if the active domain conductivity is too low to obtain the percolation threshold, then the overall conductivity is independent of the carbon domain conductivity because the active material is limiting electronic performance. This electronic system is shown in the low-carbon-domain-volumes results shown in Figure 5.13. For such a system, small changes in the active domain conductivity will have large effects. If active domain conductivity cannot be increased, then in order to achieve overall conductivity, it is necessary to increase the carbon domain volume fraction to above its percolation limit.

Figure 5.13 can be used as a reference for other electrode systems to better understand what type of electronic system one is dealing with. If active material conductivity is extremely low, higher carbon domain volumes are unavoidable for electrodes to react. If the active material conductivity is sufficient to provide overall percolation, varying the carbon domain volume can be used to tune electrode performance, subject to trade-offs between the ionic and the electronic losses.

5.5.4 Relationship between porosity and carbon domain volume

As is visually shown in Figures 5.14-5.16, there is a trade-off with the volume of pore domain associated with adding additional carbon domain. Because the carbon domains are around 63% porous, the absolute maximum of carbon that can be added depends on the overall porosity. This means the electrodes manufactured with higher carbon contents tend to have higher overall porosities. As will be shown in Chapter 6, even with calendaring at high carbon contents, electrodes will relax back to a higher porosity. Figure 5.11 shows the maximum carbon domain fraction is 51% for the 34% porosity electrode and then up to 81% carbon domain fraction for the 51% porosity electrode.

Extremely high-rate electrodes (170 C-rate to 370 C-rate) have been manufactured by others, but they required dry volume carbon contents of 65 wt% (which would correspond to electrodes in which the pores are completely filled by carbon) [89]. Due to the high microporosity of the carbon domains, adding 65 wt% of carbon would create an electrode with a high volume of electrolyte. The electrolyte in the micropores of such a domain could contain a high enough mass of lithium to completely react the small fraction of active material in the electrode without any transport of ions from the anode. The high electronic conductivity added to a shortened ionic transport pathway effectively lowers electrode resistances. This may be why such high carbon fractions can give discharge rates of 370 C-rate. However, the

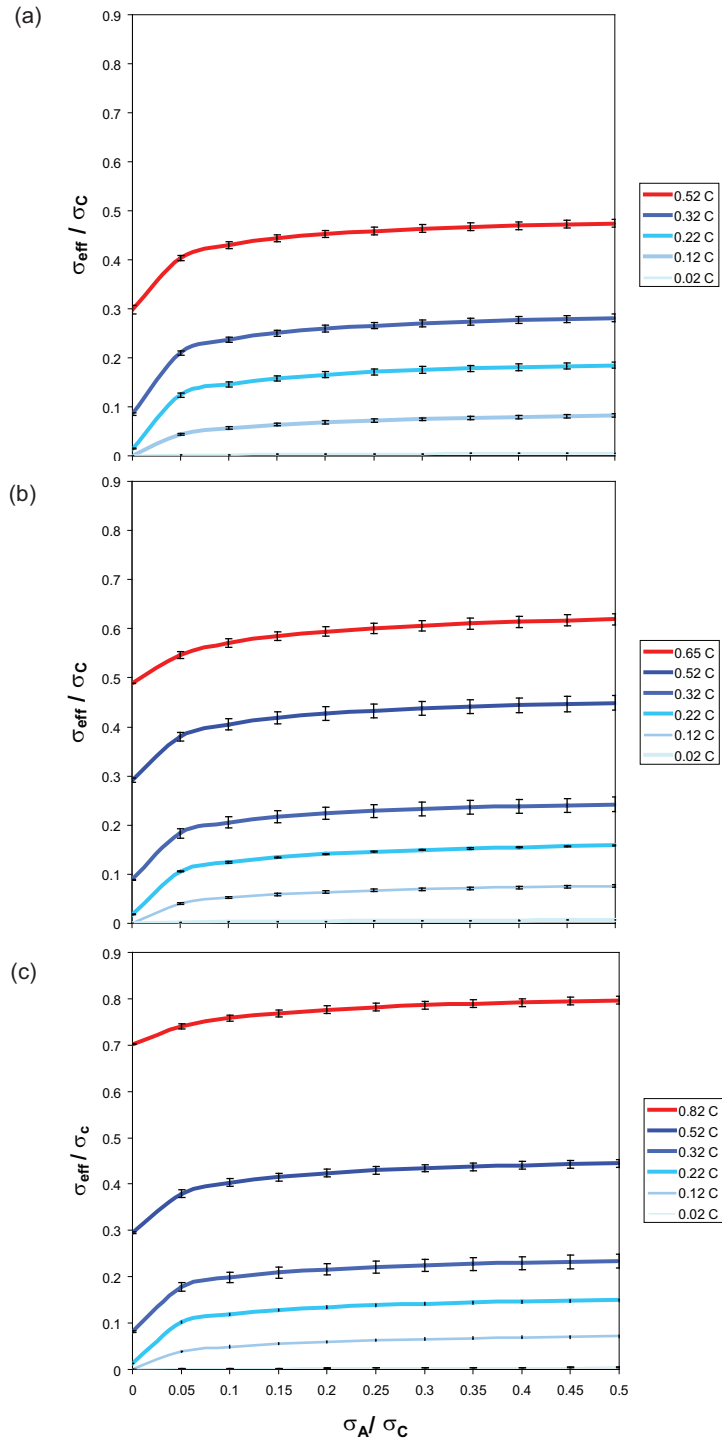


Figure 5.13: Electronic resistances at different carbon domain fractions (ϵ_{C}) and $\sigma_{\text{A}}/\sigma_{\text{C}}$ ratios for porosities of: (a) 34% (b) 45% (c) 51%

energy capability on a weight basis of such electrodes was severely limited due to there being such a high weight proportion of inert components (carbon and electrolyte).

5.5.5 Ionic pathways

The ionic pathways strongly depend on the porosity of the systems as previously shown in Figure 5.9. Figure 5.11 further shows that the ionic pathways are greatly affected by the carbon domain fractions. By adding carbon domain volume, ionic pathways decrease in the 34% electrode (Figure 5.11 (a)) from an inverse tortuosity of 0.24 to 0.05. Increasing porosity can somewhat mitigate the reduction of ion transport upon adding carbon domain as shown in Figures 5.11 (b) and (c).

5.5.6 Structure changes and its effects

Figures 5.14-5.16 show 2D slices from the PSG model for three different porosities as well as different volume fractions of the different domains. From these images we can visually see ionic and electronic pathways as well as inspect the results and compare them to the SEM/FIB images. Figures 5.14(b), 5.15(b), and 5.16(b) are all at baseline levels in which the carbon, pore, and active material volume fractions are nearly at the (imaged) values in Table 3.1. Other images were created by varying the carbon domain fractions from the baseline values.

Figure 5.14 shows how the PSG code generates structures as the carbon domain is varied at 34% overall porosity. Figure 5.14(a) shows an electrode with hardly any carbon domain. It comes as no surprise that this structure produces some of the lowest electronic conductivity values as seen in Figure 5.11. At the same time, this structure exhibits ionic resistances that are still relatively large compared to higher porosity electrodes.

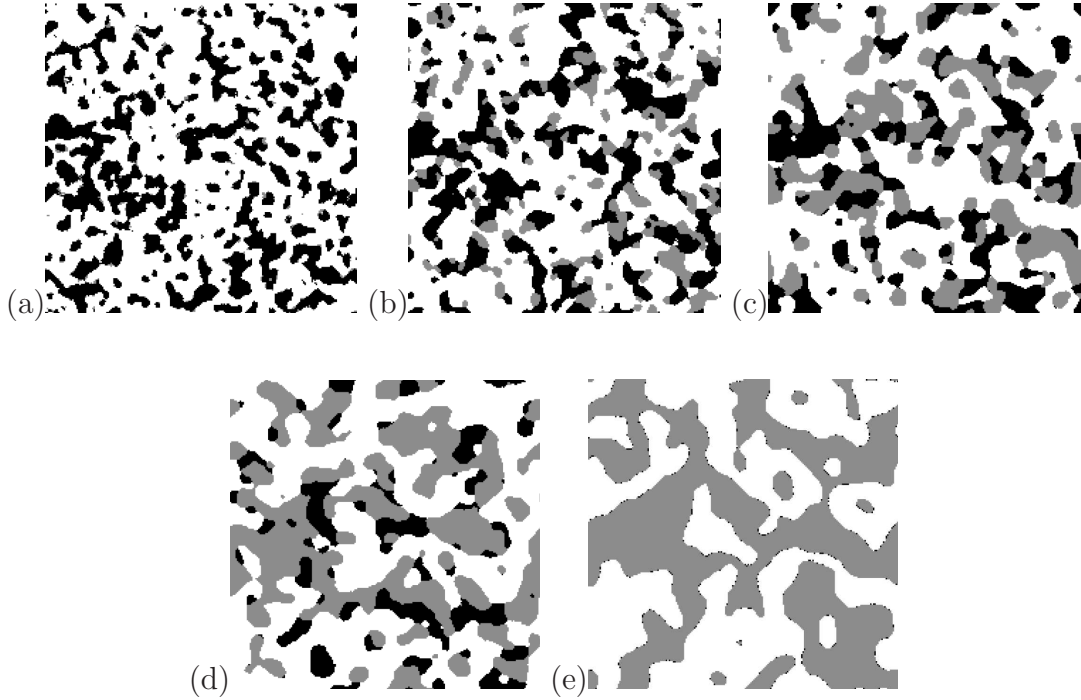


Figure 5.14: 2D slices from PSG model configurations for 34% porosity. The carbon domain fractions are (a) 1%, (b) 11%, (c) 21%, (d) 31%, (e) and 51%.

Figure 5.14(d) shows an electrode which has had its pore domain completely filled with carbon domain. While the overall porosity of the electrode has still been maintained at 34%, the pore has been adsorbed into the carbon domain. The expected volume fraction of carbon being added to the electrode is approximately only 6% at a 2:1 binder-to-carbon ratio and 8.6% at a 1:1 binder-to-carbon ratio. As a comparison, Saft electrodes were manufactured at only 2% carbon volume fractions. This shows how seemingly little changes in added carbon or binder may dramatically affect the carbon domain volume.

Figures 5.15 and 5.16 show how a greater pore volume supports a higher volume fraction of carbon. Because of the higher porosity a larger fraction of carbon can be added before the macro-size pores get plugged up with microporous carbon domain. Figure 5.14(e) is at the maximum allowable carbon domain fraction for 34% overall porosity. Notice that the volume of pore domain is still significant in comparison to Figure 5.16(e). The ionic resistances are

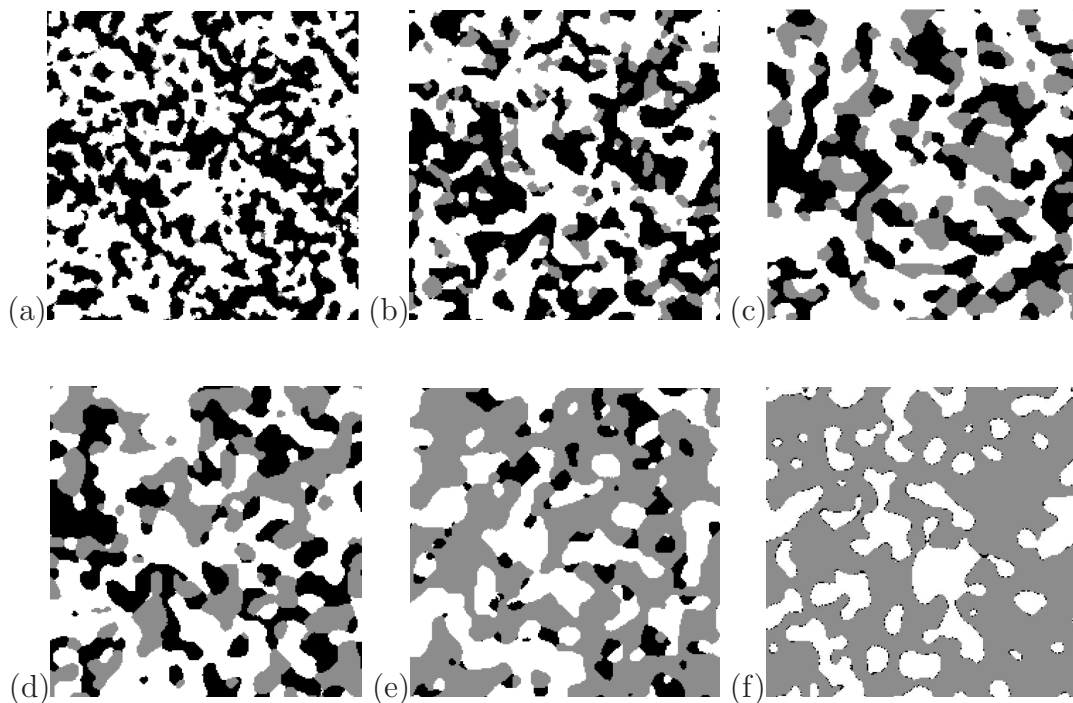


Figure 5.15: 2D slices from PSG model configurations for 45% porosity. The carbon domain fractions are (a) 1%, (b) 11%, (c) 21%, (d) 31%, (e) 51%, (f) and 66%.

lower in comparison with the 34% porosity 51% carbon domain fraction but the electronic resistances are a little poorer, as shown in Figures 5.11 (a) and (b). Figure 5.15(f) is at almost the maximum possible carbon domain volume fraction. Both the ionic and electronic resistances are still better than the 34% porosity 51% carbon domain electrode. Figure 5.16 shows similar results in which the higher porosity of the electrode allows for the addition of more carbon while maintaining pore pathways. All this shows that in battery electrode manufacture, porosity and carbon volume fractions are not independent parameters and must be optimized together.

Figure 5.16(e) shows the SG model structure at a 51% electrode porosity with enough carbon domain to correspond to the maximum carbon domain that the 34% porous electrode could handle. Here the phases are agglomerating together. The carbon domain agglomerates are above the percolation threshold, which decreases the electronic dependence of this struc-

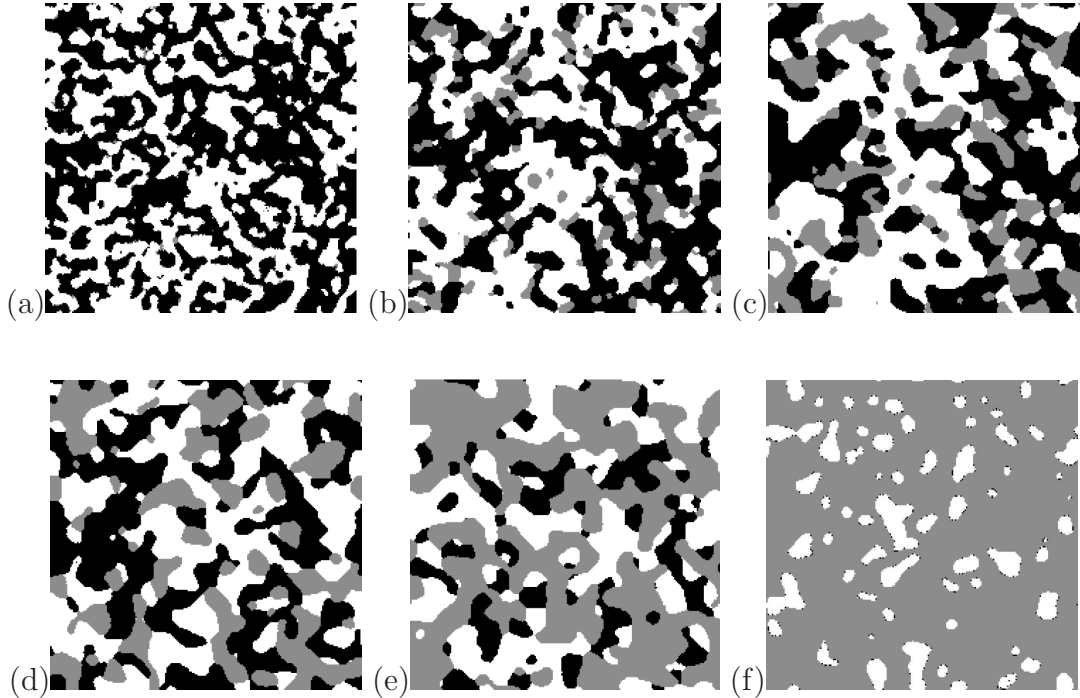


Figure 5.16: 2D slices from PSG model configurations for 51% porosity. The carbon domain fractions are (a) 1%, (b) 11%, (c) 21%, (d) 31%, (e) 51%, (f) and 81%.

ture on active material conductivity. Previously we saw that at around 21% carbon domain, the electrodes no longer depended on active material to provide bulk electrical connections, (see Figure 5.11). This means that completely non-conductive active materials require at least 2.3 wt% to 3.5 wt% of carbon additive (depending on binder-to-carbon ratio) to achieve the electronic percolation threshold. This provides a lower bound estimate for conductive additive volume fractions.

5.5.7 PSG model limitations

Figures 5.16(a), 5.15(a), and 5.14(a) are all at very low fractions of carbon domain. The shape of the active material domains at low carbon domain fractions is different from the active domains shown in Figures 5.16(e), 5.15(e), and 5.14(d).

The difference in active domain shape comes from the PSG model being based on MC principles. This means as volumes of the domains are changed, the energy of the system changes causing a different equilibrium to be achieved. For example, when the maximum of carbon domain volume was added at the 51% electrode porosity, as seen in Figure 5.16(f), we see that the PSG model starts to over agglomerate the carbon domain. This is causing the active material domains to have a higher surface area (similar to the low carbon domain images). The active material particles shown in Figure 5.14(a) have a different morphology (higher surface area) than the active material particles shown in Figures 5.14(c) and (d). The same trends are shown for the 45% and 51% PSG model structures. The change in active material morphology with varying fractions of carbon domain might not be a problem, because commercially made electrodes are not fabricated at the composition extremes illustrated here. It is more important that the model be accurate near the baseline values used to parametrize it.

It might be possible to fix the problem of changing active material morphology by adding additional constraints to the system. This has been mentioned before in the form of $C_2(r)$ function, which is one possible 3D structure constraint [90], or another such 3D structural constraint statistic. The $C_2(r)$ function or other statistical parameters of active domain phases may not be dependent upon volume fraction. This would allow for the PSG code to provide more accurate reconstructions with 3D structural constraints applied only on the active material domain.

5.5.8 Experimental results of varying carbon fractions

It is important to note that the carbon domain is composed of carbon binder and micropores. This means that at 51% carbon domain volume the carbon volume only represents 11 to 12 percent dry carbon volume with about 16 percent PVDF dry volume fraction. We have

found experimentally at calendered porosities of 50% that at dry carbon volume fractions at 10% electrode performance stopped improving. The experimental results of electrodes where both the PVDF and electrode porosity were held constant but the carbon fraction was allowed to vary are shown in Table 5.2. You can see in Table 5.2 how as carbon weight percentage is increased both the final porosity increased (even after calendaring) as well as performance plateaued. It is important to note that in these experiments PVDF to carbon ratio was being changed. This may mean that the carbon agglomerates were changing in structure and conductivity as more carbon was added.

We believe that the cells we were making were in fact originally electronically limited. The PSG code suggests that carbon fractions of 10 to 12% dry weight percentage will begin to form carbon domains that will clog up the pores. We found at room temperature we were able to experimentally still have electrode performance even at high carbon fractions due to ionic limitations not being as severe as the electronic limitations. Experimentally we see that the limit of high-power performance coincided with the carbon volume fraction at which the PSG model predicts the maximum of carbon volume fraction takes place. Further addition of carbon fractions resulted in overall porosity increasing despite attempts to calender. Experimentally the effects of changing the carbon content of a cathode has been looked at by V. Battaglia's group as well [91] but they were just observing electronic resistance changes rather than full cell performance.

We didn't try to optimize the cells shown in Table 5.2 for thickness, but we note that very thick electrodes perform very poorly at high rates. Whether this poor performance is from electronic or ionic resistances has yet to be determined. An accurate full electrochemical model will be helpful to show and understand the transport trade-offs with thickness.

Table 5.2: Varying performance at different discharge rates and carbon fractions with cell of approximately 50% porosity. PVDF was held at 3% volume fraction.

Carbon weight	Porosity (%)	C/20 (mAh/g)	1C (mAh/g)	2C (mAh/g)	5C (mAh/g)
3%	50	124	112	91	36
6%	51	129	123	109	28
10%	52	128	123	114	45
11.3%	54	130	121	108	41
12%	59	128 (C/5)	127	119	45
12%	59	131 (C/5)	130	115	41

5.6 Conclusions

The PSG model shows the trade-offs between the electronic and ionic transport properties upon changing carbon domain fractions. Because of the trade-offs between electronic and ionic transport, an optimum composition and porosity exists for a given rate of discharge. Such optimums generally require that the series transport resistances, ionic and electronic, are the same magnitude. Changing volume fractions from a optimum level will lead to worse electrode performance due to a large resistance controlling behavior. Because different resistances have a different dependence on discharge rate, different duty cycles require different volume fractions in order to optimize them.

We also learn that the ionic conductivity will quickly decrease with added carbon. Above 11-12 wt% of dry carbon, the pores are generally plugged up with microporous carbon domains. This would cause such electrodes to have ionic pathways which are only at 5% of the electrolyte's intrinsic conductivity. While ionic limitations did not shut down electrodes of a less than 100 micron thickness at room temperature, this does not mean that at lower temperatures, where the intrinsic ionic conductivity and diffusivity is severely decreased, that

the ionic conductivity could quickly become the limiting factor of cell performance. Future work can be done that will incorporate a 3D electrochemical model with the SG model's predicted structures to help determine optimal electrode volume fractions at different rates as well as at different temperatures.

Chapter 6

Electronic conductivity experiments

6.1 Introduction

Internal electrode resistances come in three forms: ionic and electronic resistances and kinetic losses. When charge is passed through a battery, total resistance can be determined. Unfortunately a measurement of total resistance cannot determine the magnitude of the component electronic, ionic, and kinetic resistances, which will also be different at each electrode and location within that electrode. The aim of the experiments done in this chapter is to determine the electronic component of electrode resistances.

We showed in Chapter 5 that, for battery systems in which electrode structure and active material conductivity make electronic transport facile, the overall electrode conductivity is primarily dependent on the carbon domain conductivity. Thus it is important to understand electronic transport in these carbon domains. While the conductivity of pure components is better known, the conductivity of mixtures such as the carbon domains or entire electrodes is not as well documented or known. Thus additional experimental measurements are needed for these porous electrode materials.

This chapter discusses what has been done in the past as well as this work's experiments, which were used to measure the electronic conductivity of battery materials and films. This work is complementary to work mentioned in Chapter 3 in which ionic transport through films was determined [7]. Conductivity measurements can be classified as either an intrinsic measurement (pure-component conductivities) or as overall effective conductivity measurements (conductivity of mixtures of components). The following sections describe the different conductivity measurement techniques found in the literature as well as the methods developed and used here.

6.2 Intrinsic conductivity measurements

Measurements of intrinsic conductivities of pure components come in two types of materials: single-crystal or pelletized. Single-crystal measurements are made on single crystals of a material. Single-crystal measurements are difficult to do because growing a single crystal with uniform geometry is not easy [77]. Also the measurements are possibly not applicable to active particles used in cells due to particles having random orientations (which would change the plane and hence the conductivity of particles) as well as possible significant defect-filled or rough surfaces of particles used in real batteries.

Pelletized measurements are made on aggregated particles of a material that has been compacted into a pellet. Pelletized measurements are easy to perform and can be done on actual battery particles. Following compaction of the pellet, electronic resistance is measured by confining the pellet between two electrodes. Because no special manufacturing process is used, any battery material or mixture of materials can be tested.

Single-crystal and pelletized particle measurements generally give very different measured conductivities [76]. This is because, unlike single-crystals, pellets have contact resistances be-

tween particles in addition to the intrinsic resistance of the particles themselves. The contact resistance between particles makes it more challenging to determine intrinsic conductivities.

As an example, pelletized carbon black conductivity has been reported as a function of pressure as ranging between 5 and 30 S cm⁻¹ [92]. Other workers have shown that carbon black conductivity varies significantly with manufacturing processes and the pressure pellets were measured at [93]. The intrinsic conductivity of carbon can be around 285 S cm⁻¹ [94]. However, the real question that needs to be answered for the model is what is the conductivity of the carbon black and PVDF domains. Also for model validation purposes, overall cathode conductivity needs to be determined.

As was mentioned before, the intrinsic single-crystal conductivity of LiCoO₂ has been obtained [77] as well as pelletized values [31, 78].

All electronic measurement techniques require at least two electronic probes. There is always a contact resistance between an electronic probe and the tested material. In order to succeed, a conductivity measurement method must either eliminate the effects of the probe contact resistances, change the geometry so as to minimize them, or use multiple experiments to correct for them. An example of changing geometry is pellet measurements where the bulk resistance of the pellet is much greater than probe contact resistances. In such pellet measurements contact resistances are generally ignored [93]. In order to eliminate probe contact resistances, a simple method that is generally used is the four-point probe method. More on these techniques is discussed below.

6.3 Overall effective conductivity measurements

The conductivity of the carbon domains is not an intrinsic conductivity measurement because the carbon domains are a microporous mixture of materials. Also measuring overall conductivity of electrode films is useful in validating the model. So for this work, a method

that could measure the effective conductivity of porous films was needed. We have found that this is not an easy task.

Overall effective conductivity measurements (conductivity of mixtures of components) are made on materials in two forms, namely pelletized and films. Pelletized measurements have been made for mixtures of battery materials [93], However, because electrode manufacturing processes are so different than the process used to make pellets (differing in the use of solvent, heat-treatment [95], and compression), the actual electronic resistances of electrodes are likely much different than for the pelletized materials tested [96].

Film measurements are done on real electrodes, which is what we wish to measure. Films are thin and generally cast on a conductive backing known as a current collector. Because of the thinness of films, their bulk resistances in the normal direction are not large enough for the contact resistance between electronic probes and the film to be negligible. Moreover, the conductive current collector makes using tangential measurement techniques like the four-point probe method not reliable, as discussed in the next section.

Measuring film conductivities is most reliably done when one can delaminate or remove the film from its conductive backing. Delamination of porous films with sub-100 μm thickness causes them to lose much of their mechanical stability. This resulted in LiCoO_2 (Saft) films being too brittle to make accurate measurements. However, carbon/binder films proved to be more robust, and delaminated carbon/binder films could be measured using various techniques. This meant for the work discussed in this chapter that we mostly did methods development and tests on carbon/binder films.

In order to better determine effective film conductivities, three methods were explored: tangential probe, perpendicular AC impedance, and measuring heat transport as a proxy measurement technique.

The tangential probe method is based on changing the geometry so that the probe contact resistances become smaller and quantifiable. To do this, films are removed from the current

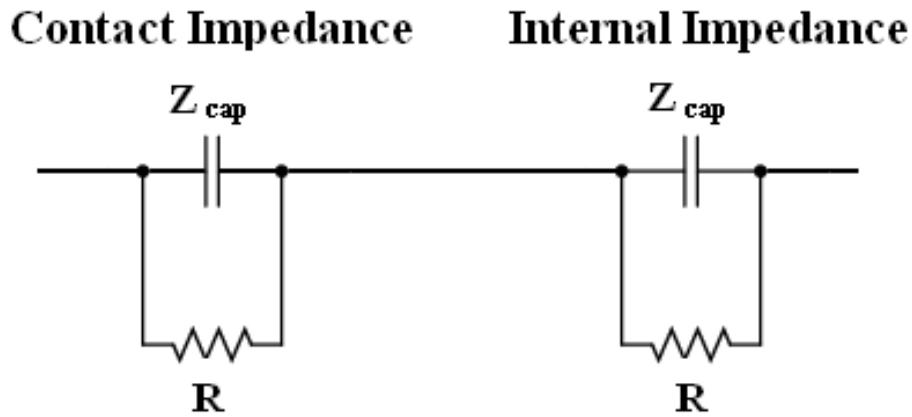


Figure 6.1: Equivalent circuit of dry electrode impedance.

collector and placed across a planar set of probes. The direction that bulk conductivity is being measured is in the same tangential direction to the surface as that measured with the four-point probe method. Measuring conductivity in a tangential direction will give the normal bulk conductivity of a film if the material is isotropic. Isotropy is likely a reasonably accurate assumption, but this has not been proven experimentally. And it should be noted that calendaring is in a direction which may cause non isotropic film structures.

The perpendicular AC impedance method is an attempt at eliminating probe contact resistances without destroying the test sample. The perpendicular AC impedance method tests conductivity normal to the film surfaces and over a range of AC frequencies with two probes placed on the top and bottom of the film. The idea behind perpendicular AC impedance was that contact resistances may be attenuated relative to conduction resistances at particular frequencies. Figure 6.1 shows the idealized AC circuit of a film measurement. If the time constants of the contact and internal (bulk) impedances are different, then as frequency is varied, one resistance can become effectively short-circuited. This could allow for both the contact and internal resistances to be determined with just two probes.

Heat transport as a proxy method is also an attempt to eliminate contact resistances. Heat transport can be measured without using probes, instead using an infrared camera to find the temperature of a surface. Differences in structure and material composition of the film can change the heat transport through a film. The goal is for the measured thermal conductivity to be related to structure using the SG model in order to validate the model's structures and then use the model to determine electronic transport. Also heat transport measurements could easily be done commercially as a non-destructive test of film quality.

6.4 Four-point probe on delaminated films

The four-point probe uses two of the four probes to pass the current and measures the voltage with the other two probes as shown in Figure 6.2. Because little to no current is being passed by the voltage-measuring probes, the contact resistances do not significantly affect the measurement. The bulk resistivity, ρ , as measured by a four-point probe is

$$\rho = \frac{\pi}{\ln(2)} t \left(\frac{V}{I} \right), \quad (6.1)$$

where t is the thickness of the film in cm, V is the measured voltage, and I is the impressed current [97]. Eq. 6.1 is true only for uniform thin films of infinite extent. It is also reasonably accurate for finite geometries as long as the probe is not placed close to the edges of a sample. For our experiments the size of the film was 2 cm by 2 cm, which was much larger than the spacing between the probes (1/16 of an inch or approximately 0.159 cm).

Because of the effective elimination of contact resistances, the four-point probe technique is the most common method used for measuring electronic conductivity [97]. Unmodified Li-ion electrode films have multiple layers (i.e. film on a current collector) which means that the different layers of resistances may only be determined indirectly from a tangential measurement like the four-point probe. Indirect calculations incorporate specimen geometry,

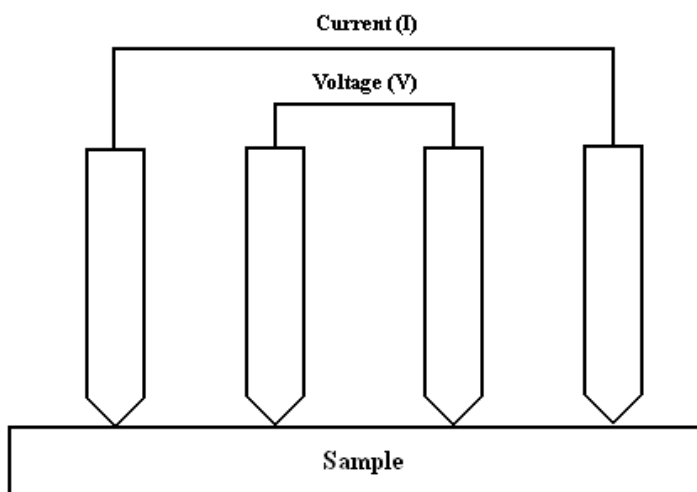


Figure 6.2: Four-point probe setup.

probe position, probe spacing, and the possibility of layers with different conductivity. However, actual four-point probe measurements using indirect calculation methods of cathode films still attached to their current collectors have not yielded reliable results [96, 98]. This is largely due to the current collectors being so much more conductive than the cathode films. The results become greatly subject to instrumental error due to very small measurement variations being the key to determining electrode film conductivities. A possible secondary problem is that indirect calculation methods assume that each probe has the same substrate underneath it. Because probe tips and particles have similar radii of curvature, local variations in electrode particle morphology may violate the assumption of uniformity.

More success with the four-point probe method has been found by fabricating films on a non-conductive glass substrate and then testing with a four-point probe [91, 99]. However, manufacturing films on non-conductive substrates is not a straightforward solution in the present case, because the manufactured film may not have the same structure as films fabri-

cated on metal foil current collectors. Also, processing steps such as calendaring are difficult to achieve on films attached to glass.

In addition, the major downside of the four-point probe method is that controlled compression of the sample film is difficult to achieve. Electrode structure and conductivity are dependent on the pressure; actual lithium-ion cells are generally produced so that electrodes are under significant pressure. Later in this chapter we show how significant the effect of pressure is on the film conductivities.

To better understand the electronic properties of carbon domains, we tested films containing only carbon black and binder to simulate the carbon domains and measured their effective conductivities. We described in Chapter 4 ionic measurements and fabrication of these simulated carbon domain films. We electronically tested 63:37 (\approx 2:1) and 46:54 (\approx 1:1) binder-to-carbon weight ratios, which represent reasonable possible cases of all the electrode binder going into the carbon domains or only half of the binder going into the carbon domains, respectively.

Despite not being able to apply a defined and uniform pressure, we still tested delaminated carbon/binder films using a four-point probe. Delamination of the carbon/binder films removed the need for unreliable indirect calculations of conductivities. Resulting measurements for the 2:1 binder-to-carbon ratio were $1.917 \pm 0.067 \text{ S cm}^{-1}$ with the uncertainty given by the standard deviation of the mean. This result is comparable to the tangential probe electrode conductivity measurements made at 73.6 kPa as shown in Figure 6.7. Measurements for the 1:1 binder-to-carbon ratio were $5.675 \pm 1.12 \text{ S cm}^{-1}$, which is lower than corresponding tangential probe measurements as shown in Figure 6.7.

The four-point probe measurement results may differ from the tangential probe measurements due to a difference in pressure. The pressure was different because the point probes are pressed onto the samples with an unknown pressure and the films were only being compressed where the probes are in contact. As pressure is applied by small probes, the pressure

experienced by the film is non-uniform in its spatial nature as well as unknown in magnitude. The next subsection shows in greater detail the role pressure plays in overall conductivity.

6.5 Tangential probe

As mentioned before, the tangential probe method changes the geometry of the measurement so as to make the contact resistances small relative to bulk resistances. To do this, the tested films were removed from the current collector by delamination. Each delaminated film was placed on a rigid substrate with two planar probe electrodes. Two substrates were made with varying probe gap distances. The experimental setup of the tangential probe experiment is shown in Figure 6.3. Assuming that the contact resistances are similar for the two substrates then both the probe contact resistances and overall effective electronic resistance can be determined from two experiments.

The substrate and planar electrodes were constructed as follows. Copper clad circuit boards formed the primary substrate. These boards were etched with warm nitric acid to remove copper to form the two boards shown in Figure 6.3. Two substrates were created, one with a 0.3 cm gap and one with a 1 cm gap. The gaps were filled with non-conductive polyethylene polymer to level the surface and prevent the cathode films from sagging into the gap. The electrodes were plated with nickel and then gold to prevent an oxide layer from forming on the surface. Leads were soldered directly to the substrate's copper metal surface for external connection to a multimeter.

The test procedure used is illustrated in Figure 6.4. Dry free-standing electrode films with dimensions $2\text{ cm} \times 2\text{ cm}$ and different porosities were placed on the substrate so that both sides of the film contacted equal portions of the two copper metal surfaces. A glass slide was then placed on top of the film and a foam pad placed on top of the glass. Different weights were then placed on top of the foam pad. The foam pad helped to evenly distribute

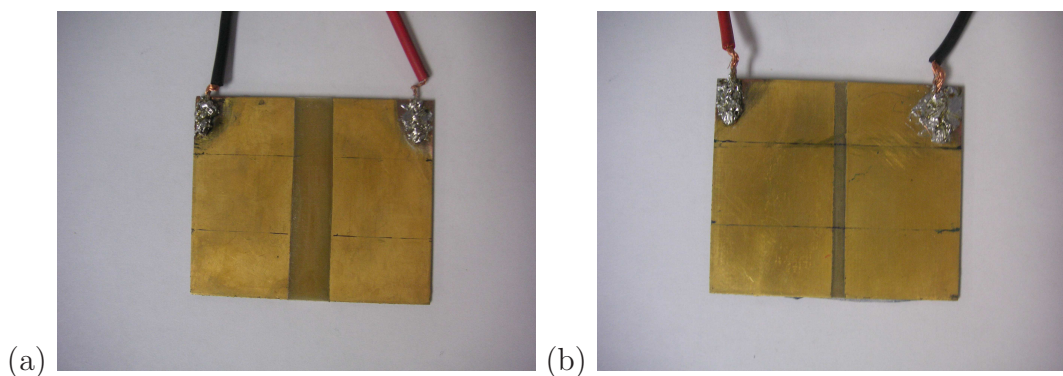


Figure 6.3: Images of tangential probe experimental setup with different gap distances: a) 1 cm gap and b) 0.3 cm gap.

the weight and thus pressure. After each measurement, each film was completely removed and then repositioned. For dry conductivity measurements, the procedure was generally repeated two times for each gap length.

Battery electrodes operate with their pores filled with electrolyte. PVDF binder can absorb electrolyte, and the resulting polymer swelling (10-20% by volume) likely affects overall structure [100, 101]. As a result, we measured films after they were wetted with diethyl carbonate (DEC) to imitate the effect of solvent and electrolyte interacting with the dry film. DEC was used because it is readily available and is liquid at room temperature. Commercial battery electrolyte solutions commonly mix DEC with ethylene carbonate (a higher melting solvent) and with LiPF_6 . LiPF_6 is sensitive to the oxygen in the air so it was not added to the DEC for our tests. DEC should by itself still be able to give a reasonable indication of how swelling of PVDF binder affects overall conductivity.

The dry conductivity procedure was adapted to enable measurement of the resistance when the cathode or carbon film was wetted with solvent. Five drops of DEC were placed on the cathode and allowed to wet the pores prior to placement of the glass slide. Measurement were taken on the two electrodes with varying gap lengths. The measurement was taken after one hour of settling because we found that time was needed for the film measurements

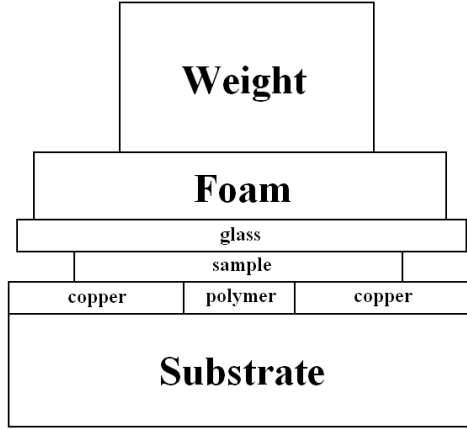


Figure 6.4: Illustration of tangential probe experimental setup.

to stabilize. While the film measurement usually stabilized sooner, we measured everything after one hour for consistency. Fewer measurements were taken with the wetted cathode films due to their extreme fragility, particularly when wetted.

The reason for having two different gap distances between the copper probes is to determine and eliminate the contact resistance between the electrodes and the cathode films. Resistivity ρ is defined as follows

$$\rho = \frac{1}{\sigma_{\text{eff}}} = \frac{R A}{L}, \quad (6.2)$$

where R is the gap resistance, A is the cross sectional area, and L is the gap length. The measured resistances are graphed versus the length of the gap between the electrodes in Figure 6.5. The fitted linear intercept of these data gives the contact resistance. The slope is equal to R/L in the above equation and when multiplied by the cross sectional area is equal to the bulk resistivity of the free-standing cathode. To illustrate the above procedure, Figure 6.5 shows the data from a wet conductivity measurement of a 1:1 binder-to-carbon film at 12.2 kPa as well as a line fitted to the data from which the slope and intercepts were obtained.

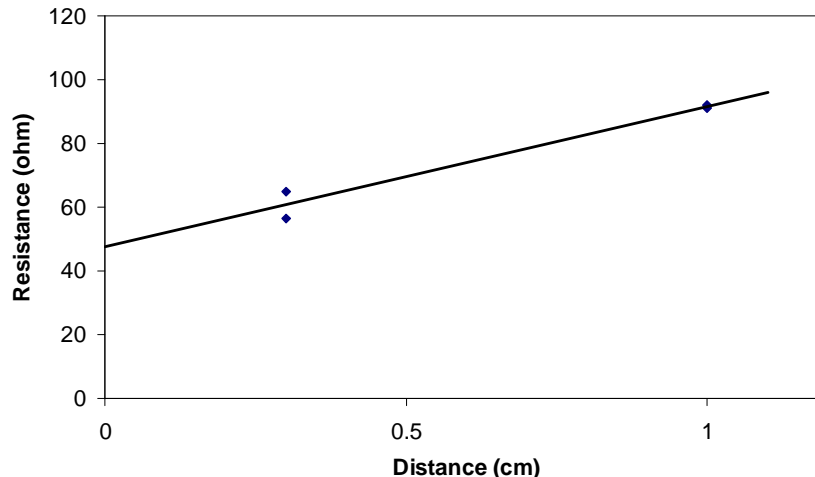


Figure 6.5: Resistance measurements of dry free-standing carbon film at a 1:1 binder-to-carbon ratio and 12.2 kPa applied pressure. The two points at 1 cm distance nearly overlap. The line is a least squares fit of the points.

As mentioned before, after delamination, LiCoO_2 composite electrode mechanical strength is very low, which leads to cracking during electronic conductivity testing. When the electrodes were wetted with DEC, their mechanical strength degraded even further, making them even harder to handle. Because of this, we have been unable to get wet conductivity measurements for commercially made cathode films.

6.5.1 Electronic measurements of electrode films

We were able to obtain dry electronic conductivity measurements at two of the four different porosities. We measured the dry electronic conductivity of one 51% porosity Saft film at 73.6 kPa, which was $0.210 \pm 0.004 \text{ S cm}^{-1}$, where the uncertainty is the 95% confidence region. We were able to measure four 45% porosity Saft films at 73.6 kPa. The results of these measurements are shown in Figure 6.6. Each of these films was cut from the the same continuous roll of cathode material. One of our motivations for contracting a commercial battery maker to fabricate electrode material was to reduce the variability inherent in electrode manufacture.

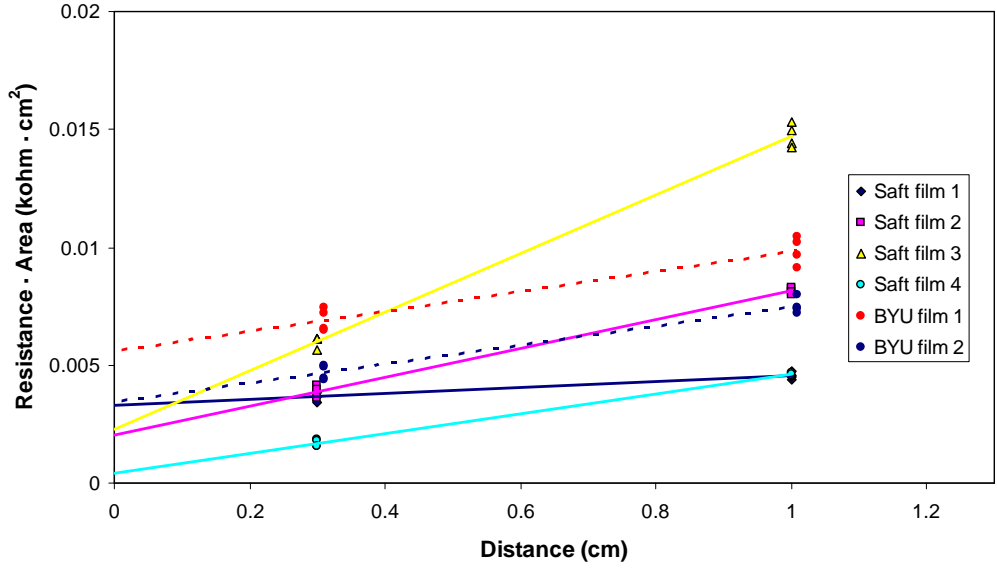


Figure 6.6: Area-specific resistance of approximately 45% porosity films measured at 73.6 kPa pressure. Films were fabricated by Saft or in our laboratory. Lines are a guide to the eye. BYU film data are slightly offset.

Thus, it was surprising to see the variability shown in Figure 6.6. We believe the measurements on Saft film 4 may be the most accurate due to low contact resistance (shown by the intercept at zero distance) and measurement uncertainties. Saft film 4 had a measured conductivity of $0.238 \pm 0.005 \text{ S cm}^{-1}$. By comparing the results for the two porosities, we see that electronic conductivity increased slightly with a decrease in overall porosity. This is the expected result, as calendaring or reducing the porosity generally brings adjacent particles into better contact. However, variation between the measured conductivity of the four 45% porosity Saft films was relatively large, and with only one film measured at 51% porosity, it is difficult to quantify the effects that porosity had on the conductivity of these films.

Because we found that it was difficult to delaminate and maintain structural integrity of the Saft films, we fabricated thicker films with the same composition as the Saft films, indicated as BYU films 1 and 2 in Figure 6.6. We found that making the films thicker

Table 6.1: Tangential probe electronic measurements. Uncertainties are standard deviations from a least squares fit of four measurements at each gap distance.

film	porosity	carbon wt %	contact R (Ω)	ρ ($\Omega\cdot\text{cm}$)	σ (S/cm)
Saft 51%	0.51	2	75.428 \pm 6.692	4.760 \pm 0.126	0.210 \pm 0.006
Saft 1 45%	0.45	2	288.393 \pm 614.6	1.256 \pm 9.472	0.796 \pm 6.008
Saft 2 45%	0.45	2	195.85 \pm 14.09	6.106 \pm 0.199	0.164 \pm 0.005
Saft 3 45%	0.45	2	141.14 \pm 17.82	12.457 \pm 0.388	0.080 \pm 0.003
Saft 4 45%	0.45	2	30.857 \pm 6.942	4.185 \pm 0.131	0.239 \pm 0.007
BYU 1 45%	0.43	2	201.179 \pm 14.274	4.212 \pm 0.543	0.237 \pm 0.031
BYU 2 45%	0.46	2	128.146 \pm 8.980	4.013 \pm 0.331	0.249 \pm 0.021
BYU 3 40%	0.40	4	72.53 \pm 4.408	1.134 \pm 0.102	0.882 \pm 0.792
BYU 4 45%	0.45	4	100.11 \pm 37.209	1.456 \pm 0.509	0.687 \pm 0.240
BYU 5 51%	0.51	4	59.58 \pm 4.172	1.242 \pm 0.055	0.805 \pm 0.036
BYU 6 45%	0.45	6	104.6 \pm 3.856	0.667 \pm 0.048	1.499 \pm 0.109
BYU 7 45%	0.45	6	110.92 \pm 4.118	0.592 \pm 0.052	1.690 \pm 0.148
BYU 8 45%	0.45	6	54.78 \pm 5.921	0.740 \pm 0.061	1.351 \pm 0.112

increased their mechanical stability. These replicate films were tested at three pressures, namely 73.1 kPa, 48.6 kPa, and 11.7 kPa. However, we found that the measured conductivity did not change significantly with pressure, except that there was greater uncertainties at lower pressures. As a result we report just the 73.1 kPa data in all the electrodes in this section. Table 6.1 shows the electronic results for all the film that were tested. We found that both BYU films had similar results to Saft film 4 and Saft 51%. We learned from these measurements that the BYU-fabricated films are reasonable facsimiles to the Saft-fabricated films, probably due to greater film thickness.

6.5.2 PSG model validation versus experiments

The PSG model was developed in an effort to provide a way to predict both electrode structure and transport properties. However, the PSG model predictions described in Section 5 needed to be validated experimentally before PSG model predictions could be believed. In order to validate the PSG model predictions regarding changes in electronic conductivity with varying carbon domain fractions, we also created electrode films with varied amounts of carbon and PVDF. Electronic results of varied amounts of carbon and PVDF are shown in Table 6.1. One set of electrodes was at double the carbon and PVDF composition of the Saft electrodes. The electrodes were calendered to three different porosities and placed under 73.1 kPa of pressure. The variability on the electrode conductivities led us to believe that variability in manufacturing steps can lead to greater electronic variability than calendering electrodes does. It could also be said that the electronic conductivity of films does not vary too significantly with porosity as the PSG model predicts.

The other set of electrodes was at triple the carbon and PVDF composition of the Saft electrodes. Three electrode films were produced all at the same porosity. Table 6.1 has the results from these measurements. More on how these values compare to the the PSG model electronic predictions is given in section 6.6.

6.5.3 Electronic measurements of simulated carbon domains

We found that carbon domain films were easier to work with due to their improved durability relative to the commercial LiCoO_2 composite films, possibly due to their having a higher mass fraction of PVDF. Outlined in Figure 6.7 are the electronic conductivity results for free-standing carbon films calculated from resistivities as shown in Figure 6.5. As the ratio of binder to carbon goes up, electronic conductivity changes slightly. This is likely because PVDF binder is basically non-conductive (10^{-13} S/cm [49]), and adding more PVDF would

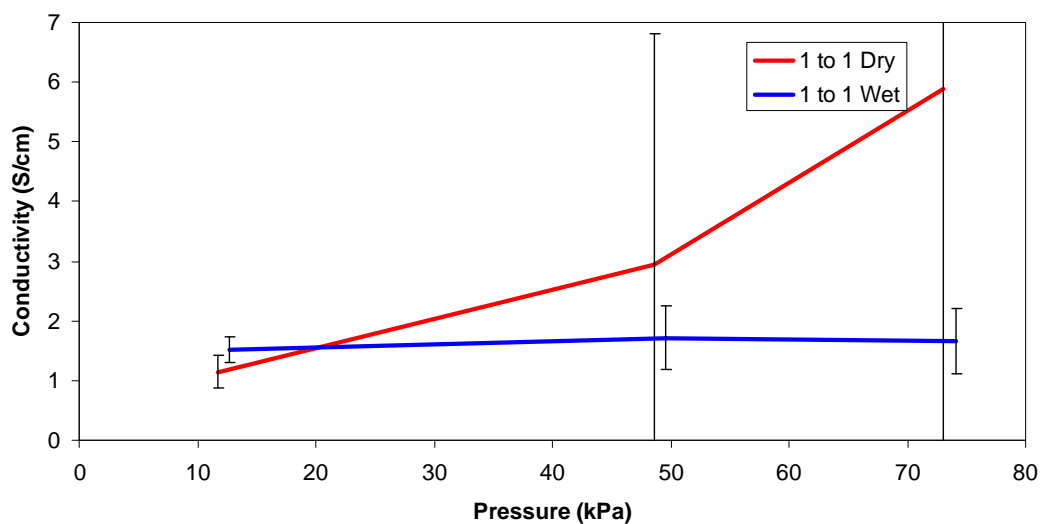
vary interparticle connections. Also of note is the dependence of conductivity on electrode pressure, which is greater than for LiCoO_2 films. For higher binder fractions, the pressure effect is stronger, with approximately a linear increase in conductivity for both wet and dry films versus pressure. For equal binder-to-carbon ratios, pressure did not really affect conductivity once electrolyte was added.

Prior work has been done by Battaglia and coworkers [99] to quantify carbon domain conductivities. They found with a four-point probe that wet conductivity was less than half that of dry conductivity, though it must be kept in mind that their experiments did not permit application of external pressure. We observed that wet conductivity was only significantly lower than dry at high pressures for 1:1 binder-to-carbon ratios. At higher binder-to-carbon ratios, the trend with pressure was similar for dry and wet films. We believe that how conductivity changes upon electrolyte addition depends on changes in carbon and active domain interactions. Currently we don't have a reliable way to image wet electrodes to fully study these effects.

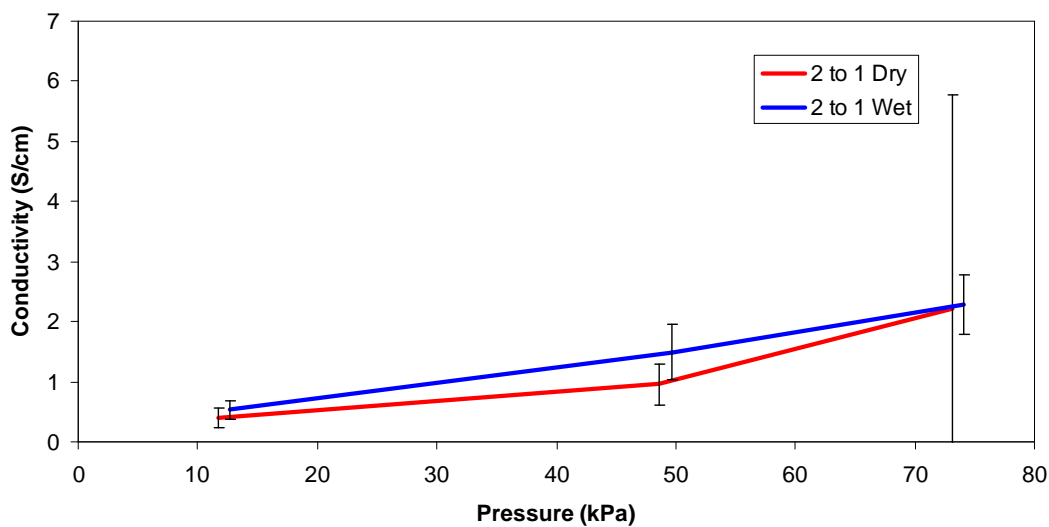
We found that with only one exception the probe contact resistances of carbon films were fairly uniform, within experimental uncertainties, regardless of pressure. The exception was the 2:1 dry carbon film in which the lowest-pressure apparent contact resistance was slightly negative. The contact resistances are plotted in Figure 6.8.

6.6 Comparing tangential probe measurements to PSG model results

PSG model results can be compared to the tangential probe method measurements of film conductivities. Of all the experiments, the tangential probe method best obtained film conductivities, which we judge to be the most reliable of the experimental methods though more on different experimental methods is presented later in this section. Comparisons

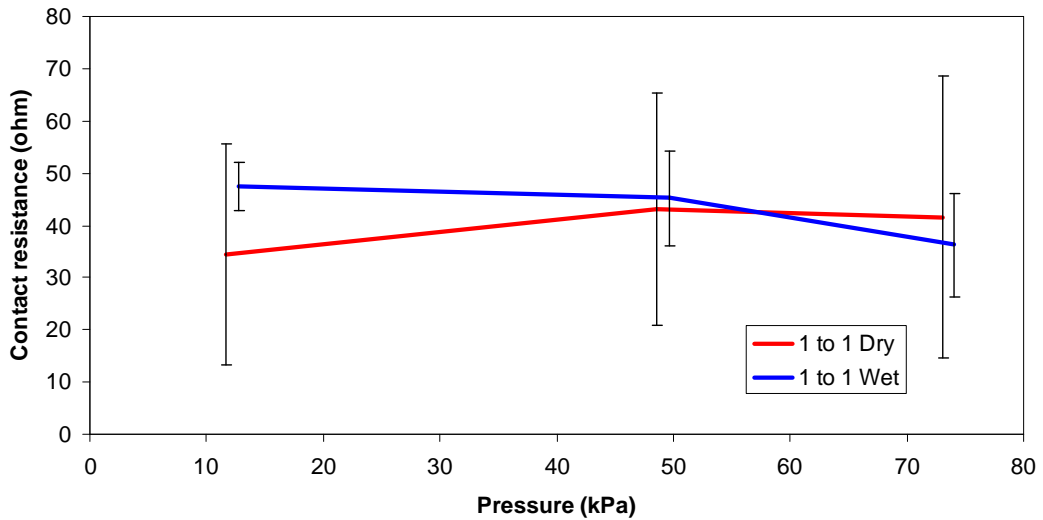


(a)

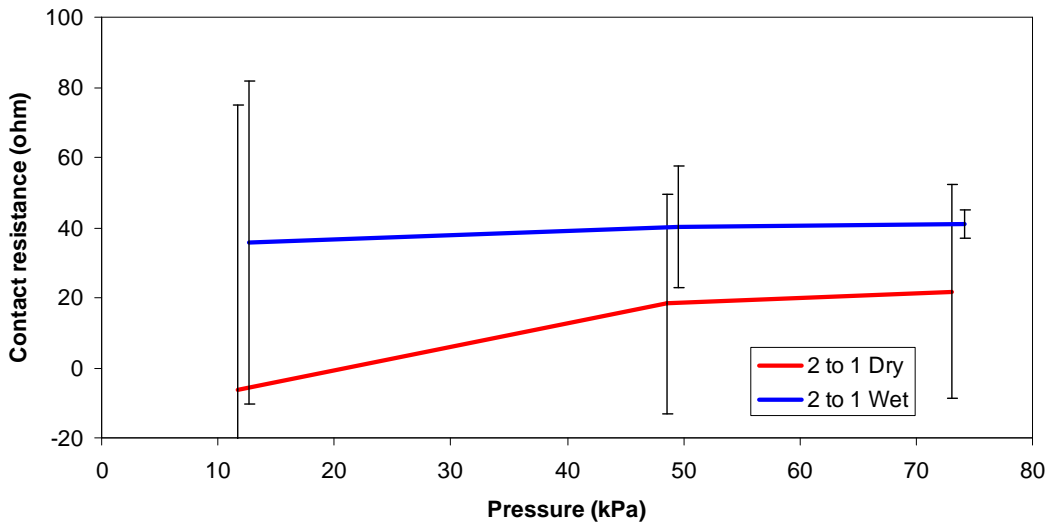


(b)

Figure 6.7: Electronic conductivity of free-standing carbon films at different binder-to-carbon ratios: a) 1:1 b) 2:1. Results are horizontally offset so that error bars can be clearly seen. Lines are added to guide the eye. Error bars represent the 95% confidence interval $n=8$.



(a)



(b)

Figure 6.8: Apparent contact resistances of free-standing carbon films at different external pressures and binder-to-carbon ratios: a) 1:1 and b) 2:1. Results are horizontally offset so that error bars can be clearly seen. Lines were added to guide the eye. Error bars represent the 95% confidence intervals $n=8$.

between the experiments and the PSG model results at this point require that the active material domain's conductivity be assumed. However, because the active material is not in sufficient quantity to create a percolation network even at the 34% porosity, it turns out that the majority of electrode conductivity depends on the carbon domain's conductivity. This is because the carbon provides the needed connections for a fully percolated network. As a result we tested how well the PSG model compares to the tangential probe measurements over extremes of possible active domain conductivities.

Experimental measurements of LiCoO_2 intrinsic conductivity were made at fully charged and discharged LiCoO_2 by Takahashi and coworkers [77]. As mentioned before, at fully charged or oxidized conditions $\sigma_a = 500 \text{ S/cm}$, and at discharged or reduced conditions $\sigma_a = 0.2 \text{ S/cm}$ [77]. Compressed pellets of LiCoO_2 particles have exhibited $\sigma = 0.00113 \text{ S/cm}$ [31]. Our own measurements of 81% LiCoO_2 and 19% PVDF films using the tangential probe measurement show conductivity to be $0.0014 \pm 0.0003 \text{ S/cm}$ with a 95% confidence, which is similar to the pelletized measurement. Differences between porous materials and intrinsic measurements suggests that contact resistances between LiCoO_2 particles is significant. The imaged active domain includes as well a small fraction of PVDF which means that the conductivity may not simply be the intrinsic active material conductivity. The active domain value may also include the effects of a possible coating of PVDF binder and/or carbon that may either improve or inhibit electron pathways in the active domains. For purposes of this work we are comparing the model to experiments using the intrinsic conductivities of LiCoO_2 as the basis of the active domain conductivity.

From the intrinsic conductivity values of LiCoO_2 and the electronic conductivity of carbon domains, we can obtain from the PSG model a range of electrode conductivities. Figure 6.9 compares the model predictions versus the experimental electrode conductivities. It can be seen that the PSG model not only follows the correct trends but it brackets the experimental results when the full range of possible intrinsic active domain conductivities is used. This

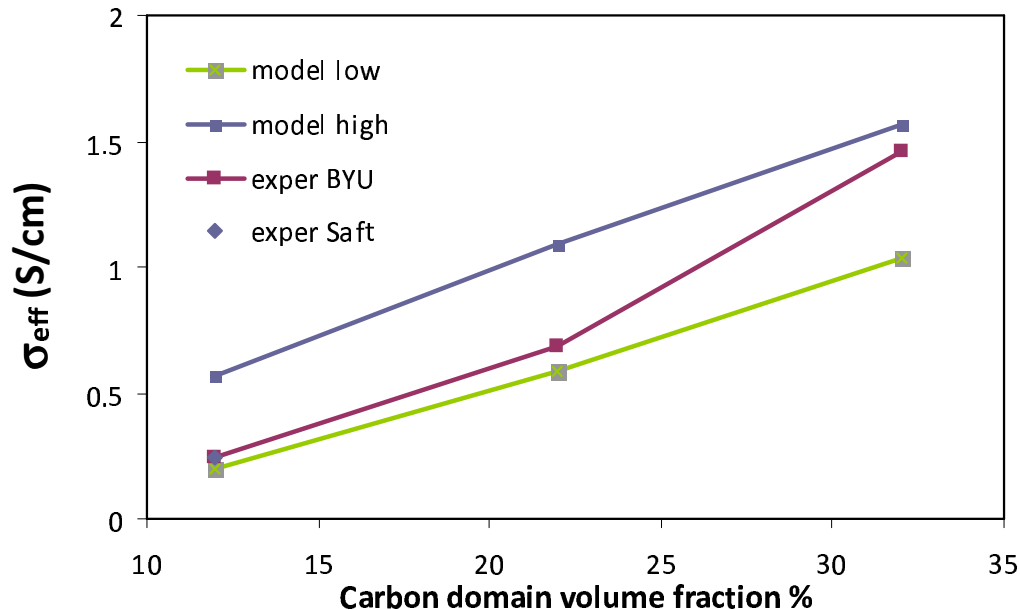


Figure 6.9: Experimental electrode conductivity over a range of carbon domain volume fractions as well as PSG model predictions. Model low is at active domains at 0.2 S/cm and the model high is with active domains at 500 S/cm. Lines are to guide to eye.

suggests that the PSG model could be used to predict with reasonable accuracy the effective electrode conductivities over a range of compositions and porosities.

As was shown earlier, the PSG model predicts that the ionic pathways within an electrode vary significantly with the carbon domain content. Polarization-relaxation experiments were done on the delaminated LiCoO_2 films in order to determine experimentally the ionic pathways within an electrode. Figure 6.10 shows the comparison between the model predictions versus the experimentally determined pathways. We see that the model has nearly quantitative agreement with experimental ionic transport values. It should be noted that the Saft or baseline electrodes had 11% carbon domain volume fraction that comes from only 2 wt% carbon. Electrodes in industry can be formulated with as much as 5 wt% carbon. These higher carbon weight percentages would correspond to model results for the carbon domain

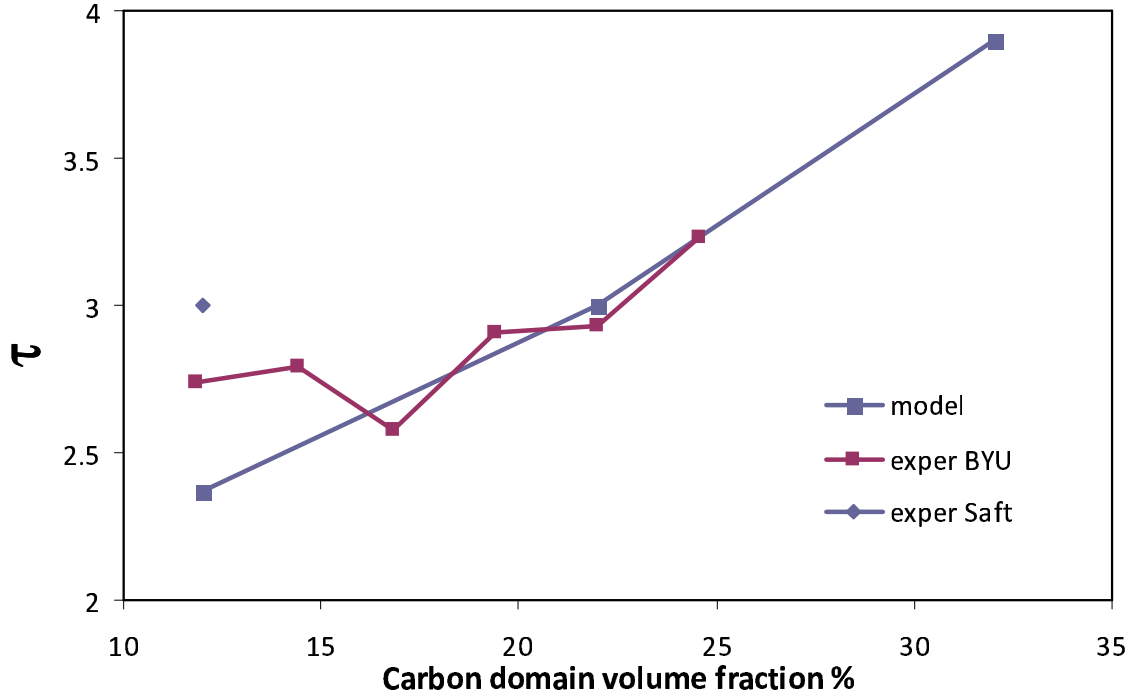


Figure 6.10: Experimental electrode ionic tortuosity versus the PSG model predictions. Lines are to guide the eye.

of 25 vol%. However, more image information needs to be done to verify that carbon domain volumes scale linearly with carbon and PVDF weight percentages.

6.7 Normal-direction AC impedance

The second method we employed was alternating current (AC) impedance to determine the electronic contact and intrinsic resistances simultaneously. AC impedance is a common technique used in the electrochemical community. Complex impedance, Z , is defined as:

$$Z = R + jX, \quad (6.3)$$

where R is the real part of the impedance and X is the imaginary part. In this work, we are most concerned with the real part of the impedance, which is related to both the contact and bulk resistances, and how these change with frequency.

The idealized circuit for a dry electrode film is shown in Figure 6.1 and has an overall impedance

$$Z_{\text{tot}} = \left(j\omega C + \frac{1}{R} \right)_{\text{con}}^{-1} + \left(j\omega C + \frac{1}{R} \right)_{\text{bulk}}^{-1}, \quad (6.4)$$

where ω is the frequency (rad/s), C is the capacitance, and R is the resistance. Subscript ‘con’ is for probe contact resistances, and subscript ‘bulk’ is for bulk resistances. As frequency is increased, the resistances of either the contact or intrinsic subcircuits or both are short circuited by the corresponding capacitance. This is illustrated in Figure 6.11 where there are distinct plateaus for the real part of the impedance. As frequency is increased, resistances decrease at different frequencies (assuming the time constant for the capacitance between the contact resistances and the bulk resistances are different).

Our experimental setup is as follows. For this work we used an Agilent 4924A Precision Impedance Analyzer. Multiple cell configurations were tried. The setup that was finalized is shown in Figure 6.12. A schematic representation of the apparatus is shown in Figure 6.13. It includes two machine-milled brass electrodes with banana clips and wires to electrically connect to the impedance analyzer. A polyethylene holder was constructed to allow for greater mechanical stability of the electrodes. Films were placed between the two electrodes with gravity providing a natural compressive force. Films attached to aluminum as well as delaminated films were both tested. The brass electrodes were 1.3 cm in diameter for a surface area of 1.327 cm^{-2} . The surfaces were sanded with fine sand paper after being machined. Varying weights were placed on top of the brass electrode for different experiments.

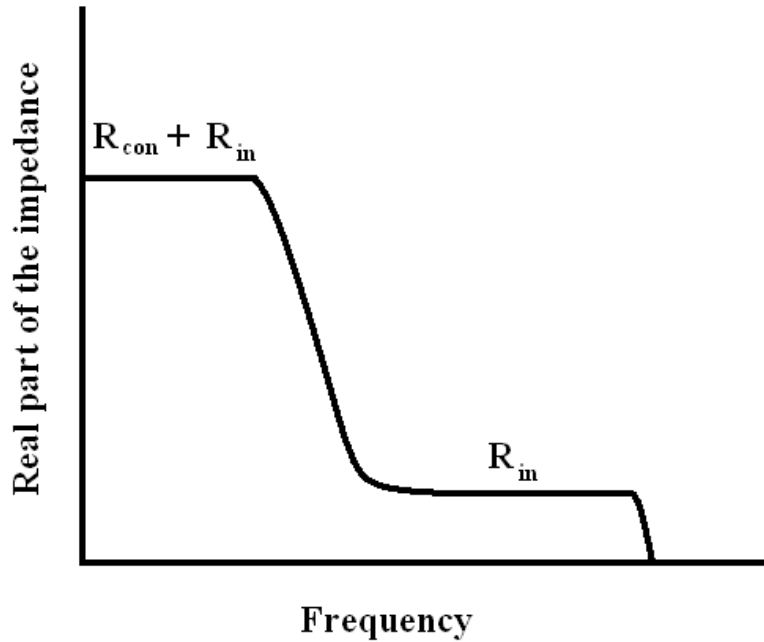


Figure 6.11: Idealized impedance circuit showing the real part of the impedance versus frequency. Distinct plateaus correspond to the resistances of the films.

6.7.1 Experiments

Several different experiments were conducted for different LiCoO_2 (Saft) and carbon films. The baseline AC test was with different films placed between the brass electrodes all at the same pressure. As a baseline in this test the aluminum foil current collector was measured without any films. In addition 2:1 binder-to-carbon ratios were tested as well as the four LiCoO_2 (Saft) films. Frequencies between 40 Hz to 110 MHz were tested at a pressure of 74 kPa. The goal of the baseline test was to observe how resistances changed with frequency and with electrode structure.

The pressure-dependence AC test was to test the 51% porosity Saft film at pressures ranging from 16 kPa to 164 kPa. The goal of the pressure-dependence test was to observe

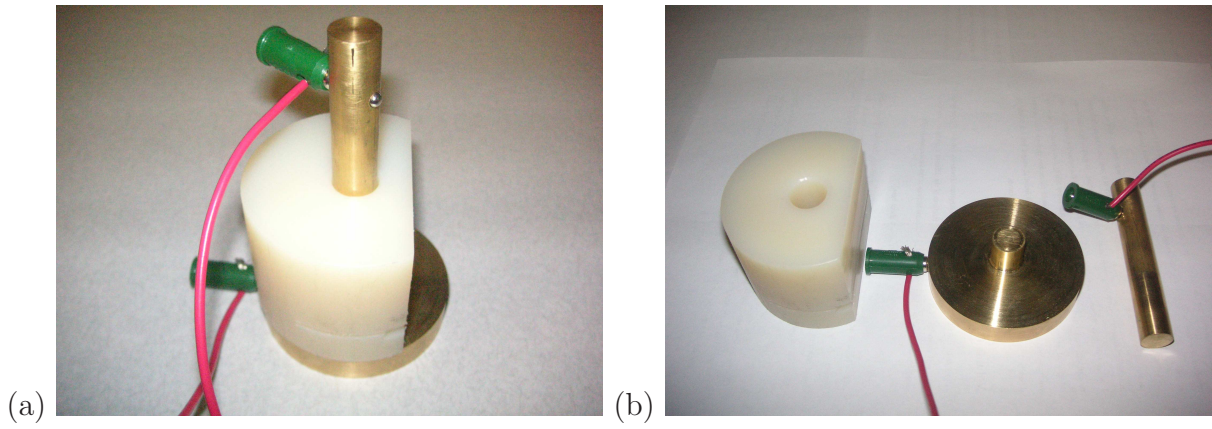


Figure 6.12: Images of experimental setup for AC experiment in a) assembled and b) disassembled states.

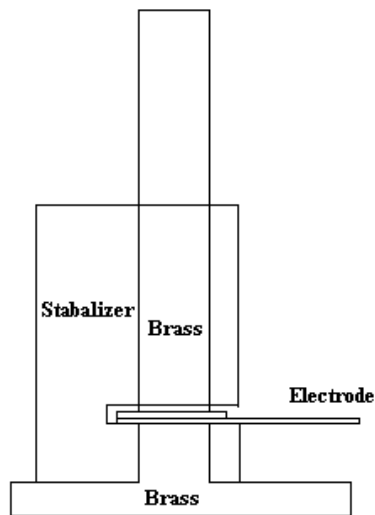


Figure 6.13: Schematic of experimental setup for AC experiment.

how resistances varied with pressure. One objective of this experiment was to evaluate whether or not the electrode contact resistances could be identified and perhaps minimized by changing the resistances with pressure.

The voltage-bias AC test applies voltage biases to the 51% porosity Saft film. The goal of the voltage-bias experiment was to verify that contact resistances were present in the system. A voltage bias can change the magnitude of contact resistances as will be explained in greater detail later.

6.7.2 Baseline AC test

Figure 6.14 shows the real part of the impedance observed from the AC impedance experiment versus the AC frequency. AC results are shown for 74 kPa of applied pressure for the cases of Saft films, 2:1 (63:37) binder-to-carbon film, and bare aluminum.

As can be seen in the results shown in Figure 6.14 both the bare aluminum and the 2:1 binder-to-carbon films exhibited similar low values of resistance (real impedance). From the tangential measurements in section 6.5, we expect cathode films in this geometry to have resistances on the order of 0.04 ohms. However, in these tests LiCoO_2 films exhibited much larger resistances. As frequency increased on the Saft electrodes, the measured resistances decreased. The low-frequency impedance values should include both contact resistances as well as bulk resistances. As frequency is increased, the capacitive nature of the different parts of the circuit short these resistances. It was hoped that there would be clear plateaus that would represent the resistances as is shown in Figure 6.11. The long-tail shape of the experimental results suggests that the actual electrode structures have a distribution of impedances more complex than that suggested in Figure 6.11. Furthermore, if the bulk and probe contact circuit elements have significant overlap in time constants, then it is difficult

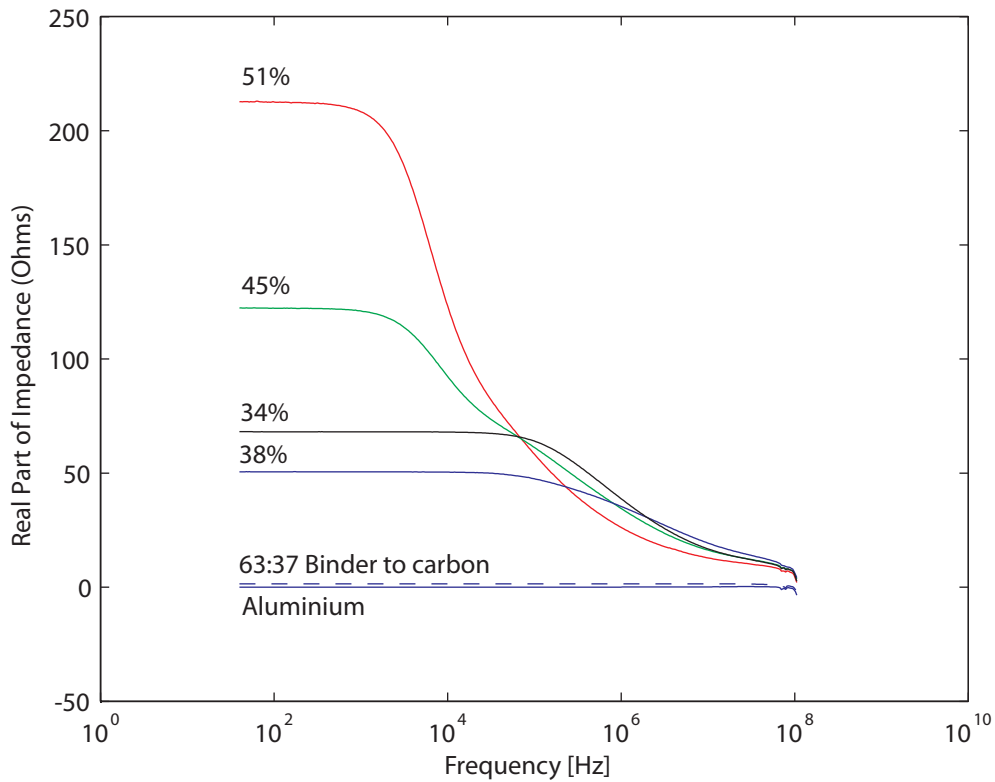


Figure 6.14: Real part of the impedance versus frequency. The delaminated binder/carbon film is only slightly above the bare aluminium.

to resolve the two elements separately as we wish. Thus, the bulk film resistances cannot be separated from the electrode contact resistances very well from this method.

At the very high frequencies, not shown in Figure 6.14, inductances in the wires and the electrodes become important. Inductance creates an impedance which is not related to the contact or intrinsic resistances but rather due to movement of electrons in the wires and current collectors. If inductance had not obscured the high-frequency data, we may have seen the resistances drop to zero as is shown in Figure 6.11 due to all circuits being short circuited at high frequencies.

One plateau did show up at low frequencies in our measurements, apparently corresponding to a combination of bulk and contact resistances. If probe contact resistances are small enough, then an accurate value of bulk conductivity can be obtained from this plateau. However, given that the thicknesses of the Saft films were between 37 and 70 μm , the bulk conductivity based on the plateaus in Figure 6.14 would be between 0.024 mS cm^{-1} and 0.084 mS cm^{-1} . Because these results are orders of magnitude lower than the pelletized LiCoO_2 with no carbon black additive, it is obvious that contact resistances are dominating the AC measurements. Because the tangential probe experiments showed 2:1 binder-to-carbon films had conductivities on the order of 2 S cm^{-1} , which is a much higher conductivity than the AC measurements, it is likely that electrode contact resistances in the AC setup were even larger than the bulk contact resistances. In order to better understand the nature and role of these electrode contact resistances, a couple of additional tests were done.

6.7.3 Pressure-dependence AC test

Probe contact resistances are dependent on the area of contact as well as the work function between materials [97]. The work function here could be thought of as the energy it takes to move electrons between materials. One test we performed was to change the pressure the sample was under in order to change the effective contact areas. For instance, changing pressure in pelletized samples has greatly affected the measured conductivity of carbon black as well as electrode mixtures [92, 93]. Figure 6.15 shows the 51% porosity Saft electrode evaluated at different pressures. The change in effective conductivity was nearly linear with pressure. Part of the measured pressure dependence may have been due to changing contact resistances between the brass electrodes and the film. With the planar probe method, intrinsic contact resistances changed linearly with pressure. Dependence on pressure of the normal AC impedance experiment followed the same linear trend.

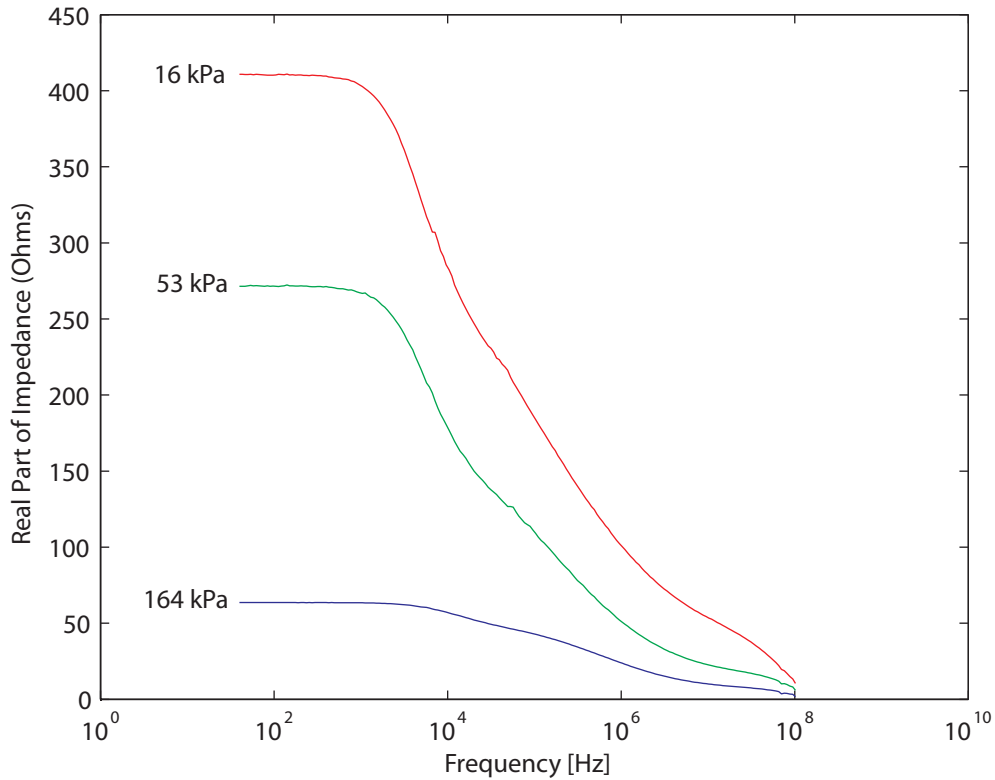


Figure 6.15: Real part of the impedance versus frequency for 51% porosity Saft electrode still attached to the aluminum current collector. Pressure was varied from 16 kPa to 164 kPa.

6.7.4 Voltage-bias AC test

Contact resistances depend not only on the area of the contact but also on the work function between materials. Schottky's model of contact resistances clarifies the relationship between contact resistance and work function [102]. According to this model, when electrons flow between two materials, an effective resistance occurs when there is a mismatch between the electron work functions of the two materials. When a potential difference is placed across the junction, it can counteract or bias the difference in work functions and modify (increase or decrease) the effective resistance in the same way that a diode has a nonlinear resistance.

Thus, we can probe whether contact resistance is due to the difference in work functions by varying in which direction and how strongly potential is used to drive current across the junction. Effectively this is done by adding a DC voltage bias on top of the AC current contact resistances. We tested this on the system in order to determine these types of contact resistances. Figure 6.16 shows the 51% porosity Saft electrode under 164 kPa of pressure with different voltage biases ranging from 0 to 200 mV. Noticeable differences in the resistance at low frequency can be seen, though it is not a dominant effect. At higher frequencies, these differences diminish leading us to conclude that the work function effects cannot explain all the problems in the measurement. We are left with the conclusion that the contact resistances are distributed with multiple time scales that likely overlap. What the actual effective intrinsic resistances are cannot be determined using the AC method directly.

6.8 Proof of concept for the thermal method

Because electronic measurements require a physical connection with the films, an unwanted connection resistance is generally measured with electrical probes. To ameliorate this problem, we explored the possibility of using an analogous measurement such as heat transport which then could be related to the electronic properties of the films. The advantage of using a heat transport measurement is the surface temperature of the films could be measured and averaged using an infrared camera. A camera does not require a physical connection with the material and thus eliminates a contact resistance. The heat flux at steady state could be solved using the SG model's structure and heat transport equations. Once the SG model was validated using heat fluxes, the electronic resistance could then be determined using the SG model rather than experiments. The tests done so far only are only able to show proof of concept, and further work is needed to develop this method into a practical technique.

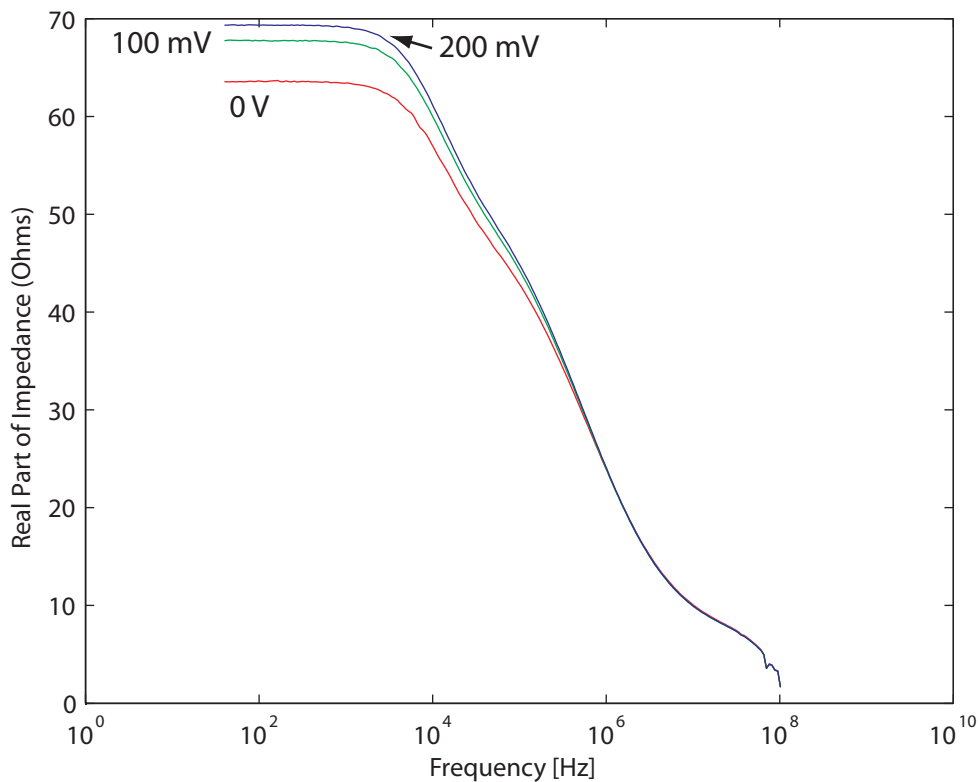


Figure 6.16: Real part of the impedance versus frequency for 51% porosity Saft electrode still attached to the aluminum current collector. Voltage bias is indicated next to each curve.

A preliminary experimental set up used in this work was a flat aluminum plate placed upon a hotplate. Images were taken with FLIR Therovision A20 camera and analyzed using the camera software. The software was able to average the temperature readings over an area. The four Saft films were placed on the hotplate and allowed to come to a pseudo steady state. However, because a hotplate was used in which the thermal element was turned on and off, there was a fluctuation of temperature in time. Figure 6.17 shows a thermal snapshot of the four Saft films on top of the aluminum plate.

The results from averaged measurements of the surface temperature of the films are graphed versus time in Figure 6.18. The temperature results show that the lower porosity

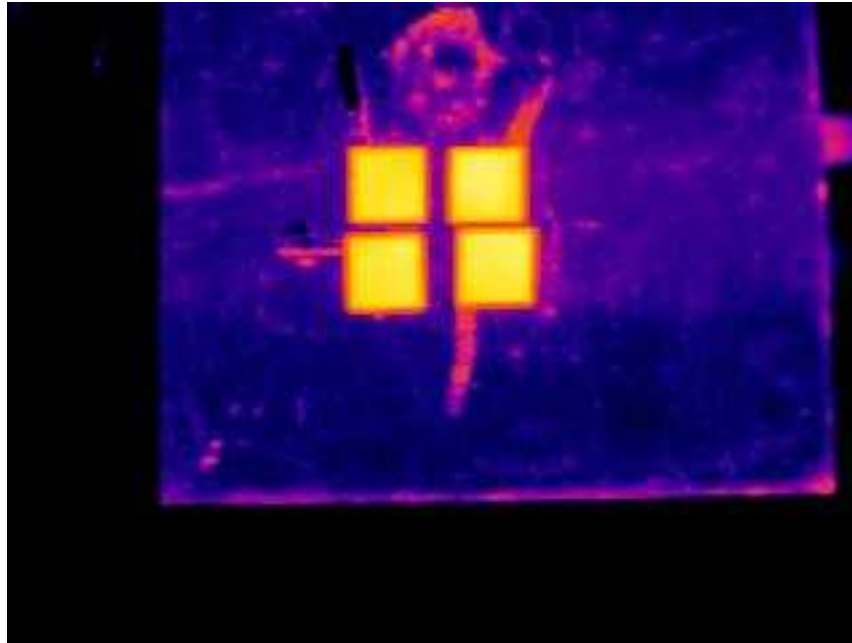


Figure 6.17: Hotplate with Saft films of the four porosities. The top right film is the Saft 34% porosity, the bottom right film is the Saft 38% porosity, the bottom left film is the Saft 45% porosity, and the top left film is the Saft 51% porosity.

LiCoO_2 films heat up faster than the higher porosity films, and heat to a higher temperature than the higher porosity films. This trend was expected because as porosity is decreased, heat transport (like electronic transport) should increase due to better interparticle connections. The higher the heat transport the greater the observed surface temperature of the film. So at least qualitatively we saw the expected variation in heat transfer properties with changing porosity.

In order to obtain quantitative electronic properties from the heat transport experiment the results need to be interpreted with the SG model. It would be best to modify the experiment so that it is at a steady state. The emissivity of the films should also be determined so that the actual temperature of the film surface can be measured, though the surfaces are likely to be well approximated as blackbody radiators. Also whatever heat source that is

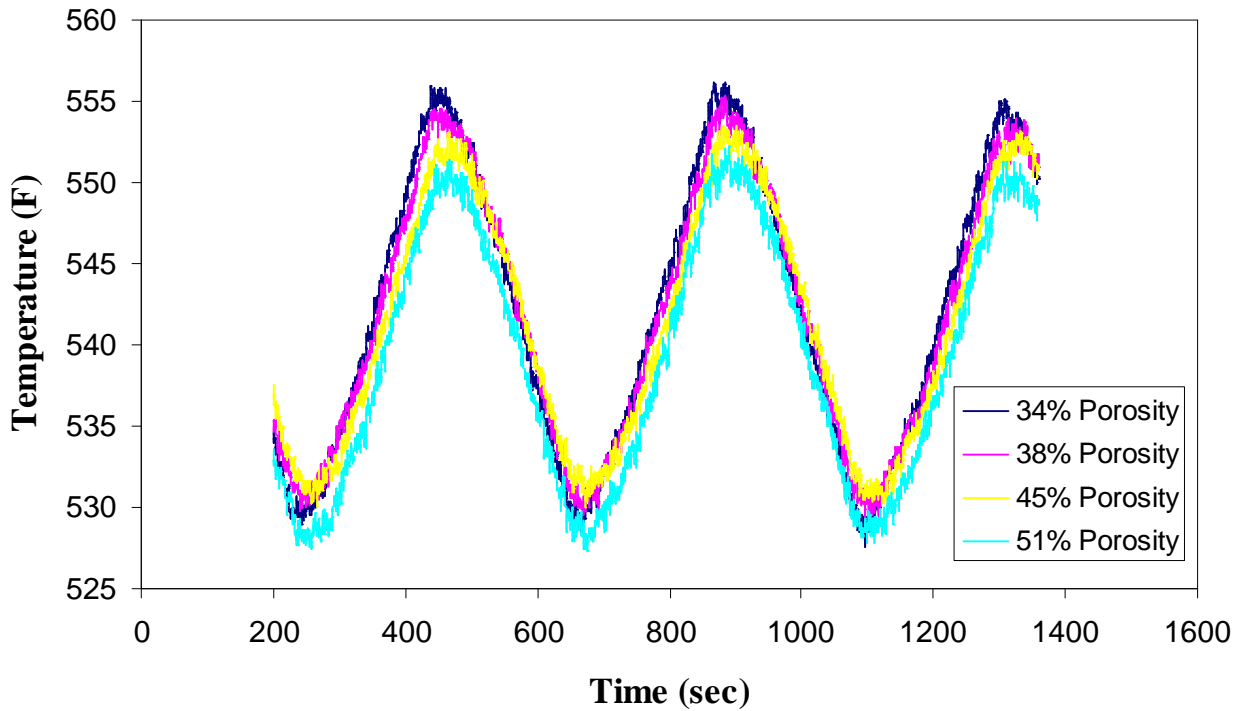


Figure 6.18: Simultaneous surface temperature results with the four porosities of Saft films heated on a hotplate at one temperature setting. Temperature results were obtained by assuming the surfaces were blackbody radiators.

used should have a known steady-state temperature. Measurements on different thickness films could facilitate validating the experiments and model.

6.9 Conclusions

Finding the intrinsic conductivity of electrodes is not a trivial problem due to probe contact resistances, surface roughness, and sample variations, even among commercially made electrodes. Contact resistances need to be eliminated or quantified in order to determine the intrinsic conductivity of electrodes. Because of the particulate nature of electrodes, the contact resistances between probe and particles cannot be eliminated in measurement tech-

niques. To match actual operating conditions, measurements should ideally be made for wet electrodes under pressure. Unfortunately this is incompatible with standard techniques such as the four-point probe. In addition, a non-destructive method of measuring film properties would be useful in industry for process control and development reasons.

The tangential probe electrode experiments provided a way (albeit a destructive way) to quantifiably apply a pressure and approximate the contact resistances between the flat electrodes and the films. The downside of the flat electrode experiment is that films needed to be delaminated. This created problems in determining both the dry and wet conductivities of Saft electrodes due to the brittleness of the delaminated electrodes.

The AC impedance experiment was a non-destructive method that also provided a way to quantifiably apply pressures. However, we could not eliminate the contact resistance between the electrodes and the films. Even though the films did not need to be delaminated, this method failed to yield accurate overall electrode conductivity.

The ability to measure the electronic properties of electrodes non-destructively continues to elude researchers. A technique that could do this would be very useful industrially as well as scientifically.

We were able using destructive measurement techniques to validate the model's ionic and electronic transport over a range of material volume fractions.

Chapter 7

Summary and scope for future work

Optimization of batteries for different applications requires an understanding of transport resistance trade-offs with material volume fractions as well as thickness of electrodes. In order to understand these trade-offs, our approach was to use a combination of model and experiments to find how changes in material volume fractions affect transport resistances. This project shows the beginnings of image analysis techniques and how it is possible to find overall electronic and ionic transport resistances from 3D structural reconstructions. The possible predictive abilities of our structural model gives hope for future electrochemical models to have fully predictive capabilities.

There were three major tasks associated with this work. Each is summarized and future directions discussed below.

7.1 FIB/SEM imaging and 3D structural reconstructions

FIB/SEM imaging was shown as a tool that could determine the essential structural features of LiCoO_2 cathodes, a model system. The existence of discrete porous carbon domains in the cathode microstructure was of major interest and is a new result in this field. Contact

probabilities between domains were used as the basis for 3D structural reconstructions. The discrete porous carbon domain ionic and electronic resistances were experimentally determined so that 3D structural reconstructions could be used to determine overall transport properties.

Two types of 3D models for correlating and predicting the electrode microstructure were explored. The first, known as the dynamic particle packing (DPP) model, is based on aggregates of spheres that move collectively in response to interparticle forces. The second is a stochastic grid (SG) model closely related to Monte Carlo techniques used in statistical physics to study cooperative and competitive phase behavior. The two models imitate the sub-micrometer-scale arrangement of active material particles, carbon, binder, and pores. The models use a small set of fundamental interdomain and bulk interaction parameters that were parametrized from 2D FIB/SEM cross sections, rather than from a full 3D reconstruction. The 3D structural reconstructions were best created using the interactions between different domains being described in terms of probabilities or energies. Probabilities or energies worked well with the Monte Carlo-type approach implemented in the SG model. Both models were able to semi-quantitatively reproduce experimental tortuosity measurements of cathodes at different porosity values.

Future prospects. In this work only a few FIB/SEM images were experimentally determined. As a result, the SG model was only parametrized with 2D FIB/SEM data. It has been shown in the literature and in this work that using only 2D data for 3D reconstructions causes an excessive aggregation of domains. This causes the 3D reconstructions to not precisely represent actual overall structures. With successive FIB/SEM images, 3D information can be obtained. With that information, particle-size statistics and shapes can be determined and implemented into the SG model using the so called C_2 statistics [73, 74]. The C_2 algorithm can be found from the work of Hoshen-Kopelman [74, 90] and modified to suit electrochemical systems.

7.2 3D Model predictions on the effects of structure and composition

We observed how probability of interactions between domains changed with material volume fractions, leading to empirical correlations. These correlations can be used in the SG model to reconstruct possible 3D structures at different material compositions.

From a combination of experimental measurements of carbon-film ionic and electronic conductivities and the PSG model, it is possible to predict semi-quantitatively the conductivities of electrode films at different compositions. We found that an optimum exists at which increasing the volume fraction of the carbon domain no longer increases the overall conductivity significantly. Using more carbon beyond the optimum only leads to marginal electronic improvement at the cost of increased ionic resistance, which in the extreme case leads to dominant ionic resistances. This decrease in effective ionic conductivity is due to very large tortuosity in the carbon domains.

Future prospects. Future work will need to incorporate a 3D electrochemical model which is based on the SG model's predicted structures and electrochemical equations in order to determine the effects of ionic and electronic transport resistance trade-offs have on electrode performance. This will be necessary in order to explore practical battery film designs that are tailored to specific battery applications.

One of the biggest questions left from this work is understanding how operating pressure changes structure. It is likely that pressure compacts the structure of an electrode effectively acting like calendaring. However, the effects of calendaring as shown by the PSG model in Figure 5.13 are not very pronounced unless the carbon domain conductivity is changed. In experimental measurements, increasing the pressure on the carbon domains caused a linear change in carbon domain conductivity. This in turn could have a significant effect on overall

conductivity. Being able to predict the optimal pressures for different electrode volume fractions would increase the practical uses of battery models.

7.3 Experimental determination of transport in films

Experiments were used to quantify the ionic and electronic pathways within simulated carbon domain agglomerates. We found that although these carbon domains are mostly porous, the ionic pathways through them are highly tortuous. This means carbon domains highly restrict ionic pathways within a cathode.

We found that experimentally determining carbon domain and electrode film electronic properties was not a trivial problem. A destructive experimental method was designed which we found produced the best overall electronic conductivity results for carbon films. From these electronic conductivity values and the 3D PSG model, overall electrochemical cell electronic properties can be estimated at given pressures. We found that electronic conductivity values of carbon domains vary significantly with fraction of PVDF binder. However, the changes that would occur to overall structure with varying PVDF fractions was not explored.

Future prospects. A non-destructive method for determining electronic conductivity of electrodes would be very helpful for industrial fabrication control processes. Also needed is a way to determine and eliminate probe contact resistances. Because bulk conductivity also depends on particle contact, a means to quantify these experimentally would also be useful in validating predictive 3D models such as our predict SG model.

Bibliography

- [1] Sheu, S., Yao, C. Y., Chen, J. M., and Chiou, Y. C. *J. Power Sources* **68**, 533–535 (1997).
- [2] Stephenson, D. E., Hartman, E. M., Harb, J. N., and Wheeler, D. R. *J. Electrochem. Soc.* **12**, 154 (2007).
- [3] Kaneko, M., Nakayama, M., and Masataka. *J. Solid State Electrochem.* **11**, 1071–1076 (2007).
- [4] Bernardi, D. M. and Go, J.-Y. *J. Power Sources* **196**, 412–427 (2011).
- [5] Newman, J. and Thomas-Alyea, K. E. *Electrochemical Systems*. John Wiley and Sons Inc. Publication, third edn edition, (2004).
- [6] Thomas, K. E., Darling, R. M., and Newman, J. Kluwer Academic/Plenum Publishers, (2002).
- [7] Thorat, I. V., Stephenson, D. E., Zacharias, N. A., Zaghbi, K., Harb, J. N., and Wheeler, D. R. *J. Power Sources* **188**, 592–600 March (2009).
- [8] Affanni, A., Belinni, A., Franceschini, G., Guglielmi, P., and Tassoni, C. *IEEE Transactions on Industrial Electronics* **52**(5), 1343–1349 October (2005).
- [9] Harb, J. N., LaFollette, R. M., Selfridge, R. H., and Howell, L. L. *Journal of Power Sources* **104**, 46–51 1 (2002).
- [10] Martin, T. L. and Siewiorek, D. P. *Wearable Computers* (1999).
- [11] Bauman, J. and Kazerani, M. *IEEE Transactions On Vehicular Technology* **57**(2), 760–769 3 (2008).
- [12] Liaw, B. Y., Jungst, R. G., Nagasubramanian, G., Case, H. L., and Doughty, D. H. *Journal of Power Sources* **140**, 157–161 1 (2005).
- [13] Arai, J., Yamaki, T., Yamauchi, S., Yuasa, T., Maeshima, T., Sakai, T., Koseki, M., and Horiba, T. *J. Power Sources* **146**, 788–792 (2005).

- [14] Kobayashi, H., Shikano, M., Koike, S., Sakaebe, H., and Tatsumi, K. *J. Power Sources* **174**, 380–386 12 (2007).
- [15] Choi, S. S. and Lim, H. S. *J. Power Sources* **111**, 130–136 (2002).
- [16] Vetter, J., Novak, P., Wagner, M. R., Veit, C., Moller, K. C., Besenhard, J. O., Winter, M., Wohlfahrt-Mehrens, M., Vogler, C., and Hammouche, A. *J. Power Sources* **147**, 269–281 (2005).
- [17] Kumai, K., Miyashiro, H., Kabayashi, Y., Takei, K., and Ishikawa, R. *J. Power Sources* **81-82**, 715–719 (1999).
- [18] Bay, S. D., Shapiro, D. G., and Langley, P. *Machine Learning: ECML 2002*. Springer Berlin / Heidelberg, (2002).
- [19] O’Sullivan, T. M., Bingham, C. M., and Clark, R. E. *SPEEDAM 2006* , S34–6–S34–11 (2006).
- [20] Reinhardt, W. L. *Ind. Eng. Chem.* **19**, 1124–1126 10 (1927).
- [21] Lovgren, J. G., Murdock, C. R., and Teofilo, V. L. *Energy Conversion Engineering Conference* 8 (1989).
- [22] Euler, K.-J. *J. Power Sources* **4**, 215–226 (1979).
- [23] Spotnitz, R. *J. Power Sources* **113**, 72–80 1 (2003).
- [24] Liaw, B. Y., Roth, E. P., Jungst, R. G., Nagasubramanian, G., Case, H. L., and Doughty, D. H. *J. Power Sources* , 874–886 6 (2003).
- [25] Mandal, S. *J. Electrochem Soc.* **A24**, 148 (2001).
- [26] Striebel, K. A., Sierra, A., Shim, J., Wang, C. W., and Sastry, A. M. *J. Power Sources* **241**, 134 (2004).
- [27] Gnanaraj, J. S., Cohen, Y. S., Levi, M. D., and Aurbach, D. *J. Electroanal. Chem.* **89**, 516 (2001).
- [28] Lin, Q. and Harb, J. *J. Electrochem. Soc.* **A1115**, 151 (2004).
- [29] Newman, J. and Tiedemann, W. *AIChE J.* **25**, 21 (1975).
- [30] Gummow, R. J., Thackeray, M. M., David, W. I. F., and Hull, S. *Materials Research Bulletin* **27**, 327–337 (1992).
- [31] Thomas, M., Bruce, P., and Goodenough, J. *Solid State Ionics* **18**, 794–8 (1986).

- [32] Yamada, A., Chung, S. C., and Hinokuma, K. *J. Electrochem. Soc.* **148**, A224–A229 (2001).
- [33] Delacourt, C., Poizot, P., Morcrette, M., Tarascon, J. M., and Masquelier, C. *Chem. Mater.* **16**, 93 (2004).
- [34] Delacourt, C., Poizot, P., Levasseur, S., and Masquelier, C. *Electrochem. Solid-State Lett.* **9**, A352–A355 (2006).
- [35] Hu, Y., Doeff, M. M., Kostecki, B. R., and Finones, R. *J. Electrochem. Soc.* **153**, A1279–A1285 (2006).
- [36] Doeff, M. M., Hu, Y., Mclarnon, F., and Kostecki, R. *Electrochem. Solid-State Lett.* **6**, A207–A209 (2003).
- [37] Huang, Y.-H., Park, K.-S., , and Goodenough, J. B. *J. Electrochem. Soc.* **9**, A2282–A2286 (2006).
- [38] Abraham, K. M. and Jiang, Z. *J. Electrochem. Soc.* **143**(1) 1 (1996).
- [39] Jeong, S. S., Lim, Y. T., Choi, Y. J., Cho, G. B., Kim, K. W., Ahn, H. J., and Cho, K. K. *J. Power Sources* **174**, 745–750 (2007).
- [40] Thackeray, M. M., Johnson, P. J., de Picciotto, L. A., Bruce, P. G., and Goodenough, J. B. *Materials Research Bulletin* **19**, 179–187 (1984).
- [41] Endo, M., Kim, C., Nishimura, K., Fujino, T., and Miyashita, K. *Carbon* **38**, 183–197 (2000).
- [42] Wilson, J. R., Kobsiriphat, W., Mendoza, R., Hsun-YiChen, Hiller, J. M., Miller, D. J., Thornton, K., Voorhees, P., Adler, S. B., and Barnett, S. A. *Nature Materials* **5**, 541–544 July (2006).
- [43] Shearing, P. R., Golbert, J., Chater, R. J., and Brandon, N. P. *Chem. Eng. Sci.* **64**, 3928–3933 (2009).
- [44] Harris, S. J. website, October (2010).
- [45] Lee, S.-Y., Kim, S. K., and Ahn, S. *J. Power Sources* **174**, 480–483 (2007).
- [46] Antolini, E., Giorgi, L., and Carewska, M. *J. Materials Science Letters* **18**, 325–327 (1999).
- [47] Li, Z., Zhang, D., and Yang, F. *J. Mater. Sci.* **44**, 2435–2443 (2009).
- [48] Mandal, S., Amarilla, J. M., Ibanez, J., and Rojo, J. M. *J. Electrochem. Soc.* **148**, A24–A29 (2001).

- [49] Ji, Y. and Jiang, Y. *Applied Physics Letters* **89**, 221103 (2006).
- [50] Feng, J. and Chan, C.-M. *Polymer Engineering and Science* **39**, 1207–1215 (1999).
- [51] Tizzani, C., Appetecchi, G. B., Carewska, M., Kim, G.-T., and Passerini, S. *Aust. J. Chem.* **60**, 47–50 (2007).
- [52] Doyle, M., Newman, J., Gozdz, A., Schmutz, C., and Tarascon, J.-M. *J. Electrochem. Soc.* **143**, 1890 (1996).
- [53] Nikolaidis, N. and Pitas, I. *3-D Image Processing Algorithms*. John Wiley and Sons, Inc., (2001).
- [54] Seul, M., O’Gorman, L., and Sammon, M. J. *Practical Algorithms for Image Analysis Description, Examples, and Code*. Cambridge University Press, (2000).
- [55] Wang, C.-W. and Sastry, A. M. *J. Electrochem. Soc.* **154**(11), A1035–A1047 (2007).
- [56] Wilson, J. R., Cronin, J. S., Barnett, S. A., and Harris, S. J. *J. Power Sources* **196**, 3443–3447 (2011).
- [57] Ender, M., Joos, J., Carraro, T., and Ivers-Tiffée, E. *Electrochemistry Communications* **13**, 166–168 (2011).
- [58] Russ, J. C. and Dehoff, R. T. *Practical Stereology*. Plenum Press, 2nd edition, (2001).
- [59] Torquato, S. *Random Heterogeneous Materials: Microstructure and Macroscopic Properties*. Springer-Verlag, New York, (2002).
- [60] Jiao, Y., Stillinger, F. H., and Torquato, S. *Phys. Rev. E* **82**, 011106 (2010).
- [61] Widom, B. *Statistical Mechanics: A Concise Introduction for Chemists*. Cambridge University Press, (2002).
- [62] Yeong, C. L. Y. and Torquato, S. *Physical Rev. E* **58**, 224–233 (1998).
- [63] Mandelbrot, B. B. *Science* **156**, 636–638 (1967).
- [64] Wang, C.-W. and Sastry, A. M. *J. Electrochem. Soc.* **154**(154), A1035–A1047 11 (2007).
- [65] Yi, Y. B., Wang, C. W., and Sastry, A. M. *Journal of Engineering Materials and Technology* **128**, 73–80 (2006).
- [66] Siddique, N. A. and Liu, F. *Electrochimica Acta* **55**, 5357–5366 (2010).
- [67] Smith, M., Garcia, R. E., and Horn, Q. C. *J. Electrochem. Soc.* **156**, A896–A904 (2009).

- [68] Frenkel, D. and Smit, B. *Understanding Molecular Simulation From Algorithms to Applications*. Academic Press, 2 edition, (2002).
- [69] Lennard-Jones, J. E. *Proc. R. Soc. Lond. A* **106**(738), 463–477 (1924).
- [70] von Solms, N., Koo, K. Y., and Chiew, Y. C. *Fluid Phase Equilibria* **180**, 71–85 (2001).
- [71] Brush, S. G. *Rev. Mod. Phys.* **39**, 883–893 (1967).
- [72] Schlick, T. *Molecular Modeling and Simulation*. Springer-Verlag, New York, (2002).
- [73] Jiao, Y., Stillinger, F. H., and Torquato, S. *Proc. Nat. Acad. Sci.* **106**, 17634 (2009).
- [74] Lee, S. B. and Torquato, S. *J. Chem. Phys.* **91**, 1173 (1989).
- [75] Wheeler, D. R. and Newman, J. *J. Phys. Chem. B* **108**, 18362–18367 (2004).
- [76] Park, M., Zhang, X., Cung, M., Less, G. B., and Sastry, A. M. *J. Power Sources* **195**, 7904–7929 (2010).
- [77] Takahashi, Y., Kijima, N., Tokiwa, K., Watanabe, T., and Akimoto, J. *J. Phys.: Condens. Matter* **19** (2007).
- [78] Carewska, M., Scaccia, S., Croce, F., Arumugam, S., Wang, Y., and Greenbaum, S. *Solid State Ionics* **93**, 227–237 (1997).
- [79] Ohzuku, T. and Ueda, A. *J. Electrochem. Soc.* **141**, 2973 (1994).
- [80] Li, C., Xu, X., and Wang, C. *J. Material Sci. Letters* **22**, 1183–1184 (2003).
- [81] Tukamoto, H. and West, A. R. *J. Electrochem. Soc.* **144**, 3164–3168 (1997).
- [82] Reimers, J. N. and Dahn, J. R. *J. Electrochem. Soc.* **139**, 2091–2097 (1992).
- [83] Inaba, M., Iriyama, Y., Ogumi, Z., Todzuka, Y., and Tasaka, A. .
- [84] Thorat, I. V. *Understanding performance-limiting mechanisms in Li-ion batteries for high-rate applications*. PhD thesis, Brigham Young University, (2009).
- [85] Zhang, Q., Guo, Q., and White, R. E. *J. Power Sources* **165**, 427–435 (2007).
- [86] Sheu, S. P., Yao, C. Y., Chen, J. M., and Chiou, Y. C. *Journal of Power Sources* **68**, 533–535 (1997).
- [87] Stux, A. M. and Swider-Lyons, K. E. *J. Electrochem. Soc.* **152**, A2009 (2005).
- [88] Stephenson, D. E. Master’s thesis, Brigham Young University, August (2008).
- [89] Kang, B. and Ceder, G. *Nature* **458**, 190–193 March (2009).

- [90] Hoshen, J. and Kopelman, R. *Phys. Rev. B.* **14**, 3438–3445 (1976).
- [91] Liu, G., Zheng, H., Kim, S., Deng, Y., Minor, A. M., Song, X., and Battaglia, V. S. *J. Electrochem. Soc.* **155**, A887–A892 12 (2008).
- [92] Palomares, V., Goni, A., de Muro, I. G., de Meatza, I., Bengoechea, M., Cantero, I., and Rojo, T. *J. Power Sources* **195**(195), 7661–7668 (2010).
- [93] Sphar, M. E., Goers, D., Leone, A., Stallone, S., and Grivei, E. *J. Power Sources* **196**, 3404–3413 (2011).
- [94] Cutnell, J. D. and Johnson, K. W. *Resistivity of Various Materials in Physics*. Wiley, New York, (2004).
- [95] Coroce, F., Eifanio, A. D., Hassoun, J., Deptula, A., Olczac, T., and Scrosati, B. *Electrochem. Solid-State Lett.* **5**, A47–A50 (2002).
- [96] Wang, C. W., Sastry, A. M., Striebel, K. A., and Zaghib, K. *J. Electrochem. Soc.* **152**, A1001–A1010 (2005).
- [97] Schroder, D. K. *Semiconductor Material and Device Characterization*. John Wiley & Sons, New York, 2 edition, (1998).
- [98] Wang, C. W., Cook, K. A., and Sastry, A. M. *J. Electrochem. Soc.* **150**, A385–A397 3 (2003).
- [99] Liu, G., Zheng, H., Simens, A. S., Minor, A. M., Song, X., and Battaglia, V. S. *J. Electrochem. Soc.* **154**, A1129–A1134 12 (2007).
- [100] Chen, Z., Christensen, L., and Dahn, J. R. *J. Electrochem. Soc.* **150**, A1073 (2003).
- [101] Saunier, J., Alloin, F., Sanchez, J. Y., and Barriere, B. *J. Polymer Sci. Part B: Polymer Physics* **42**, 532–543 (2004).
- [102] Schroder, D. K. *Semiconductor Material and Device Characterization*. John Wiley and Sons, 2 edition, (1998).

Appendix A. DPP model code

Input file for the DPP model which was programmed in Fortran 77.

1.0 :dimensionless temperature

1.2 :dimensionless density

0.0000005 :dimensionless time-step

0.1 :dimensionless tau of real particles (usually around $50*dt$)

0.1 :dimensionless tau of flotsam particles

10 :dimensionless lamda of ghost particles

2.5 :dimensionless cutoff length (usually around 2.5)

10000 :number of timesteps per block

1 :number of blocks

2 :number of blocks to discard

1 :.xyz file output (0=no, 1=yes)

0 :tethering (0=no, 1=yes)

3.0 :tethering constant

50 :number of timesteps between samples

50 :number of timesteps between .xyz file output

0.7 :dimentionless fcut for flotsam potential

50 :flotsam force at $r=0$

DPP model main code

```
*23456789012345678901234567890123456789012345678901234567890123456789012
PROGRAM DPd2
! nn=number of particles (carbon and active) per dimension
! nd=number of dimensions
! n=total number of real particles (carbon and active)
! nc=number of carbon particles
! maxbin=# of bins for histograms
Parameter (nn=10,nd=3,maxbin=30000,nc=275) !Input Parameters
Parameter (n=(nn**nd),ng=(nn-1)**nd) !Number of real and flotsam particles
integer nn,nd,tsblk,nblk,i,j,k,ii,jj,numf(maxbin),ng,kkk,
1 ct,nt,ntu,ts,n,txyz,
2 tsam,numw(maxbin),numd(maxbin),
3 numt(maxbin),nums(maxbin)
real*8 v(3,n),rp,dt,dt2,
1 x(5,n),a(3,n),L,ke,virial,xnew(3),pe,pet,
2 rho,vol,tdes,pvt,tt,umax,umin,eu,
3 xg(3,ng),vg(3,ng),ag(3,ng),uadd(ng),
4 tempg,keg,xt(3,ng),ke2,eutot,euf,uxces,uxcesb,
5 ut(ng),us(ng),
6 uxcesuc,pi,utail,rcut,rcut2,
7 Fint(3,n),Fgint(3,ng),lam,tau,lamg,temp,keg2,ttg,
8 uw(ng),ud(n),uwmax,uwmin,udmax,udmin,euw,eud,
9 uxcesw,uxcesd,At,rf(ng,n),rw(ng,n),rd(n,n),
1 numrf(maxbin),numrw(maxbin),numrd(maxbin),
2 CC,fcut,utmin,utmax,sigdist(n),epsdist(n),
3 usmin,usmax,uxcesf,taug
logical xyzbol,sbol,tbol
character(2) pname !name of particle
character(4) stopme
Data nt/0/,pvt/0.d0/,tt/0.d0/,pet/0.d0/,ts/0/
Data eu/0.d0/,ntu/0/,ke2/0.d0/,ke/0.d0/,keg/0.d0/
Data eutot/0.d0/,euf/0.d0/,umax/0.d0/,umin/0.d0/
Data utmax/0.d0/,utmin/0.d0/,ufmax/0.d0/,ufmin/0.d0/
Data uwmax/0.d0/,uwmin/0.d0/,udmax/0.d0/,udmin/0.d0/
Data utmax/0.d0/,utmin/0.d0/,usmax/0.d0/,usmin/0.d0/
Data eus/0.d0/,euus/0.d0/,lam/0.d0/,fcnt/0/,fcnt2/0/
Data keg2/0.d0/,ttg/0.d0/,euw/0.d0/,eud/0.d0/
Data sbol/.false./
!Data output
Open(12,FILE='output.txt')
Rewind(12)
```

```

!Stops code at the end of the current block—change to "true" to stop
Open(15,FILE='stopmenow.txt')
rewind(15)
Write(15,*) 'false'
close(15)
!Reads in variables from input.txt
call input(tdes,rho,dt,tau,lamg,At,fcut,tsblk,nblk,ct,
1 xyzbol,tbol,tsam,CC,rcut,txyz,taug)
!Zero variables
do i=1,ng
uadd(i)=0.d0
uw(i)=0.d0
ut(i)=0.d0
us(i)=0.d0
enddo
do i=1,n
do k=1,nd
Fint(k,i)=0.d0
enddo
enddo
do i=1,ng
do k=1,nd
Fgint(k,i)=0.d0
enddo
enddo
do i=1,maxbin
numf(i)=0
numw(i)=0
numd(i)=0
enddo
pname='H ' !Name of particle (controls size of visualization in VMD)
!Error trap—wrong number of dimensions (must be 2 or 3)
If ((nd.gt.3) .or. (nd.lt.2)) then
Print *, 'Error: only 2 or 3 dimensions allowed'
stop
endif
!Output number of molecules to output.txt
Print *, 'You have selected: '
Print *, " ",n,' total molecules.'
vol=n/rho !system volume
L=vol**(1.d0/nd) !system length
Print *, "L=",L !Output length to output.txt

```

```

rp=0.71 !radius of particles—used to position molecules in cold start
dt2=dt*dt !timestep squared
ct=ct*tsblk !total number of timesteps to discard at the beginning
!calculate long range correction of potential
rcut2=rcut*rcut
pi=3.14159265
utail=(-16.d0/9.d0)*pi*rho*((3.d0*(rcut**6)-1.d0)
1 /(rcut**9.d0))
utail=0.d0 !I haven't got this working yet, so set utail equal to 0
call initial(v,nn,n,x,L,nd,rp,tdes,nc) !Positions real particles and starts them moving
call accel(n,nd,a,x,L,pe,virial,rcut2,Fint,ud,sbol,ts,utail, !Calculates the accelertion of real
particles
1 rd,fcut,rcut,v,tdes,nc)
!Diagnostic to make sure the code is working
Print *, 'x1=',x(1,1),x(2,1)
Print *, 'v1=',v(1,1),v(2,1)
Print *, 'a1=',a(1,1),a(2,1)
if (xyzbol) then !Output positions for visualization in VMD
OPEN(1,FILE='real.xyz')
Rewind (1)
C C C———Print out positions———
205 format (I5,A)
305 format (F6.0,A)
405 format (A2,2x,3F10.4,A)
Write(1,205) n, char(13)
Write(1,305) 0.0,char(13)
do kkk=1,n
pname='H+'
if (x(4,kkk).lt.0.6) then
pname='H'
endif
if (nd.eq.3) then
Write(1,405)
1 pname,x(1,kkk)*2,x(2,kkk)*2,x(3,kkk)*2,char(13)
elseif (nd.eq.2) then
Write(1,405)
1 pname,x(1,kkk),x(2,kkk),0.0000,char(13)
endif
enddo
endif
C***** main loop to move particles *****
virial=0.0 !pressure accumulator

```

```

pe=0.0 !potential energy accumulator
do i=1,nblk !number of blocks
do j=1,tsblk !number of timesteps per block
ts=ts+1 !timestep counter
c if (ts.le.500) then !Output timestep to make sure code hasn't crashed
c Print *, "
Print *, ts
c Print *, "
c endif
if (mod(ts,tsam).eq.0) then !Sample and record energies, etc.
sbol=.true.
else
sbol=.false.
endif
call move (n,nd,dt,dt2,x,v,a,L,ke,virial,xnew,pe, !move real particles
1 rcut2,Fint,ud,sbol,ts,utail,rd,
2 fcut,rcut,tdes)
!Nose-Hoover thermostat for real particles
ke=ke/n
temp=2.d0*ke/nd
lam=lam+dt*(temp-tdes)/(tdes*tau)
do ii=1,n
do jj=1,nd
Fint(jj,ii)=lam*v(jj,ii)
enddo
enddo
ke2=ke2+ke*n
ke=0.d0
if (mod(ts,txyz).eq.0) then !print out positions
if (xyzbol) then
ts2=(ts/txzy)
Write(1,205) n, char(13)
Write(1,305) ts2,char(13)
do kkk=1,n !Real particles
pname='H+'
if (x(4,kkk).lt.0.6) then
pname='H'
endif
if (nd.eq.3) then
Write(1,405) pname,x(1,kkk)*2,
1 x(2,kkk)*2,x(3,kkk)*2,char(13) !3-D representation
elseif (nd.eq.2) then

```

```

Write(1,405) pname,x(1,kkk),
1 x(2,kkk),0.0000,char(13) !2-D representation
endif
enddo
endif
endif
call comsol(x,n,rp,L,nc)
enddo
!***** End of Block *****
c call comsol(x,n,rp,L,nc)
call final(tsbk,ke2,pe,n,nd,L,virial,ts,dt,v,tdes,pvt,nt, !Calculate properties like pressure,
pot. energy, etc.
1 tt,ct,pet,vg,ng,tsam,keg2,ttg)
Open(15,FILE='stopmenow.txt') !Check to see if the code should stop from stopfile
Rewind(15)
Read(15,*) stopme
If (stopme.eq.'true') then !Stop
Print *, "
Print *, 'File stopped by stopfile.'
Print *, "
GOTO 101 !Not sure how else to break out of the loop...
Close(15)
endif
Close(15)
enddo
***** End of Main Loop *****
101 if (xyzbol) then
Close(1)
Close(2)
endif
Print *, "
Print *, 'Average Temperature=',tt/(nt)
Print *, 'Average Pressure=',(pvt/(nt))
Print *, 'Average PE=', pet/(nt)
end
C*****
subroutine initial(v,nn,n,x,L,nd,rp,tdes,nc)
real*8 vmax,v(3,n),rp,eps,sig,
1 x(5,n), Rnum,L,ke,temp,tdes,gauss,gauss2
integer n,nn,nd,i,j,k,particle,IRR,nc,nnc,
1 scram(n),nlats,particle2,I1,I2,IT,j1,j2
real*8 vcum(3),dL,sigdist(n),epsdist(n)

```

```

Data IRR/10105/,vmax/1.d0/,ke/0.d0/
nnc=n-nc
Do i=1,3
vcum(i)=0
enddo
dL=L/nn
particle=0
C Input the sigmas eps of the system
do i=1,n-nc
sigdist(i)=0.01d0
do while (sigdist(i).lt.0.1d0)
call RANDNUM(IRR,Rnum)
rn1=Rnum
call RANDNUM(IRR,Rnum)
rn2=Rnum
gauss=sqrt(-2.d0*log(rn1))*cos(6.283185306d0*rn2)
gauss2=sqrt(-2.d0*log(rn1))*sin(6.283185306d0*rn2)
sigdist(i)=exp(-2.30+1.8*gauss)
do while (sigdist(i).gt.2.30d0)
sigdist(i)=2.29d0
enddo
epsdist(i)=100.d0
epsdist(i)=1+epsdist(i)**1+((sigdist(i)-0.2d0)**3)*
1 ((2.3d0-sigdist(i))**2)*0
enddo
enddo
do i=n-nc+1,n
sigdist(i)=0.01d0
do while (sigdist(i).lt.0.1d0)
call RANDNUM(IRR,Rnum)
rn1=Rnum
call RANDNUM(IRR,Rnum)
rn2=Rnum
gauss=sqrt(-2.d0*log(rn1))*cos(6.283185306d0*rn2)
gauss2=sqrt(-2.d0*log(rn1))*sin(6.283185306d0*rn2)
sigdist(i)=exp(-2.30+1.7*gauss)
do while (sigdist(i).gt.2.30d0)
sigdist(i)=2.29d0
enddo
epsdist(i)=100.d0
epsdist(i)=1+epsdist(i)**1+((sigdist(i)-0.2d0)**3)*
1 ((2.0d0-sigdist(i))**2)*0

```



```

enddo
enddo
do j2=1,n
c write(6,*) 'scram,j2=',scram(j2),' ',j2
scram(j2)=j2
enddo
nlats=nn*nn*nn
do j1 = 1, 20*nlats
CALL RANDNUM(IRR,Rnum) !FIND A RANDOM LATTICE SLOT
I1 = INT(Rnum*FLOAT(nlats))+1
CALL RANDNUM(IRR,Rnum) !FIND ANOTHER ONE
I2 = INT(Rnum*FLOAT(nlats))+1
IT = scram(I2) !SWAP OCCUPANTS OF TWO SLOTS
scram(I2) = scram(I1)
scram(I1) = IT
enddo
do i=1,nn
do j=1,nn
do k=1,nn
particle=particle+1
particle2=scram(particle)
sig=sigdist(particle2)
eps=epsdist(particle2)
x(1,particle2)=(i)*dL
x(2,particle2)=(j)*dL
x(3,particle2)=(k)*dL
x(4,particle2)=sig
x(5,particle2)=eps
enddo
enddo
enddo
do k=1,nd
do particle=1,n
call RANDNUM(IRR,Rnum)
v(k,particle)=vmax*(2.d0*Rnum-1.d0)
vcum(k)=vcum(k)+v(k,particle)
enddo
!normalize velocities
vcum(k)=vcum(k)/n
do particle=1,n
v(k,particle)=v(k,particle)-vcum(k)
enddo

```

```

enddo
do i=1,n
do k=1,nd
ke=ke+0.5*v(k,i)*v(k,i)
enddo
enddo
ke=ke/n
temp=2.d0*ke/nd
do i=1,n
do k=1,nd
!scale velocities to get the correct temperature
v(k,i)=v(k,i)*sqrt(tdes/temp)
enddo
enddo
return
end
C*****
subroutine accel(n,nd,a,x,L,pe,virial,rcut2,Fint,ud,sbol,ts,utail,
1 rd,fcut,rcut,v,tdes,nc)
real*8 x(5,n),v(3,n),a(3,n),L,virial,pe,rn1,rn2,sig,
1 dx(3),sgndx,r2,r,force,potential,dxk,rnum,eps,
2 rcut2,Fint(3,n),ud(n),utail,rd(n,n),fcut,fcut2,
3 vij(3),vr,vrhat,rcut,vijk,xhat,tdes,gauss,gauss2
4 kij
integer n,nd,i,k,molec,neighbor,ts,IRR,Rnumtest,nc
logical sbol
Data IRR/10105/
do i=1,n
do k=1,nd
a(k,i)=0.d0
enddo
enddo
fcut2=fcut**2.d0
do molec=1,n-1
do neighbor=molec+1,n
r2=0
vr=0.d0
Rnumtest=0
do k=1,nd
dx(k)=x(k,molec)-x(k,neighbor)
dx(k)=dx(k)-L*nint(dx(k)/L)
r2=r2+dx(k)*dx(k)

```

```

vij(k)=v(k,molec)-v(k,neighbor)
vr=vr+vij(k)*dx(k)
if (sbol) then
r=sqrt(r2)
if (.not.(molec.eq.neighbor)) then
rd(molec,neighbor)=r
rd(neighbor,molec)=r
endif
endif
enddo
if (r2.lt.(rcut2)) then !truncate LJ potential
sig=0.5*(x(4,molec)+x(4,neighbor))
kij=1-((x(4,molec)+x(4,neighbor))*(x(4,molec)
1 +x(4,neighbor))/(4*x(4,molec)*x(4,neighbor)))*0+1
eps=sqrt(x(5,molec)*x(5,neighbor))*((kij))
r=sqrt(r2)
vrhat=vr/r
do k=1,nd
vijk=vij(k)
dxk=dx(k)
xhat=dxk/r
if (Rnumtest.eq.0) then
call RANDNUM(IRR,Rnum)
rn1=Rnum
call RANDNUM(IRR,Rnum)
rn2=Rnum
Rnumtest=1
gauss=sqrt(-2.d0*log(rn1))*cos(6.283185306d0*rn2)
gauss2=sqrt(-2.d0*log(rn1))*sin(6.283185306d0*rn2)
else Rnumtest=0
endif
call LJ(r,force,potential,dxk,rcut,vijk,
1 vrhat,xhat,tdes,gauss,sig,eps)
a(k,molec)=a(k,molec)+(force)*x(4,molec)
1 *x(4,molec)*dxk/(r)
a(k,neighbor)=a(k,neighbor)-(force)
1 *x(4,molec)*x(4,molec)*dxk/(r)
virial=virial+force*x(4,molec)
1 *x(4,molec)*dxk
gauss=gauss2
enddo
pe=pe+potential

```

```

If(sbol) then
!Print *, r
!Print *, r
ud(molec)=ud(molec)+potential
ud(neighbor)=ud(neighbor)+potential
endif
endif
enddo
enddo
!thermostat for real particles
do i=1,n
do k=1,nd
a(k,i)=a(k,i)-Fint(k,i)
enddo
enddo
return
end
d
C*****
subroutine periodic(nd,xnew,L,k)
real*8 L,xnew(3)
integer nd,i,j,k
do while (xnew(k).lt.0)
xnew(k)=xnew(k)+L
enddo
do while (xnew(k).gt.L)
xnew(k)=xnew(k)-L
enddo
return
end
C*****
subroutine move (n,nd,dt,dt2,x,v,a,L,ke,virial,xnew,pe,
1 rcut2,Fint,ud,sbol,ts,utail,rd,
2 fcut,rcut,tdes)
real*8 v(3,n),dt,dt2,pe,ud(n),rcut,tdes,
1 x(5,n),a(3,n),L,ke,virial,xnew(3),
2 rcut2,Fint(3,n),utail,rd(n,n),fcut
integer n,nd,i,k,ts
logical sbol
do i=1,n
do k=1,nd
xnew(k)=x(k,i)+v(k,i)*dt+a(k,i)*dt2/2.d0

```

```

call periodic(nd,xnew,L,k)
x(k,i)=xnew(k)
v(k,i)=v(k,i)+a(k,i)*dt/2.d0 !Half update velocity
enddo
enddo
call accel(n,nd,a,x,L,pe, virial,rcut2,Fint,ud,sbol,ts,utail,
1 rd,fcut,rcut,v,tdes,nc)
do i=1,n
do k=1,nd
v(k,i)=v(k,i)+a(k,i)*dt/2
ke=ke+0.5*(v(k,i)*v(k,i))
enddo
enddo
return
end
C*****
subroutine final(tsblk,ke2,pe,n,nd,L, virial,ts,dt,v,tdes,pvt,nt,
1 tt,ct,pet,vg,ng,tsam,keg2,ttg)
real*8 dt,v(3,n),tdes,tt,pet,e,
1 L,ke2, virial,pe,pvirial,pvt,vg(3,ng),tempg,
2 temp,ttg,keg2
integer n,nd,ng,ts,nt,ct,tsam,tsblk
ke2=ke2/(tsblk*n)
keg2=keg2/(tsblk*ng)
pe=pe/(tsblk*n)
e=ke2+pe
temp=2.d0*ke2/nd
tempg=2.d0*keg2/nd
pvirial=n*temp/(L**nd)+virial/(nd*(L**nd)*tsblk)
If (ts.gt.ct) then
nt=nt+1
pvt=pvt+pvirial
tt=tt+temp
ttg=ttg+tempg
pet=pet+pe
endif
If (mod(ts,10000).eq.0) then
Print *, "
Print *, ts
Print *, ' KE=',ke2
Print *, ' PE=',pe
Print *, ' E=',e

```

```

Print *, ' P=',pvirial
Print *, ' T=',temp
Print *, ' T Flotsam=',tempg
endif
ke2=0.d0
keg2=0.d0
pe=0.d0
virial=0.d0
return
end
C*****
subroutine LJ(r,force,potential,dxk,rcut,vijk,vrhat,
1 xhat,tdes,gauss,sig,eps)
real*8 r,ri,ri6,force,potential,dxk,rtest,rcut,vijk,vrhat,
1 forcec,forced,xhat,omegan,omegat,omegar,tdes,gauss,
2 sig,eps
rtest=3.d0
ri=1.d0/r
ri6=(sig*ri)**6.d0
forcec=24.d0*eps*ri*ri6*(2*ri6-1.d0)
potential=4.d0*eps*ri6*(ri6-1.d0)
if (r.gt.rtest) then
force=0
potential=0
endif
!Drag force
c friction=1.3d1
c omegan=(1.d0-r/rcut)**2
c omegat=(1.d0-r/rcut)**2*0
c
c normal=omegan*vrhat*dxk*ri
c tangential=omegat*(vijk-vrhat*dxk)
c forced=-friction*(normal+tangential)*0
c
!Random force
c omegar=(1.d0-r/rcut)
c sigma=sqrt(2.d0*friction*tdes)
c forcer=sigma*omegar*gauss*dxk*ri
force=(forcec)
return
end
C*****

```

```

SUBROUTINE RANDNUM(ISEED,Rnum)
REAL*8 DSEED,D2P31M,D2P31,Rnum
Integer ISEED
DATA D2P31M /2147483647.D0/
DATA D2P31 /2147483648.D0/
DSEED = float(ISEED)
DSEED = DMOD(16807.D0*DSEED,D2P31M)
Rnum = DSEED/D2P31
ISEED = INT(DSEED)
RETURN
END
C*****
subroutine input(tdes,rho,dt,tau,lamg,At,fcut,tsblk,nblk,ct,
1 xyzbol,tbol,tsam,CC,rcut,txyz,taug)
Real*8 tdes,rho,dt,tau,lamg,At,CC,fcut,taug,rcut
Integer tsblk,nblk,ct,dum,tsam,txyz
logical xyzbol,tbol
OPEN(10,FILE='input.txt',STATUS='old')
rewind 10
read (10,*) tdes
read (10,*) rho
read (10,*) dt
read (10,*) tau
read (10,*) taug
read (10,*) lamg
read (10,*) rcut
read (10,*) tsblk
read (10,*) nblk
read (10,*) ct
read (10,*) dum
if (dum.eq.0) then
xyzbol=.false.
else
xyzbol=.true.
endif
read (10,*) dum
if (dum.eq.0) then
tbol=.false.
else
tbol=.true.
endif
read (10,*) At

```

```

read (10,*) tsam
read (10,*) txyz
read (10,*) fcut
read (10,*) CC
CC=-CC
close(10)
return
end
C*****
SUBROUTINE comsol(x,n,rp,L,nc)
integer n,kkk,nc
REAL*8 x(5,n), rp, L
OPEN(14,FILE='particle.txt')
Rewind (14)
C C C-----Print out positions-----
206 format (I5)
306 format (F6.0)
406 format (3F10.4,2x,F5.3)
Write(14,206) n
Write(14,306) L
Write(14,206) nc
do kkk=1,n
Write(14,406)
1 x(1,kkk),x(2,kkk),x(3,kkk),x(4,kkk)
enddo
Close(14)
RETURN
END

```

Program for evaluating interfacial statistics as well as volume fractions for the DPP model.

```

*23456789012345678901234567890123456789012345678901234567890123456789012
PROGRAM bigmess
! density=number of grids per dimension
! np=total number of particles
! ng=number of total grid locations
! lambda=averaging radius relative to cell length
Parameter (density=967,np=2500,ng=density**3,lambda=0.2d0) !Input Parameters
REAL*8 x(3,np),rp(np),L,dL,rp2,r2,dx,cx,LI,
1 dI,sgndx,ratioAplace,ratioCplace,
2 z2(density,density),dz,ratioACplace,

```



```

3 Nx,Ny,Y(density,density),perA,
4 perC,perAC,areaA,areaC,areaAC,dy,ratioA,ratioC,
5 ratioAC,deriv,areaP,Cplace,Aplace,
6 totalarea,totalvolume,cy,cz,percentageA,
7 eppA2,eppC2,eppP2,eppA3,eppC3,eppP3,volumeA,
8 volumeC,volumeP,weightpercentageC,percentageC,
9 weightpercentageA,weightA,weightC,volumeS,eppS3
integer n,kkk,site,i,j,k,molec,site2,site3,nc,
1 p,Nbin,i2,j2,m
call particle(x,n,rp,L,np,nc)
dL=L/density
dI=1.d0/density
LI=1.d0/L
site=0
do m=1,10
eppA2=0.d0
eppC2=0.d0
eppP2=0.d0
weightpercentageC=0.d0
weightpercentageA=0.d0
weightA=0.d0
weightC=0.d0
ratioA=0.d0
ratioC=0.d0
ratioAC=0.d0
perA=0.d0
perC=0.d0
areaA=0.d0
areaC=0.d0
do i=1,density
do j=1,density
z2(i,j)=0.d0
Y(i,j)=0.d0
enddo
enddo
do molec=n-nc+1,n
rp2=(rp(molec)/2)**2
r2=0.d0
dx=0.d0
dy=0.d0
dz=0.d0
dz=x(3,molec)-(m*50)*dL

```

```

cz=(dz)-L*NINT((dz)*LI)
do i=1,density
dx=x(1,molec)-i*dL
cx=(dx)-L*NINT((dx)*LI)
do j=1,density
dy=x(2,molec)-j*dL
cy=(dy)-L*NINT((dy)*LI)
r2=cx*cx+cy*cy+cz*cz
if (r2.le.rp2) then !assign carbon material
z2(i,j)=128.d0
endif
enddo
enddo
enddo
do molec=1,n-nc
rp2=(rp(molec)/2)**2
r2=0.d0
dx=0.d0
dy=0.d0
dz=0.d0
dz=x(3,molec)-(m*50)*dL
cz=(dz)-L*NINT((dz)*LI)
do i=1,density
dx=x(1,molec)-i*dL
cx=(dx)-L*NINT((dx)*LI)
do j=1,density
dy=x(2,molec)-j*dL
cy=(dy)-L*NINT((dy)*LI)
r2=cx*cx+cy*cy+cz*cz
if (r2.le.rp2) then !assign active material
z2(i,j)=255.d0
endif
enddo
enddo
enddo
Nx=density
Ny=density
C voxulate the image
do i=1,Ny-1
do j=1,Nx-1
if (z2(i,j).gt.145) then
z2(i,j)=255

```

```

elseif (z2(i,j).lt.118) then
z2(i,j)=0
else
z2(i,j)=128
endif
enddo
enddo
C calculate the total number of sites for area calculations and volume sites
totalarea=(density-4)*(density-4)
totalvolume=density*density*density
C now calculate the edge of the active material particles
do i=2,Ny-2
do j=2,Nx-2
Y(i,j)=0
deriv=((z2((i+1),j)-z2(i,j))**2+(z2((i-1),j)-z2(i,j))**2+
1 (z2(i,(j+1))-z2(i,j))**2+(z2(i,(j-1))-z2(i,j))**2)
if ((deriv.gt.0) .and. z2(i,j).gt.250) then
Y(i,j)=255
else
Y(i,j)=0
endif
enddo
enddo
C now calculate the perimimeter of active material
perA=0
do i=2,Ny-2
do j=2,Nx-2
if (Y(i,j).gt.254) then
perA=perA+1
endif
enddo
enddo
C now calculate the area of active material for 2D slice
areaA=0
do i=2,Ny-2
do j=2,Nx-2
if (z2(i,j).gt.254) then
areaA=areaA+1
endif
enddo
enddo
C find the ratio of active material edge to area of active material

```

```

ratioA=perA/areaA
C calculate the porosity from the 2D slice
eppA2=areaA/totalarea
C calculate the weight of active material from the 3D slice
weightA=areaA*5.01d0
C do the same calculations for carbon material particles
do i=2,Ny-2
do j=2,Nx-2
Y(i,j)=0
deriv=((z2((i+1),j)-z2(i,j))**2+(z2((i-1),j)-z2(i,j))**2+
1 (z2(i,(j+1))-z2(i,j))**2+(z2(i,(j-1))-z2(i,j))**2)
if (deriv.gt.127 .and. z2(i,j).gt.127 .and.
1 z2(i,j).lt.129) then
Y(i,j)=255
else
Y(i,j)=0
endif
enddo
enddo
C now calculate the perimimeter
perC=0
do i=2,Ny-2
do j=2,Nx-2
if (Y(i,j).gt.254) then
perC=perC+1
endif
enddo
enddo
C now calculate the area
areaC=0
do i=2,Ny-2
do j=2,Nx-2
if (z2(i,j).gt.127 .and. z2(i,j).lt.129) then
areaC=areaC+1
endif
enddo
enddo
C find the ratio of active material edge to area of active material
ratioC=perC/areaC
C calculate the porosity from the 2D slice
eppC2=areaC/totalarea
C calculate the weight of carbon material from the 3D slice

```

```

weightC=areaC*1.95d0
C calculate the weight percentage of active material from the 3D slice
weightpercentageA=weightA/(weightA+weightC)
C calculate the weight percentage of carbon material from the 3D slice
weightpercentageC=weightC/(weightA+weightC)
C carbon to active material calculations
do i=2,Ny-2
do j=2,Nx-2
Y(i,j)=0
if (((z2(i+1,j)-z2(i,j))**2).gt.0 .and. z2(i,j).gt.127
1 .and. z2(i+1,j).gt.127) then
Y(i,j)=255
elseif (((z2(i-1,j)-z2(i,j))**2).gt.0 .and. z2(i,j).gt.127
1 .and. z2(i-1,j).gt.127) then
Y(i,j)=255
elseif (((z2(i,j+1)-z2(i,j))**2).gt.0 .and. z2(i,j).gt.127
1 .and. z2(i,j+1).gt.127) then
Y(i,j)=255
elseif (((z2(i,j-1)-z2(i,j))**2).gt.0 .and. z2(i,j).gt.127
1 .and. z2(i,j-1).gt.127) then
Y(i,j)=255
else
Y(i,j)=0
endif
enddo
enddo
C now calculate the perimimeter
perAC=0
do i=2,Ny-2
do j=2,Nx-2
if (Y(i,j).gt.254) then
perAC=perAC+1
endif
enddo
enddo
C now calculate the area
areaAC=0
do i=2,Ny-2
do j=2,Nx-2
if (z2(i,j).gt.127) then
areaAC=areaAC+1
endif

```

```

enddo
enddo
C find the ratio
ratioAC=perAC/areaAC
C calculate pore porosity
C now calculate the area
areaP=0
do i=2,Ny-2
do j=2,Nx-2
if (z2(i,j).lt.127) then
areaP=areaP+1
endif
enddo
enddo
C calculate the porosity from the 2D slice
eppP2=areaP/totalarea
C calculate the porosity from the 2D slice
eppP2=areaP/totalarea
C exporting everything
eppA2place=(eppA2+eppA2place)
eppC2place=(eppC2+eppC2place)
eppP2place=(eppP2+eppP2place)
Cplace=(weightC+Cplace)
Aplace=(weightA+Aplace)
percentageA=weightpercentageA+percentageA
percentageC=weightpercentageC+percentageC
ratioAplace=(ratioA+ratioAplace)
ratioCplace=(ratioC+ratioCplace)
ratioACplace=(ratioAC+ratioACplace)
enddo
eppA2=eppA2place/10
eppC2=eppC2place/10
eppP2=eppP2place/10
weightC=Cplace/10
weightA=Aplace/10
weightpercentageA=percentageA/10
weightpercentageC=percentageC/10
ratioA=ratioAplace/10
ratioC=ratioCplace/10
ratioAC=ratioACplace/10
C need to export the matrix Z, perA, perC, perAC, areaA, areaC, areaAC, ratioA....
OPEN(16,FILE='David3.txt')

```

```

Rewind (16)
980 format (F7.5,A)
write(16,*) 'eppA2 area based porosity'
write(16,980) eppA2
write(16,*) 'ratioA=perA/areaA'
write(16,980) ratioA
write(16,*) 'eppC2 area based porosity'
write(16,980) eppC2
write(16,*) 'ratioC=perC/areaC'
write(16,980) ratioC
write(16,*) 'ratioAC=perAC/areaCA'
write(16,980) ratioAC
write(16,*) 'eppP2 area based porosity'
write(16,980) eppP2
write(16,*) 'weightA'
write(16,*) weightA
write(16,*) 'weightC'
write(16,*) weightC
write(16,*) 'weightpercentageA'
write(16,980) weightpercentageA
write(16,*) 'weightpercentageC'
write(16,980) weightpercentageC
Close(16)
RETURN
END
*****
SUBROUTINE particle(x,n,rp,L,np,nc)
integer n,kkk,np,nc
REAL*8 x(3,np), rp(np), L
OPEN(14,FILE='particle.txt')
Rewind (14)
C C C-----read in positions-----
206 format (I5)
306 format (F6.0)
406 format (3F10.4,2x,F5.3)
Read(14,206) n
Read(14,306) L
Read(14,206) nc
do kkk=1,n
Read(14,406)
1 x(1,kkk),x(2,kkk),x(3,kkk),rp(kkk)
enddo

```

```
Close(14)
RETURN
END
```

Program to export 3D grid from the DPP model for COMSOL multiphysics.

```
*23456789012345678901234567890123456789012345678901234567890123456789012
PROGRAM bigmess
! density=number of grids per dimension
! np=total number of particles
! ng=number of total grid locations
! lambda=averaging radius relative to cell length
Parameter (density=50,np=2500,ng=density**3,lambda=0.2d0) !Input Parameters
integer n,kkk,site,i,j,k,molec,site2,site3,nc
REAL*8 x(3,np),rp(np),L,dL,y(3,ng),rp2,r2,dx,cx,LI,
1 z(3,ng),dI,cond(ng),sgndx,kap(3,ng),
2 kappa(density,density,density),ravg,
3 z2(density,density),condavg
call particle(x,n,rp,L,np,nc)
dL=L/density
dI=1.d0/density
LI=1.d0/L
site=0
ravg=0.d0
do i=1,n
ravg=ravg+rp(i)
enddo
ravg=ravg/n
do i=1,density
do j=1,density
do k=1,density
site=site+1
y(1,site)=(i)*dL
y(2,site)=(j)*dL
y(3,site)=(k)*dL
z(1,site)=(i)*dI
z(2,site)=(j)*dI
z(3,site)=(k)*dI
kap(1,site)=(i)
kap(2,site)=(j)
kap(3,site)=(k)
```



```

cond(site)=1.d0
kappa(i,j,k)=1.d0
enddo
enddo
enddo
do molec=n-nc+1,n
rp2=(rp(molec)/2)**2
do site2=1,ng
r2=0.d0
do k=1,3
dx=x(k,molec)-y(k,site2)
cx=dx-L*NINT(dx*LI)
r2=r2+cx*cx
enddo
if (r2.le.rp2) then !assign active material conductance
cond(site2)=0.05d0
c cond(site2)=1.0d0
kappa(kap(1,site2),kap(2,site2),kap(3,site2))=0.d0
endif
enddo
enddo
do molec=1,n-nc
rp2=(rp(molec)/2)**2
do site2=1,ng
r2=0.d0
do k=1,3
dx=x(k,molec)-y(k,site2)
cx=dx-L*NINT(dx*LI)
r2=r2+cx*cx
enddo
if (r2.le.rp2) then !assign active material conductance
cond(site2)=0.d0
kappa(kap(1,site2),kap(2,site2),kap(3,site2))=0.d0
endif
enddo
enddo
condavg=condavg/ng
OPEN(17,FILE='Comsol.txt')
Rewind (17)
! write(14,*) site, ng
C C C———Print out positions———
406 format (F7.5,A,F7.5,A,F7.5,A,F7.5)

```

```

do kkk=1,ng
Write(17,406)
1 z(1,kkk),char(9),z(2,kkk),char(9),z(3,kkk),
2 char(9),cond(kkk)
enddo
Close(17)
C Print out z2
do i=1,density
do j=1,density
z2(i,j)=kappa(i,j,5)
enddo
enddo
OPEN(15,FILE='David2.txt')
Rewind (15)
950 format (10000000(F7.2,A))
write(15,*) condavg
do i=1,density
write(15,950) (z2(i,j),char(9), j=1,density)
enddo
Close(15)
RETURN
END
*****

SUBROUTINE particle(x,n,rp,L,np,nc)
integer n,kkk,np,nc
REAL*8 x(3,np), rp(np), L
OPEN(14,FILE='particle.txt')
Rewind (14)
C C C-----read in positions-----
206 format (I5)
306 format (F6.0)
406 format (3F10.4,2x,F5.3)
Read(14,206) n
Read(14,306) L
Read(14,206) nc
do kkk=1,n
Read(14,406)
1 x(1,kkk),x(2,kkk),x(3,kkk),rp(kkk)
enddo
Close(14)
RETURN
END

```


Appendix B. SG model predict computer code with electronic and ionic capabilities

Main SG model code. Was programmed and compiled in a windows based Fortran 95 compiler.

```
*23456789012345678901234567890123456789012345678901234567890123456789012
  c You can do it, MC code
  c David Stephenson cetra 1999-2011
  c
  PROGRAM MC
  real altmac
  real*8 rhoA,rhoP
  C
  C
  C **Constants for calculations to follow
  C
  C Volume fractions of Pore and Active material from FIB 34%
  rhoA = 0.625
  rhoP = 0.34
  C Volume fractions of Pore and Active material from FIB 51%
  c rhoA = 0.446
  c rhoP = 0.51
  C
  call MCcode(rhoP,rhoA,altmac)
  STOP
  END
  C*****
  C Monte Carlo engine: based on nearest-neighbor probabilities between
  C three phases, determine a series of likely configurations. Calculate
  C statistics including tortuosity for the final configuration
  C*****
```

```

C
Subroutine MCcode(rhoP,rhoA,altmac)
integer density,dens2
integer movescount,ngrid
Parameter (density=220,dens2=density**2,ngrid=density**3)
c
c Don't let density be greater than 280, as program memory
c requirements will be about 50 bytes * ngrid. Make sure
c to do a search-and-replace throughout the program listing
c if changing the density=value because this parameter
c statement is repeated in other subroutines.
c
integer i,j,k,site,domaint,IRR,j1,site1,site2
integer nabor(6,ngrid),dnabor(12,ngrid),domain(ngrid),
1 position(3,ngrid)
real keff(9),potl(ngrid),length
common nabor,dnabor,domain,position,keff,potl,length
real Etot,error,tauistdev,keffint,taui1,altmac,eps,
1 Rnum,Trel,errorf,curve
integer direction
integer maxlbin,nblock,id1,id2,idn1,idn2,i5,i7
Parameter (maxlbin=55)
real*8 P2(0:2,0:2),P2tot(0:2,0:2),E2(0:2,0:2),
1 Pd2(0:2,0:2),Pd2tot(0:2,0:2),Ed2(0:2,0:2),
2 Pvol(0:2),P2sim(0:2,0:2),Pd2sim(0:2,0:2),Pi,Pt,
3 Pnorm,Pcurve(0:2,1000),Pcurvei,Pcurvet,varyC,
4 rhoA,rhoP,rhoC,condA,condC,condP
logical Pmove,edgeflag
integer*8 i6
c
c save IRR
c
c———calculate probs of particular configs from 2D image
call probimage(P2,Pd2,P2tot,Pd2tot,E2,Ed2,Pvol,Pcurve)
print *, 'before'
c lateral area fraction
print *, P2(0,0), 'P2(0,0)'
print *, P2(1,1), 'P2(1,1)'
print *, P2(2,2), 'P2(2,2)'
print *, P2(0,1), 'P2(0,1)'
print *, P2(1,0), 'P2(1,0)'
print *, P2(0,2), 'P2(0,2)'

```

```

print *, P2(2,0), 'P2(2,0)'
print *, P2(1,2), 'P2(1,2)'
print *, P2(2,1), 'P2(2,1)'
c now for the diagonal area fraction
print *, Pd2(0,0), 'Pd2(0,0)'
print *, Pd2(1,1), 'Pd2(1,1)'
print *, Pd2(2,2), 'Pd2(2,2)'
print *, Pd2(0,1), 'Pd2(0,1)'
print *, Pd2(1,0), 'Pd2(1,0)'
print *, Pd2(0,2), 'Pd2(0,2)'
print *, Pd2(2,0), 'Pd2(2,0)'
print *, Pd2(1,2), 'Pd2(1,2)'
print *, Pd2(2,1), 'Pd2(2,1)'
c
c—————experimental data (basis for objective function)
c Volume fractions of domains
rhoA=Pvol(0)
rhoC=Pvol(1)
rhoP=Pvol(2)
c values for 45% porosity
rhoP=0.366658527
rhoC=0.118730159
rhoA=1-rhoP-rhoC
c values for 51% porosity
c rhoP=0.449631273
c rhoC=0.115507077
c rhoA=1-rhoP-rhoC
c values other porosities
c varyC=0.17
c rhoA=Pvol(0)-varyC
c rhoC=Pvol(1)
c rhoP=Pvol(2)+varyC
c vary carbon fraction
varyC=0.4
rhoA=rhoA-varyC*(1-0.63)
rhoC=rhoC+varyC
rhoP=rhoP-varyC*(0.63)
c
print *, rhoP, 'rhoP'
print *, rhoA, 'rhoA'
print *, rhoC, 'rhoC'
write(6,*) 'porosity tot', (rhoP+rhoC*0.63)

```

```

Pvol(0)=rhoA
Pvol(1)=rhoC
Pvol(2)=rhoP
c Pvol(0)=0.45-(0.51-0.45011)
c Pvol(1)=1-rhoP-rhoC
c Pvol(2)=0.12
c A=0
c C=1
c P=2
P2(0,0) = 0.925237085/Pvol(0)
P2(1,1) = 0.863501059/Pvol(1)
P2(2,2) = 0.890484278/Pvol(2)
P2(0,1) = 0.009031047/(Pvol(0)*Pvol(1))
P2(1,0) = 0.009031047/(Pvol(1)*Pvol(0))
P2(0,2) = 0.029044873/(Pvol(0)*Pvol(2))
P2(2,0) = 0.029044873/(Pvol(2)*Pvol(0))
P2(1,2) = 0.007035876/(Pvol(1)*Pvol(2))
P2(2,1) = 0.007035876/(Pvol(2)*Pvol(1))
c now for the diagonal area fraction
Pd2(0,0) = 0.899818099/Pvol(0)
Pd2(1,1) = 0.817283444/Pvol(1)
Pd2(2,2) = 0.853704357/Pvol(2)
Pd2(0,1) = 0.012215658/(Pvol(0)*Pvol(1))
Pd2(1,0) = 0.012215658/(Pvol(1)*Pvol(0))
Pd2(0,2) = 0.039014728/(Pvol(0)*Pvol(2))
Pd2(2,0) = 0.039014728/(Pvol(2)*Pvol(0))
Pd2(1,2) = 0.009511548/(Pvol(1)*Pvol(2))
Pd2(2,1) = 0.009511548/(Pvol(2)*Pvol(1))
print *, 'after'
c lateral area fraction
print *, P2(0,0), 'P2(0,0)'
print *, P2(1,1), 'P2(1,1)'
print *, P2(2,2), 'P2(2,2)'
print *, P2(0,1), 'P2(0,1)'
print *, P2(1,0), 'P2(1,0)'
print *, P2(0,2), 'P2(0,2)'
print *, P2(2,0), 'P2(2,0)'
print *, P2(1,2), 'P2(1,2)'
print *, P2(2,1), 'P2(2,1)'
c now for the diagonal area fraction
print *, Pd2(0,0), 'Pd2(0,0)'
print *, Pd2(1,1), 'Pd2(1,1)'

```

```

print *, Pd2(2,2), 'Pd2(2,2)'
print *, Pd2(0,1), 'Pd2(0,1)'
print *, Pd2(1,0), 'Pd2(1,0)'
print *, Pd2(0,2), 'Pd2(0,2)'
print *, Pd2(2,0), 'Pd2(2,0)'
print *, Pd2(1,2), 'Pd2(1,2)'
print *, Pd2(2,1), 'Pd2(2,1)'
c A = 0
c C = 1
c P = 2
c Relative conductivities of domains (dimensionless) Electronic
condA = 0.0
condC = 0.05
condP = 1.0
length= 6*0.065
C-----initialize certain arrays if first time being called
c
write(6,*) 'Initializing'
write(6,*)
C initialize random number seed
IRR = 27644437
Rnum = 27644437
c 27644437
c Make neighbor list for six nearest lateral neighbors to given
c site; for pair interactions we apply periodic boundaries in
c x,y,z directions.
c Also create position array to locate site positions
site = 0
do i = 1, density
do j = 1, density
do k = 1, density
site = site + 1
nabor(1,site) = mod(i,density)*dens2
1 + (j-1)*density + k !direction +x
nabor(2,site) = mod(i-2+density,density)*dens2
1 + (j-1)*density + k !direction -x
nabor(3,site) = (i-1)*dens2 + mod(j,density)*density
1 + k !direction +y
nabor(4,site) = (i-1)*dens2
1 + mod(j-2+density,density)*density
1 + k !direction -y
nabor(5,site) = (i-1)*dens2 +(j-1)*density

```



```

1 + mod(k,density)+1 !direction +z
nabor(6,site) = (i-1)*dens2 + (j-1)*density
1 + mod(k-2+density,density)+1 !direction -z
c
c position array to locate x,y,z for site
position(1,site) = i
position(2,site) = j
position(3,site) = k
enddo
enddo
enddo
c
c Make neighbor list for twelve nearest diagonal neighbors to
c given site using previously developed lateral nabor list.
do site = 1, ngrid
dnabor(1,site) = nabor(3,nabor(1,site)) ! direction +x+y
dnabor(2,site) = nabor(4,nabor(2,site)) ! direction -x-y
dnabor(3,site) = nabor(4,nabor(1,site)) ! direction +x-y
dnabor(4,site) = nabor(3,nabor(2,site)) ! direction -x+y
dnabor(5,site) = nabor(5,nabor(3,site)) ! direction +y+z
dnabor(6,site) = nabor(6,nabor(4,site)) ! direction -y-z
dnabor(7,site) = nabor(6,nabor(3,site)) ! direction +y-z
dnabor(8,site) = nabor(5,nabor(4,site)) ! direction -y+z
dnabor(9,site) = nabor(1,nabor(5,site)) ! direction +z+x
dnabor(10,site) = nabor(2,nabor(6,site)) ! direction -z-x
dnabor(11,site) = nabor(2,nabor(5,site)) ! direction +z-x
dnabor(12,site) = nabor(1,nabor(6,site)) ! direction -z+x
enddo
c
c Initialize the node domain identities as 1D array
c change the value of volumes here
c
c calc numbers of nodes for each domain type
initialP = nint(Pvol(2)*ngrid)
initialA = nint(Pvol(0)*ngrid)
initialC = ngrid - initialP - initialA
c Put the three domains into the system
do site = 1, initialA
domain(site) = 0 !Active site
enddo
do site = initialA+1, initialA+initialC
domain(site) = 1 !Carbon site

```

```

enddo
do site = initialA+initialC+1, ngrid
domain(site) = 2 !Pore site
enddo
c
c scramble domains for initial configuration
do j1 = 1, 2*ngrid !loop through nodes twice
site1 = MOD(j1,ngrid)+1 !find 1st node sequentially
CALL RANDNUM(IRR,Rnum) !find 2nd node randomly
site2 = MOD(IRR,ngrid)+1
domainT = domain(site2) !swap domains of two nodes
domain(site2) = domain(site1)
domain(site1) = domainT
enddo
c
c tabulate pairwise effective conductivities, given
c pair domain types: Active (0), Carbon (1), Pore (2)
c The general formula is a harmonic mean:
c keff_ij = 2*cond_i*cond_j/(cond_i+cond_j+eps)
c where eps is a small parameter to ensure num. stability
c
eps = 1.E-9
keff(1) = condA
keff(2) = 2.*condA*condC/(condA+condC+eps)
keff(3) = 2.*condA*condP/(condA+condP+eps)
keff(4) = keff(2)
keff(5) = condC
keff(6) = 2.*condC*condP/(condC+condP+eps)
keff(7) = keff(3)
keff(8) = keff(6)
keff(9) = condP
c
c End of the initialization
c -----
c
c start of the main move loop
c
nblock=0
nblock = 2*ngrid !size of one block 1*ngrid
c Trel is temperature of sim relative to image
c and can be used to tweak randomness in sim results
Trel = 1.0

```

```

c quick type of programing for secondary loop
movescount=0
error=10000
do i6 = 1,2147483647
movescount=movescount+1
c error=0
c dowhile (error.gt.0.1)
c Trel = Trel-0.0000001
c if (Trel.lt.0) Trel=0
c loop to extend main loop
c do i6=1,2
c find two edge nodes randomly
c get unual configurations
do i7=1,nblock
do i5=1,100*100*1000
CALL RANDNUM(IRR,Rnum)
site1 = MOD(IRR,ngrid)+1
id1 = domain(site1)
edgeflag = .false.
do j1 = 1, 6 !loop over nearest neighbors
c if neighbor is of a different phase then accept
if (id1.ne.domain(nabor(j1,site1))) then
edgeflag = .true.
exit
endif
enddo
if (edgeflag) exit
do j1 = 1, 12 !loop over nearest neighbors
c if neighbor is of a different phase then accept
if (id1.ne.domain(dnabor(j1,site1))) then
edgeflag = .true.
exit
endif
enddo
if (edgeflag) exit
enddo
do i5=1,100*100*1000
CALL RANDNUM(IRR,Rnum)
site2 = MOD(IRR,ngrid)+1
id2 = domain(site2)
edgeflag = .false.
do j1 = 1, 6 !loop over nearest neighbors

```

```

c if neighbor is of a different phase then accept
if (id2.ne.domain(nabor(j1,site2))) then
edgeflag = .true.
exit
endif
enddo
if (edgeflag) exit
do j1 = 1, 12 !loop over nearest neighbors
c if neighbor is of a different phase then accept
if (id2.ne.domain(dnabor(j1,site2))) then
edgeflag = .true.
exit
endif
enddo
if (edgeflag) exit
enddo
c calculate the id of the sites
if (id2 .ne. id1) then !nontrivial solution
c Find probability of given site and neighbors
c as well as of trial change
Pi = 1.D0
Pt = 1.D0
c do lateral nearest neighbors
do j1 = 1, 6
idn1 = domain(nabor(j1,site1))
idn2 = domain(nabor(j1,site2))
Pi = Pi * P2(id1,idn1) * P2(id2,idn2)
Pt = Pt * P2(id1,idn2) * P2(id2,idn1)
enddo
c do diagonal nearest neighbors
do j1 = 1, 12
idn1 = domain(dnabor(j1,site1))
idn2 = domain(dnabor(j1,site2))
Pi = Pi * Pd2(id1,idn1) * Pd2(id2,idn2)
Pt = Pt * Pd2(id1,idn2) * Pd2(id2,idn1)
enddo
c find curve probability
c print *, IRR, 'id1 before'
c call prob(site1,id1,curve,IRR)
c print *, IRR, 'id1 after'
c Pcurvei=Pcurve(id1,int(curve*10))/Pvol(id1)
c Pcurvei=Pcurve(id1,int(curve*10))

```

```

c Pi=Pi*Pcurvei
c print *, id2, 'id2 before'
c call prob(site2,id2,curve,IRR)
c print *, id2, 'id2 after'
c Pcurvet=Pcurve(id2,int(curve*10))/Pvol(id2)
c Pcurvet=Pcurve(id2,int(curve*10))
c Pt=Pt*Pcurvet
c
c determine whether to accept trial move
if (Pt .ge. Pi) then !auto accept favorable move
Pmove = .true.
elseif (Pt .le. 0.D0) then !auto reject impossible move
Pmove = .false.
else !conditionally accept unfavorable move
c Trel=0 !c this out for now
CALL RANDNUM(IRR,Rnum)
if (Pt .gt. Pi*Rnum**Trel) then
Pmove = .true.
else
Pmove = .false.
endif
endif
if (Pmove) then
domain(site1) = id2
domain(site2) = id1
endif
endif
c enddo !enddo of extend loop
c do j2 = 0, 2
c do j1 = 0, 2
c print *, P2
c print *, Pd2
c enddo
c enddo
c call stats(P2sim,Pd2sim,P2tot,Pd2tot,E2,Ed2,
c 1 Etot,error)
c do j2 = 0, 2
c do j1 = 0, 2
c print *, 'madeit2'
c print *, Pd2tot
c print *, Pd2sim
c enddo

```

```

c enddo
c print *, 'madeit2'
c testing an idea
c
c monitor progress during secondary run
c
if (mod(movescount,nblock) .eq. 0) then
c calculate inter-domain areas and energy per
c node based on final config of each block
call stats(P2sim,Pd2sim,P2tot,Pd2tot,E2,Ed2,
1 Etot,error)
write(6,'(A,I3,3(A,F8.4))' ) 'time block ',
1 movescount/nblock,' energy =' ,Etot,
2 ' error =' ,error
c correct probabilities and energies to improve result
call getcorr(P2sim,P2tot,P2,E2)
call getcorr(Pd2sim,Pd2tot,Pd2,Ed2)
c if (movescount/nblock .gt. 10) then
c print *, 'Trel',Trel
c if (error.gt.(errort+10.001)) exit
c errort=error
c endif
endif
enddo !end the secondary loop
do i7=1,0 !10*ngrid/600
do i5=1,100*100*1000
CALL RANDNUM(IRR,Rnum)
site1 = MOD(IRR,ngrid)+1
id1 = domain(site1)
edgeflag = .false.
do j1 = 1, 6 !loop over nearest neighbors
c if neighbor is of a different phase then accept
if (id1.ne.domain(nabor(j1,site1))) then
edgeflag = .true.
exit
endif
enddo
if (edgeflag) exit
do j1 = 1, 12 !loop over nearest neighbors
c if neighbor is of a different phase then accept
if (id1.ne.domain(dnabor(j1,site1))) then
edgeflag = .true.

```

```

exit
endif
enddo
if (edgeflag) exit
enddo
do i5=1,100*100*1000
CALL RANDNUM(IRR,Rnum)
site2 = MOD(IRR,ngrid)+1
id2 = domain(site2)
edgeflag = .false.
do j1 = 1, 6 !loop over nearest neighbors
c if neighbor is of a different phase then accept
if (id2.ne.domain(nabor(j1,site2))) then
edgeflag = .true.
exit
endif
enddo
if (edgeflag) exit
do j1 = 1, 12 !loop over nearest neighbors
c if neighbor is of a different phase then accept
if (id2.ne.domain(dnabor(j1,site2))) then
edgeflag = .true.
exit
endif
enddo
if (edgeflag) exit
enddo
c calculate the id of the sites
if (id2 .ne. id1) then !nontrivial solution
c Find probability of given site and neighbors
c as well as of trial change
Pi = 1.D0
Pt = 1.D0
c find curve probability
call prob(site1,id1,curve,IRR)
if (curve.gt.0) then
Pcurvei=Pcurve(id1,int(curve*10))/Pvol(id1)
else
Pcurvei=1
endif
Pi=Pi*Pcurvei
call prob(site2,id2,curve,IRR)

```

```

if (curve.gt.0) then
Pcurvei=Pcurve(id1,int(curve*10))/Pvol(id1)
else
Pcurvei=1
endif
Pi=Pi*Pcurvei
call prob(site1,id2,curve,IRR)
if (curve.gt.0) then
Pcurvet=Pcurve(id1,int(curve*10))/Pvol(id1)
else
Pcurvet=0
endif
Pt=Pt*Pcurvet
call prob(site2,id1,curve,IRR)
if (curve.gt.0) then
Pcurvet=Pcurve(id1,int(curve*10))/Pvol(id1)
else
Pcurvet=0
endif
Pt=Pt*Pcurvet
c
c determine whether to accept trial move
if (Pt .ge. Pi) then !auto accept favorable move
Pmove = .true.
elseif (Pt .le. 0.D0) then !auto reject impossible move
Pmove = .false.
else !conditionally accept unfavorable move
c Trel=0 !c this out for now
CALL RANDNUM(IRR,Rnum)
if (Pt .gt. Pi*Rnum**Trel) then
Pmove = .true.
else
Pmove = .false.
endif
endif
if (Pmove) then
domain(site1) = id2
domain(site2) = id1
endif
endif
c
enddo !end the secondary loop

```



```

write(6,*) 'end of loop'
call stats(P2sim,Pd2sim,P2tot,Pd2tot,E2,Ed2,
1 Etot,error)
write(6,'(A,I3,3(A,F8.4))') 'time block ',
1 movescount/nblock,' energy =' ,Etot,
2 ' error =' ,error
c if (error.le.1.00) exit
if (error.gt.(errort+0.0005)) exit
errort=error
enddo
c
c-----
c collect properties on final configuration
c
c
c calculate tortuosity averaged over three coord directions
c and get standard deviation
c
c Reset property accumulators
taui1 = 0.
taui2 = 0.
c calculate the ionic resistances
print *, 'made it to tau'
do direction = 1,3
call gettau(direction,rhoP,rhoC,condP,taui)
taui1 = taui1 + taui/3.
taui2 = taui2 + taui*taui/3.
enddo
tauistdev = sqrt((taui2 - taui1*taui1)/2.)
c
c turn tortuosity into alternative MacMullin number
altmac = (rhoP+rhoC*0.63)**0.53/(taui1+1.E-9)
c print *, 'altmac', altmac
c calculate the electronic resistances
c Relative conductivities of domains (dimensionless) Electronic
c loop through 5 condA values
do i5=1,11
condA = 0.05*(real(i5)-1)
condC = 1.0
condP = 0.0
eps = 1.E-9
keff(1) = condA

```

```

keff(2) = 2.*condA*condC/(condA+condC+eps)
keff(3) = 2.*condA*condP/(condA+condP+eps)
keff(4) = keff(2)
keff(5) = condC
keff(6) = 2.*condC*condP/(condC+condP+eps)
keff(7) = keff(3)
keff(8) = keff(6)
keff(9) = condP
print *, ''
print *, ''
print *, 'made it to sigma',i5
print *, ''
print *, 'condA', keff(1)
print *, ''
do direction = 1,3
call gettau2(direction,rhoP,rhoC,condP,taui)
tauil = tauil + taui/3.
tauil2 = tauil2 + taui*taui/3.
enddo
tauistdev = sqrt((tauil2 - tauil*tauil)/2.)
print *, ''
print *, 'end of sigma',i5
print *, ''
print *, ''
enddo
c
c export data
c
OPEN(15,FILE='MC_old_results.txt')
Rewind (15)
do j1=6,15,9
write(j1,*) '*****'
write(j1,*)
write(j1,*) 'final config averages'
write(j1,*) 'energy = ',Etot
write(j1,*) 'inv tau = ',tauil
write(j1,*) ' st dev = ',tauistdev
write(j1,*)
write(j1,*) 'altmac = ',altmac
write(j1,*)
write(j1,*) 'volume fractions'
write(j1,*) ' original coarse-grain'

```

```

write(j1,98) ' A',rhoA,Pvol(0)
write(j1,98) ' C',rhoC,Pvol(1)
write(j1,98) ' P',rhoP,Pvol(2)
write(j1,*)
write(j1,*) 'lateral area fractions'
write(j1,*) ' pair sim image'
write(j1,99)' AA ', P2sim(0,0), P2tot(0,0)
write(j1,99)' AC+CA',2*P2sim(0,1),2*P2tot(0,1)
write(j1,99)' AP+PA',2*P2sim(0,2),2*P2tot(0,2)
write(j1,99)' CC ', P2sim(1,1), P2tot(1,1)
write(j1,99)' CP+PC',2*P2sim(1,2),2*P2tot(1,2)
write(j1,99)' PP ', P2sim(2,2), P2tot(2,2)
write(j1,*)
write(j1,*) 'diagonal area fractions'
write(j1,*) ' pair sim image'
write(j1,99)' AA ', Pd2sim(0,0), Pd2tot(0,0)
write(j1,99)' AC+CA',2*Pd2sim(0,1),2*Pd2tot(0,1)
write(j1,99)' AP+PA',2*Pd2sim(0,2),2*Pd2tot(0,2)
write(j1,99)' CC ', Pd2sim(1,1), Pd2tot(1,1)
write(j1,99)' CP+PC',2*Pd2sim(1,2),2*Pd2tot(1,2)
write(j1,99)' PP ', Pd2sim(2,2), Pd2tot(2,2)
write(j1,*)
write(j1,*) ' sum squared area error =' ,error
98 FORMAT(A,2F10.4)
99 FORMAT(A,2F8.4)
write(j1,*)
write(j1,*) 'initial pair energies'
write(j1,*) ' pair lat diag'
write(j1,99)' AA ',-LOG(P2tot(0,0)*Pvol(2)**2
1 /Pvol(0)/Pvol(0)/P2tot(2,2)),
2 -LOG(Pd2tot(0,0)*Pvol(2)**2
3 /Pvol(0)/Pvol(0)/Pd2tot(2,2))
write(j1,99)' AC ',-LOG(P2tot(0,1)*Pvol(2)**2
1 /Pvol(0)/Pvol(1)/P2tot(2,2)),
2 -LOG(Pd2tot(0,1)*Pvol(2)**2
3 /Pvol(0)/Pvol(1)/Pd2tot(2,2))
write(j1,99)' AP ',-LOG(P2tot(0,2)*Pvol(2)**2
1 /Pvol(0)/Pvol(2)/P2tot(2,2)),
2 -LOG(Pd2tot(0,2)*Pvol(2)**2
3 /Pvol(0)/Pvol(2)/Pd2tot(2,2))
write(j1,99)' CC ',-LOG(P2tot(1,1)*Pvol(2)**2
1 /Pvol(1)/Pvol(1)/P2tot(2,2)),

```

```

2 -LOG(Pd2tot(1,1)*Pvol(2)**2
3 /Pvol(1)/Pvol(1)/Pd2tot(2,2))
write(j1,99)' CP ',-LOG(P2tot(1,2)*Pvol(2)**2
1 /Pvol(1)/Pvol(2)/P2tot(2,2)),
2 -LOG(Pd2tot(1,2)*Pvol(2)**2
3 /Pvol(1)/Pvol(2)/Pd2tot(2,2))
write(j1,99)' PP ',0.,0.
write(j1,*)
write(j1,*) 'final pair energies'
write(j1,*) ' pair lat diag'
write(j1,99)' AA ',E2(0,0),Ed2(0,0)
write(j1,99)' AC ',E2(0,1),Ed2(0,1)
write(j1,99)' AP ',E2(0,2),Ed2(0,2)
write(j1,99)' CC ',E2(1,1),Ed2(1,1)
write(j1,99)' CP ',E2(1,2),Ed2(1,2)
write(j1,99)' PP ',E2(2,2),Ed2(2,2)
write(j1,*)
c write(j1,*) 'lines2'
c write(j1,*) ' avglength = ',avglength
c write(j1,*) ' stdevlength = ',stdevlength
c write(j1,*) ' avgsquare = ',avgsquare
c write(j1,*) ' stdevsquare = ',stdevsquare
c write(j1,*) ' avgratio = ',avgratio
c write(j1,*) ' stdevratio = ',stdevratio
enddo
Close(15)
c
c output file for comsol
c OPEN(17,FILE='Comsol.txt')
c Rewind (17)
c write(17,*) 'Output: xyz positions, conductivity, potential'
c do site = 1,ngrid
c Write(17,406)
c 1 position(1,site)/float(density),char(9),
c 2 position(2,site)/float(density),char(9),
c 3 position(3,site)/float(density),char(9),
c 4 keff(1+4*domain(site))
c 5 ,char(9),potl(site)
c enddo
c Close(17)
OPEN(19,FILE='pic3.txt')
do site=1,ngrid

```

```

if (domain(site).eq.0) then
keffint=255
elseif (domain(site).eq.1) then
keffint=140
else
keffint=0
endif
if (position(2,site).eq.density/2) then
Write(19,*) position(1,site),char(9),
c 1 position(2,site),char(9),
2 position(3,site),char(9),keffint
endif
enddo
Close(19)
RETURN
END
C*****
C calculate pseudo-random number, evenly distributed
C from 0 to 1, using integer seed
C*****
SUBROUTINE RANDNUM(ISEED,Rnum)
REAL*8 DSEED,D2P31M,D2P31
REAL Rnum
INTEGER ISEED
DATA D2P31M /2147483647.D0/
DATA D2P31 /2147483648.D0/
DSEED = DBLE(ISEED)
DSEED = DMOD(16807.D0*DSEED,D2P31M)
Rnum = DSEED/D2P31
ISEED = INT(DSEED)
RETURN
END
C*****
C Calculate the probability statistics from the image
C Arrays P2,P2tot, and E2 have two dimensions as follows
C *node 1 ID: values 0=active, 1=carbon, 2=pore
C *node 2 ID: values 0=active, 1=carbon, 2=pore
C
C*****
SUBROUTINE probimage(P2,Pd2,P2tot,Pd2tot,E2,Ed2,Pvol
1 ,Pcurve)
real*8 P2(0:2,0:2),P2tot(0:2,0:2),E2(0:2,0:2),Pvol(0:2),

```

```

1 Pd2(0:2,0:2),Pd2tot(0:2,0:2),Ed2(0:2,0:2),
2 Po2(0:2,0:2),Po2tot(0:2,0:2),Pcurve(0:2,1000)
integer U(2000,2000),site2(2),site1(2),lengthmax
integer bins(2),j1,j2,j3,j4,j5,j6,j7,id,id1,id2,nd,site(2),
1 sitex,sitey,numsampl,IRR,ngrid2,maxsampl,sitesave(2)
integer sitecent(2),numsampl2(0:2),lengthedge,rn(2),trn1
real dn,rmove(2),unitvect(2,2),curve,lengthstraight
integer rnstart(2),counter,moves
logical edgeflag,edgepartic
IRR = 27644437
Rnum = 27644437
nd=2
id2=0
c specify image size
bins(1) = 601 !columns
bins(2) = 90 !rows
c
c read in image data
OPEN(9,FILE='6imagecircle34.dat',err=100)
Rewind (9)
do sitey = 1,bins(2)
read(9,*,end=100) (U(sitex,sitey),sitex=1,bins(1))
enddo
Close(9)
goto 200
100 print*, 'problem with imagecircle.dat'
stop
200 continue
c
c initialize prob arrays
do j2 = 0, 2
do j1 = 0, 2
P2tot(j1,j2) = 0.D0
Pd2tot(j1,j2) = 0.D0
Po2tot(j1,j2) = 0.D0
enddo
Pvol(j2) = 0.D0
enddo
c
c number of samples (used to normalize probabilities)
numsampl = (bins(1)-1)*(bins(2)-1)
c

```

```

c loop over all nearest pairs of pixels in the image
c and accumulate pair identities, making sure P2tot
c and Pd2tot are symmetric and properly normalized.
do j4 = 1, bins(2)-1
do j3 = 1, bins(1)
id = U(j3,j4) !identify domain of central pixel
if (j3 .lt. bins(1)) then
c accum lateral pair samples
id1 = U(j3+1,j4) !ID domain of neighbor to right
id2 = U(j3,j4+1) !ID domain of neighbor below
P2tot(id,id1) = P2tot(id,id1) + 0.25D0/numsampl
P2tot(id1,id) = P2tot(id1,id) + 0.25D0/numsampl
P2tot(id,id2) = P2tot(id,id2) + 0.25D0/numsampl
P2tot(id2,id) = P2tot(id2,id) + 0.25D0/numsampl
c accum estimated out-of-plane samples
CALL RANDNUM(IRR,Rnum) !estimate node above
j2 = MOD(IRR,9)
j3mod = j3+MOD(j2,3)-1
if (j3mod .lt. 1) j3mod=j3mod+bins(1)
j4mod = j4+j2/3-1
if (j4mod .lt. 1) j4mod=j4mod+bins(2)
id1 = U(j3mod,j4mod)
Po2tot(id,id1) = Po2tot(id,id1) + 0.5D0/numsampl
Po2tot(id1,id) = Po2tot(id1,id) + 0.5D0/numsampl
c accum diagonal pair samples
id2 = U(j3+1,j4+1) !ID domain of neighbor to lower right
Pd2tot(id,id2) = Pd2tot(id,id2) + 0.25D0/numsampl
Pd2tot(id2,id) = Pd2tot(id2,id) + 0.25D0/numsampl
endif
if (j3 .gt. 1) then
c accum more diagonal pair samples
id1 = U(j3-1,j4+1) !ID domain of neighbor to lower left
Pd2tot(id,id1) = Pd2tot(id,id1) + 0.25D0/numsampl
Pd2tot(id1,id) = Pd2tot(id1,id) + 0.25D0/numsampl
endif
c accumulate volume fraction samples
Pvol(id) = Pvol(id) + 1.D0/numsampl
enddo
enddo
c
c renormalize pair probability by single probabilities
do j2 = 0, 2

```

```

do j1 = 0, 2
P2(j1,j2) = P2tot(j1,j2)/(Pvol(j1)*Pvol(j2))
Pd2(j1,j2) = Pd2tot(j1,j2)/(Pvol(j1)*Pvol(j2))
Po2(j1,j2) = Po2tot(j1,j2)/(Pvol(j1)*Pvol(j2))
enddo
enddo
c
c get dimensionless pair energies (E/kT) relative
c to the pore-pore interaction
do j2 = 0, 2
do j1 = 0, 2
E2(j1,j2) = -LOG(P2(j1,j2)/P2(2,2))
Ed2(j1,j2) = -LOG(Pd2(j1,j2)/Pd2(2,2))
enddo
enddo
c
c output histograms
c
open(5,file="image_histogram_pairs.csv")
rewind(5)
write(5,*) 'probability histograms of image file'
write(5,*)
write(5,*) 'id, volfrac'
do j1 = 0, 2
write(5,*) j1,',',Pvol(j1)
enddo
write(5,*)
write(5,*) 'lateral nearest neighbor full pair probabilities'
write(5,*) ', A, C, P'
write(5,*) 'A',(' ',P2tot(0,j1),j1=0,2)
write(5,*) 'C',(' ',P2tot(1,j1),j1=0,2)
write(5,*) 'P',(' ',P2tot(2,j1),j1=0,2)
write(5,*)
write(5,*) 'diagonal nearest neighbor full pair probabilities'
write(5,*) ', A, C, P'
write(5,*) 'A',(' ',Pd2tot(0,j1),j1=0,2)
write(5,*) 'C',(' ',Pd2tot(1,j1),j1=0,2)
write(5,*) 'P',(' ',Pd2tot(2,j1),j1=0,2)
write(5,*)
write(5,*) 'out of plane nearest neighbor full pair probabilities'
write(5,*) ', A, C, P'
write(5,*) 'A',(' ',Po2tot(0,j1),j1=0,2)

```



```

write(5,*) 'C',(',',Po2tot(1,j1),j1=0,2)
write(5,*) 'P',(',',Po2tot(2,j1),j1=0,2)
write(5,*)
write(5,*) 'lateral nearest neighbor pair probabilities'
write(5,*) 'relative to random arrangements'
write(5,*) ', A, C, P'
write(5,*) 'A',(',',P2(0,j1),j1=0,2)
write(5,*) 'C',(',',P2(1,j1),j1=0,2)
write(5,*) 'P',(',',P2(2,j1),j1=0,2)
write(5,*)
write(5,*) 'diagonal nearest neighbor pair probabilities'
write(5,*) 'relative to random arrangements'
write(5,*) ', A, C, P'
write(5,*) 'A',(',',Pd2(0,j1),j1=0,2)
write(5,*) 'C',(',',Pd2(1,j1),j1=0,2)
write(5,*) 'P',(',',Pd2(2,j1),j1=0,2)
write(5,*)
write(5,*) 'out of plane nearest neighbor pair probabilities'
write(5,*) 'relative to random arrangements'
write(5,*) ', A, C, P'
write(5,*) 'A',(',',Po2(0,j1),j1=0,2)
write(5,*) 'C',(',',Po2(1,j1),j1=0,2)
write(5,*) 'P',(',',Po2(2,j1),j1=0,2)
write(5,*)
write(5,*) 'lateral nearest neighbor pair Energies (E/kT)'
write(5,*) ', A, C, P'
write(5,*) 'A',(',',E2(0,j1),j1=0,2)
write(5,*) 'C',(',',E2(1,j1),j1=0,2)
write(5,*) 'P',(',',E2(2,j1),j1=0,2)
write(5,*)
write(5,*) 'diagonal nearest neighbor pair Energies (E/kT)'
write(5,*) ', A, C, P'
write(5,*) 'A',(',',Ed2(0,j1),j1=0,2)
write(5,*) 'C',(',',Ed2(1,j1),j1=0,2)
write(5,*) 'P',(',',Ed2(2,j1),j1=0,2)
c close(5)
print*, 'image_histogram_pairs.csv written'
c now calculate Pcurve probabilities
c max number of sample attempts
maxsampl = 4*bins(1)*bins(2)
c initialize sample counter
do j1=0,2

```

```

numsampl2(j1) = 0
enddo
c initialize probability counter
do j1=1,3
do j2=1,1000
Pcurve(j1,j2)=0
enddo
enddo
lengthstraight=0
lengthedge=0
site1(1)=0
site1(2)=0
site2(1)=0
site2(2)=0
c loop over starting locations
ngrid2 = NINT(SQRT(FLOAT(bins(1)**2 + bins(2)**2)))
c mousehunt programming for finding the length of an edge
do j7=1, maxsampl !loop through to sample everything
c restart looking for an edge site
do while (.true.)
c pick a random site
do j1 = 1, nd
CALL RANDNUM(IRR,Rnum)
sitecent(j1) = MOD(IRR,bins(j1))+1
enddo
id = U(sitecent(1),sitecent(2))
c see if its at the edge of image then try new site
if ((sitecent(1).gt.bins(1)-1)
1 .or.(sitecent(2).gt.bins(2)-1)
2 .or.(sitecent(1).lt.2)
3 .or.(sitecent(2).lt.2)) cycle
c determine if its an edge site
rn(1)=0
rn(2)=0
if (U(sitecent(1),sitecent(2)+1).ne.id) then
rn(2) = 1
exit
elseif (U(sitecent(1),sitecent(2)-1).ne.id) then
rn(2) = -1
exit
elseif (U(sitecent(1)+1,sitecent(2)).ne.id) then
rn(1) = 1

```

```

exit
elseif (U(sitecent(1)-1,sitecent(2)).ne.id) then
rn(1) = -1
exit
endif
enddo
c start of the mousehunt algorithm
lengthedge=0
site1(1)=sitecent(1)
site1(2)=sitecent(2)
j1=0
lengthmax=5
do moves = 1, lengthmax !this is the length measured
do counter = 1, 4
c turn left
trn1 = rn(1)
rn(1) = -rn(2)
rn(2) = trn1
c check for way out
if (U(site1(1)+rn(1),site1(2)+rn(1)).eq.id) exit
enddo
c move to new site
do j1=1,2
site1(j1) = site1(j1) + rn(j1)
enddo
c stop moves if back where started
if ((site1(1).eq.sitecent(1))
1 .and.(site1(2).eq.sitecent(2))) exit
c stop moves if at edge of image
if ((site1(1).gt.bins(1)-1)
1 .or.(site1(2).gt.bins(2)-1)
2 .or.(site1(1).lt.2)
3 .or.(site1(2).lt.2)) exit
c now turn to the right twice
rn(1) = -rn(1)
rn(2) = -rn(2)
enddo !end moves loop
c reject sample if didn't do 5 moves
if (moves .lt. lengthmax) cycle
site2(1)=sitecent(1)
site2(2)=sitecent(2)
lengthstraight=sqrt(real(site1(1)-site2(1))**2+

```

```

1 real(site1(2)-site2(2))**2)
c record curve
curve=lengthstraight/real(moves)
c record probability
Pcurve(id,int(curve*10))=Pcurve(id,int(curve*10))+1
numsampl2(id)=numsampl2(id)+1
lengthedge=0
lengthstraight=0
curve=0
enddo !enddo for maxsampl
write(5,*) 'Pcurve values'
do j1=0,2
do j2=1,1000
if (numsampl2(j1).le.0) then
Pcurve(j1,j2)=0
else
Pcurve(j1,j2)=Pcurve(j1,j2)/numsampl2(j1)
endif
write(5,*) Pcurve(j1,j2)
enddo
enddo
close(5)
return
end
C*****
C Correct probability matrix used to generate moves (P2) and
C energy (E2) by comparing discrepancy between P2sim and P2tot
C*****
SUBROUTINE getcorr(P2sim,P2tot,P2,E2)
real*8 P2sim(0:2,0:2),P2tot(0:2,0:2),P2(0:2,0:2),
1 E2(0:2,0:2),Pnorm
real correx
integer j1,j2
c
correx = 0.01
c if correx > 1 then more aggressive correction
c if correx between 0 and 1 then less aggressive correction
c
Pnorm = 0.
do j2 = 0, 2
do j1 = 0, 2
P2(j1,j2) = P2(j1,j2)*(P2tot(j1,j2)/P2sim(j1,j2))**correx

```

```

Pnorm = Pnorm + P2(j1,j2)
enddo
enddo
do j2 = 0, 2
do j1 = 0, 2
E2(j1,j2) = -LOG(P2(j1,j2)/P2(2,2))
P2(j1,j2) = P2(j1,j2)/Pnorm
enddo
enddo
return
end
C*****
C Calculate a move probability for a site
C *****NOT CURRENTLY USED, BUT COULD BE ADAPTED TO GET
C INTERESTING LINE STATISTICS*****
C*****
SUBROUTINE prob(sitecent,id,curve,IRR)
integer maxlbin,density,ngrid,nd
Parameter (maxlbin=55,density=220,ngrid=density**3,nd=3)
integer site,j1,j2,j3,j4,j5,j6,j7,id,IRR,site1,site2
integer nabor(6,ngrid),dnabor(12,ngrid),domain(ngrid),
1 position(3,ngrid),id2,id3,lengthmax
real keff(9),potl(ngrid),length,curve,lengthstraight
common nabor,dnabor,domain,position,keff,potl,length
integer sitecent,lengthedge,IRRsave,neighborlist,rn2(2)
real dn,rmove(nd),rn(nd),unitvect(2,nd),Rnum,L(18)
integer moves,counter
logical edgeflag
lengthmax=5
c
c pick a random spherical direction to look at for a line (vector 1)
c reset dn to gt 1
dn = 10.
dowhile (dn .gt. 1.0)
dn = 0.
do j1 = 1, nd
CALL RANDNUM(IRR,Rnum)
rn(j1) = Rnum*2.0 - 1.0
dn = dn + rn(j1)**2
enddo
enddo
c normalize direction vector 1

```

```

do j1 = 1, nd
unitvect(1,j1) = rn(j1)/sqrt(dn)
enddo
c repeat for vector 3
dn = 10.
dowhile (dn .gt. 1.0)
dn = 0.
do j1 = 1, nd
CALL RANDNUM(IRR,Rnum)
rn(j1) = Rnum*2.0 - 1.0
dn = dn + rn(j1)**2
enddo
enddo
c normalize direction vector 3
do j1 = 1, nd
rn(j1) = rn(j1)/sqrt(dn)
enddo
c vector 2 is cross product of vectors 1 and 3
unitvect(2,1) = unitvect(1,2)*rn(3) - unitvect(1,3)*rn(2)
unitvect(2,2) = unitvect(1,3)*rn(1) - unitvect(1,1)*rn(3)
unitvect(2,3) = unitvect(1,1)*rn(2) - unitvect(1,2)*rn(1)
c (vector 3 is discarded and vectors 1,2 are orthogonal)
c
c initialize counter for line neighbors
lengthedge=0
lengthstraight=0.
curve=0.
neighborlist=0
c
c
c reset move accumulator and starting position
do j1 = 1, nd
rmove(j1) = 0.
enddo
site = sitecent
id2 = domain(site) !identify primary node
c find and edge site
c find the neighbor in the + direction
edgeflag = .false.
c find the plane's neighbors and then loop over those neighbors
c use the process of elimination, set up a length array + vect1
do j7=1,4

```

```

rn2(1)=1
rn2(2)=1
c algorithm for finding neighbors in the rn(1),rn(2) direction in 3D space
do j1=1,6
L(j1)=sqrt((position(1,site)+rn2(1)*unitvect(rn2(2),1)*10-
1 position(1,nabor(j1,site)))**2
2 +(position(2,site)+rn2(1)*unitvect(rn2(2),2)*10
3 -position(2,nabor(j1,site)))**2
4 +(position(3,site)+rn2(1)*unitvect(rn2(2),3)*10
5 -position(3,nabor(j1,site)))**2)
enddo
do j1=1,12
L(j1+6)=sqrt((position(1,site)+rn2(1)*unitvect(rn2(2),1)*10-
1 position(1,dnabor(j1,site)))**2
2 +(position(2,site)+rn2(1)*unitvect(rn2(2),2)*10
3 -position(2,dnabor(j1,site)))**2
4 +(position(3,site)+rn2(1)*unitvect(rn2(2),3)*10
5 -position(3,dnabor(j1,site)))**2)
enddo
c find the minimum distance
do j1=1,18
if (L(j1).eq.(min(L(1),L(2),L(3),L(4),L(5),L(6),L(7),L(8),L(9)
1 ,L(10),L(11),L(12),L(13),L(14),L(15),L(16),L(17),L(18)))) then
neighborlist=j1
exit
endif
enddo
edgeflag = .false.
if (neighborlist.le.6) then
j5=neighborlist
site2=nabor(j5,site)
edgeflag = .false.
c if neighbor is of a same phase then move
if (id2.eq.domain(nabor(j5,site))) then
edgeflag = .true.
exit
endif
if (edgeflag) exit
elseif (neighborlist.ge.7) then
j5=neighborlist-6
site2=dnabor(j5,site)
c if neighbor is of a different phase then accept

```

```

if (id2.eq.domain(dnabor(j5,site))) then
edgeflag = .true.
exit
endif
if (edgeflag) exit
endif
c look to the left
if (rn2(1).eq.1.and.rn2(2).eq.1) then
rn2(1)=1
rn2(2)=2
elseif (rn2(1).eq.1.and.rn2(2).eq.2) then
rn2(1)=-1
rn2(2)=1
elseif (rn2(1).eq.-1.and.rn2(2).eq.1) then
rn2(1)=-1
rn2(2)=2
endif
enddo !end moves loop
c start of the mousehunt algorithm
if (edgeflag) then !look for an edge if an edge was found
lengthedge=0
site1=site
do moves = 1, lengthmax
do counter = 1, 4
c turn left
if (rn2(1).eq.1.and.rn2(2).eq.1) then
rn2(1)=1
rn2(2)=2
elseif (rn2(1).eq.1.and.rn2(2).eq.2) then
rn2(1)=-1
rn2(2)=1
elseif (rn2(1).eq.-1.and.rn2(2).eq.1) then
rn2(1)=-1
rn2(2)=2
elseif (rn2(1).eq.-1.and.rn2(2).eq.2) then
rn2(1)=1
rn2(2)=1
else
print *, 'grump'
endif
c find the first neighbor that's id eq id of sitecent
c algorithm for finding neighbors in the rn(1),rn(2) dircection in 3D space

```



```

do j1=1,6
L(j1)=sqrt((position(1,site)+rn2(1)*unitvect(rn2(2),1)*10-
1 position(1,nabor(j1,site)))**2
2 +(position(2,site)+rn2(1)*unitvect(rn2(2),2)*10
3 -position(2,nabor(j1,site)))**2
4 +(position(3,site)+rn2(1)*unitvect(rn2(2),3)*10
5 -position(3,nabor(j1,site)))**2)
enddo
do j1=1,12
L(j1+6)=sqrt((position(1,site)+rn2(1)*unitvect(rn2(2),1)*10-
1 position(1,dnabor(j1,site)))**2
2 +(position(2,site)+rn2(1)*unitvect(rn2(2),2)*10
3 -position(2,dnabor(j1,site)))**2
4 +(position(3,site)+rn2(1)*unitvect(rn2(2),3)*10
5 -position(3,dnabor(j1,site)))**2)
enddo
c find the minimum distance
do j1=1,18
if (L(j1).eq.(min(L(1),L(2),L(3),L(4),L(5),L(6),L(7),L(8),L(9)
1 ,L(10),L(11),L(12),L(13),L(14),L(15),L(16),L(17),L(18)))) then
neighborlist=j1
exit
endif
enddo
edgeflag = .false.
if (neighborlist.le.6) then
j5=neighborlist
site2=nabor(j5,site)
edgeflag = .false.
c if neighbor is of a same phase then move
if (id2.eq.domain(nabor(j5,site))) then
edgeflag = .true.
exit
endif
if (edgeflag) exit
elseif (neighborlist.ge.7) then
j5=neighborlist-6
site2=dnabor(j5,site)
c if neighbor is of a different phase then accept
if (id2.eq.domain(dnabor(j5,site))) then
edgeflag = .true.
exit

```

```

endif
if (edgeflag) exit
endif
enddo !end counter loop
c move to new site
site = site2
c stop moves if back where started
if (site.eq.sitecent) exit
c now turn to the right twice
rn2(1)=-rn2(1)
enddo !end moves loop
endif !end of if statement for if loop was found
c need to find the length of a straight line
site1=sitecent
site2=site
lengthstraight=sqrt(
1 real(mod((position(1,site1)-position(1,site2)),density))**2
2 +real(mod((position(2,site1)-position(2,site2)),density))**2
3 +real(mod((position(3,site1)-position(3,site2)),density))**2)
c record curve
curve=lengthstraight/real(moves)
c reject sample if didn't do 5 moves
if (moves .lt. lengthmax) then
curve=0
endif
c print *, 'made it',curve
return
end
C*****
C Calculate the inter-domain area fractions, average
C node energy, and relative error in area fractions.
C
C Inter-domain area fractions are same as probabilities
C P2tot calculated in subroutine probimage, except here it
C must be computed in 3 dimensions with periodic boundaries
C*****
SUBROUTINE stats(P2sim,Pd2sim,P2tot,Pd2tot,E2,Ed2,
1 Etot,error)
integer density,ngrid
Parameter (density=220,ngrid=density**3)
integer site,j1,j2,id,idn
real*8 P2sim(0:2,0:2),P2tot(0:2,0:2),E2(0:2,0:2),Pincr

```

```

real*8 Pd2sim(0:2,0:2),Pd2tot(0:2,0:2),Ed2(0:2,0:2)
integer nabor(6,ngrid),dnabor(12,ngrid),domain(ngrid),
1 position(3,ngrid)
real keff(9),potl(ngrid),length
common nabor,dnabor,domain,position,keff,potl,length
real Etot,error
c
c initialize pair probability arrays
do j2 = 0, 2
do j1 = 0, 2
P2sim(j1,j2) = 0.D0
Pd2sim(j1,j2) = 0.D0
enddo
enddo
c
c Loop over every node and look at adjacent nodes,
c relying on periodic boundaries to eliminate edge
c effects. In accumulating pair sample, make sure
c probability arrays are symmetric and normalized.
c
Pincr = 1.D0/(12*ngrid) !increment for pair accumulator
c
do site = 1, ngrid
id = domain(site) !identify primary node
c first look at lateral nodes in the
c positive x,y,z directions
do j1 = 1, 5, 2
idn = domain(nabor(j1,site)) !identify neighbor
P2sim(id,idn) = P2sim(id,idn) + 2*Pincr
P2sim(idn,id) = P2sim(idn,id) + 2*Pincr
enddo
c next look at diagonal nodes
do j1 = 1, 11, 2 !look at half of neighbors
idn = domain(dnabor(j1,site)) !identify neighbor
Pd2sim(id,idn) = Pd2sim(id,idn) + Pincr
Pd2sim(idn,id) = Pd2sim(idn,id) + Pincr
enddo
enddo
c
c Get average node energy from inter-domain area fractions.
c Also get squared error function based on relative
c deviation of area fractions for simulation vs. image.

```

```

c
Etot = 0.
error = 0.
do j2 = 0, 2
do j1 = 0, 2
Etot = Etot + E2(j1,j2)*P2sim(j1,j2)
1 + Ed2(j1,j2)*Pd2sim(j1,j2)
error = error + (P2sim(j1,j2)/P2tot(j1,j2) - 1.)**2
1 + 0.5*(Pd2sim(j1,j2)/Pd2tot(j1,j2) - 1.)**2
enddo
enddo
return
end
C*****
c calculate the ionic tortuosity of the system
c in a given direction
c
c In order to take advantage of periodic boundaries in all
c three dimensions, the potential at each node is taken as
c relative to the average linear potential profile induced
c by an external field. For example, if the field is in the
c x direction:
c potl_tot = potl + Field*x
C*****
subroutine gettau(direction,rhoP,rhoC,condP,taui)
integer density,ngrid
Parameter (density=220,ngrid=density**3)
real taui,taui1,taui2
integer nabor(6,ngrid),dnabor(12,ngrid),domain(ngrid),
1 position(3,ngrid)
real keff(9),potl(ngrid),length
common nabor,dnabor,domain,position,keff,potl,length
integer site,j1,id1,site2,iter,itermax,direction,
1 post
real potlold,threshold,ktot,Itot,I1tot,I2tot,
1 kefft,relax,field(6)
real*8 rhoP,rhoC,condP
logical stopflag
stopflag = .false.
iter = 0
itermax = ngrid/10 !max number of iterations
threshold = 1.E-3 !Threshold to stop interations

```

```

relax = -0.9 ! relaxation parameter for
c convergence stability (between 0 and 1)
c or convergence acceleration (between 0 and -1)
c initialize potential field
c set up external field, which is average dimensionless
c gradient in total potential
do j1 = 1, 6
field(j1) = 0.
enddo
field(2*direction-1) = 1.
field(2*direction) = -1.
c
c begin iterations to solve for relative node potentials
c using finite difference equations
do while (.not. stopflag)
iter = iter + 1
stopflag = .true.
c
c loop over nodes
do site = 1, ngrid
id1 = 1 + 3*domain(site)
c skip site potential update if is active material
c (i.e. conductivity=zero)
if (id1.eq.1) cycle
post = position(direction,site)
Itot = 0.
ktot = 1.E-10 !give small value for stability
do j1 = 1, 6 !loop over neighbors
site2 = nabor(j1,site)
kefft = keff(id1 + domain(site2))
Itot = Itot + kefft*(potl(site2)+field(j1))
ktot = ktot + kefft
enddo
c update site potential with use of relaxation
c parameter for stability or acceleration
potlold = potl(site)
potl(site) = (1.-relax)*Itot/ktot + relax*potlold
c stop iterations if all node changes are below threshold
if (abs(Itot/ktot-potlold).gt.threshold) stopflag = .false.
enddo ! end loop over nodes
c
c end iterations if exceed max iterations

```

```

if (iter .gt. itermax) then
write(6,*)'max iterations exceeded'
stopflag = .true.
continue
endif
enddo !end loop over matrix iterations
c
c now calculate flux on two different planes
c
I1tot = 0.
I2tot = 0.
do site = 1, ngrid
id1 = 1 + 3*domain(site)
if (id1 .eq. 1) cycle !skip site if is active material (no flux)
post = position(direction,site)
if (post .eq. density) then ! on outer surface
site2 = nabor(2*direction-1,site)
I1tot = I1tot + keff(id1 + domain(site2))
1 *(potl(site2) - potl(site) + 1.0)
elseif (post .eq. density/2) then ! at midplane
site2 = nabor(2*direction-1,site)
I2tot = I2tot + keff(id1 + domain(site2))
1 *(potl(site2) - potl(site) + 1.0)
endif
enddo ! end loop over nodes
c
c turn flux into inverse tortuosity
taui1 = I1tot/(condP*(rhoP+rhoC*0.63)*density**2)
taui2 = I2tot/(condP*(rhoP+rhoC*0.63)*density**2)
taui = 0.5*(taui1 + taui2) + 1.E-9
write(6, '(A,I2,A,I7,A,G11.4)')' dir =',direction,
1 ' iter =',iter,' tau =',1./taui
write(6,*) 'Itot', 0.5*(I1tot+I2tot)/(density**2)
c write(6,*) 'porosity tot', (rhoP+rhoC*0.63)
taui1 = (I1tot/(density**2))
taui2 = (I2tot/(density**2))
taui = 0.5*(taui1 + taui2)
return
end
C*****
c calculate the electronic conductivity of the system
c in a given direction

```

```

c
c In order to take advantage of periodic boundaries in all
c three dimensions, the potential at each node is taken as
c relative to the average linear potential profile induced
c by an external field. For example, if the field is in the
c x direction:
c potLtot = potl + Field*x
C*****
subroutine gettau2(direction,rhoP,rhoC,condP,taui)
integer density,ngrid
Parameter (density=220,ngrid=density**3)
real taui,taui1,taui2
integer nabor(6,ngrid),dnabor(12,ngrid),domain(ngrid),
1 position(3,ngrid)
real keff(9),potl(ngrid),length
common nabor,dnabor,domain,position,keff,potl,length
integer site,j1,id1,site2,iter,itermax,direction,
1 post
real potlold,threshold,ktot,Itot,I1tot,I2tot,
1 kefft,relax,field(6)
real*8 rhoP,rhoC,condP
logical stopflag
stopflag = .false.
iter = 0
itermax = ngrid/10 !max number of iterations
threshold = 1.E-3 !Threshold to stop iterations
relax = -0.9 ! relaxation parameter for
c convergence stability (between 0 and 1)
c or convergence acceleration (between 0 and -1)
c initialize potential field
c set up external field, which is average dimensionless
c gradient in total potential
do j1 = 1, 6
field(j1) = 0.
enddo
field(2*direction-1) = 1.
field(2*direction) = -1.
c
c begin iterations to solve for relative node potentials
c using finite difference equations
do while (.not. stopflag)
iter = iter + 1

```

```

stopflag = .true.
c
c loop over nodes
do site = 1, ngrid
id1 = 1 + 3*domain(site)
c skip site potential update if is active material
c (i.e. conductivity=zero)
if (id1.eq.1) cycle
post = position(direction,site)
Itot = 0.
ktot = 1.E-10 !give small value for stability
do j1 = 1, 6 !loop over neighbors
site2 = nabor(j1,site)
kefft = keff(id1 + domain(site2))
Itot = Itot + kefft*(potl(site2)+field(j1))
ktot = ktot + kefft
enddo
c update site potential with use of relaxation
c parameter for stability or acceleration
potlold = potl(site)
potl(site) = (1.-relax)*Itot/ktot + relax*potlold
c stop iterations if all node changes are below threshold
if (abs(Itot/ktot-potlold).gt.threshold) stopflag = .false.
enddo ! end loop over nodes
c
c end iterations if exceed max iterations
if (iter .gt. itermax) then
write(6,*)'max iterations exceeded'
stopflag = .true.
continue
endif
enddo !end loop over matrix iterations
c
c now calculate flux on two different planes
c
I1tot = 0.
I2tot = 0.
do site = 1, ngrid
id1 = 1 + 3*domain(site)
if (id1 .eq. 1) cycle !skip site if is active material (no flux)
post = position(direction,site)
if (post .eq. density) then ! on outer surface

```



```

site2 = nabor(2*direction-1,site)
I1tot = I1tot + keff(id1 + domain(site2))
1 *(potl(site2) - potl(site) + 1.0)
elseif (post .eq. density/2) then ! at midplane
site2 = nabor(2*direction-1,site)
I2tot = I2tot + keff(id1 + domain(site2))
1 *(potl(site2) - potl(site) + 1.0)
endif
enddo ! end loop over nodes
c
taui1 = (I1tot/(density**2))
taui2 = (I2tot/(density**2))
taui = 0.5*(taui1 + taui2)
write(6,*) 'condA and direction', keff(1), direction
write(6,'(A,I2,A,I7,A,G11.4)') ' dir =',direction,
1 ' iter =',iter,' sigma/sigmaC =',taui
return
end

```

Appendix C. Maccor test schedule

This is a sample Maccor test schedule used to test electrodes fabricated at BYU.

```
Rest Step Time = 00:05:00 002 Voltage 0.01 3NNN Step Time 00:00:30
Do1
Advance Cycle
Charge Current 0.5C Voltage >= 4.0 005 Step Time 00:01:00 3NNN Voltage 0.05
Charge Voltage 4.0 Current <= 0.02C 006 Step Time 00:01:00 3NNN Voltage 0.05
Rest Step Time = 01:00:00 007 Step Time 00:01:00 3NNN Voltage 0.05
Discharge Current 0.5C Voltage <= 2.2 008 Step Time 00:01:00 3NNN Voltage 0.05
Rest Step Time = 01:00:00 009 Step Time 00:01:00 3NNN Voltage 0.05
Loop1 Loop Count = 4 010
Advance Cycle
Charge Current 0.5C Voltage >= 4.0 012 Voltage 0.05 3NNN Step Time 00:05:00
Charge Voltage 4.0 Current <= 0.02C 013 Voltage 0.05 3NNN Step Time 00:05:00
Rest Step Time = 01:00:00 014 Voltage 0.05 3NNN Step Time 00:05:00
Discharge Current 0.1C Voltage <= 2.2 015 Voltage 0.05 3NNN Step Time 00:01:00
Rest Step Time = 01:00:00 016 Voltage 0.05 3NNN Step Time 00:05:00
Charge Current 0.5C LHC-AHr >* 0.5 017 Voltage 0.05 3NNN Step Time 00:01:00
End
```